Studies of correlation effects in layered transition metal oxides

By

Kwan-Woo Lee
B.S. (Korea University) 1996
M.S. (Korea University) 1998

DISSERTATION

Submitted in partial satisfaction of the requirements for the degree of

Doctor of Philosophy

in

Physics

in the

OFFICE OF GRADUATE STUDIES

of the

UNIVERSITY OF CALIFORNIA
DAVIS

Approved:

_____

_____

_____

Committee in Charge

2006

Abstract

Studies of correlation effects in layered transition metal oxides

by

Kwan-Woo Lee

For a correlated system, conventional *ab initio* band theory, the local density approximation (LDA), frequently fails to supply a correct ground state due to lack of consideration of correlation effects. In this research, I will investigate the strength and effect of Coulomb correlations in the three layered transition-metal oxides, using a correlated band theory LDA+U including correlations due to intra-atomic Coulomb repulsion U.

First, the LDA+U method is applied to study charge disproportionation, and charge and spin ordering in Na_xCoO_2, which forms a superconductor ($T_c \approx$4.5 K) when hydrated. My results display a charge disproportionation transition (for example, at x=0.5, $2Co^{3.5+} \rightarrow Co^{3+} + Co^{4+}$) at a (moderate) critical U_c for $0 \leq x < 1$. The disproportionation in the Co a_g orbital results in a fraction x of Co ions becoming electronically and magnetically dead, which subsequently undergo charge ordering and metal-insulator transition. In particular, precisely at x=0.5, the observed antiferromagnetic insulating phase, various ordering patterns are analyzed and an observed "out-of-phase stripe" pattern of antiferromagnetic Co^{4+} spins is discussed in terms of distinct analogies and substantial differences with cuprates. Also, by comparison with experiments, I suggest a crossover from effective single-band character $U \gg W$ for $x > 0.5$ into a three-band regime for $x < 0.5$, resulting

in the Coulomb repulsion strength significantly dependent on the carrier concentration.

Second, in $LaNiO_2$ with the Ni ion having the same formal ionic configuration $3d^9$ as does Cu in isostructural $CaCuO_2$ which is a parent material of high T_c superconductor cuprates, correlation effects do not appear to be large. However, *ad hoc* increase of the intra-atomic repulsion on the Ni site is found to lead to a novel correlated state: (i) the transition metal $d_{x^2-y^2}$ and $d_{3z^2-r^2}$ states undergo consecutive Mott transitions and (ii) their moments are *antialigned* leading (ideally) to a "singlet" ion in which there are two polarized orbitals.

Third, for Sr_2CoO_4 newly synthesized by two groups, the system (formal oxidation state Co^{4+}) shows a high Curie temperature ($\sim$ 250 K). But the two groups report different moments of 1.8 μ_B and 1 μ_B per Co. Using both LDA+U and LSDA, the combined effects of correlation and hybridization with O $2p$ states are calculated and analyzed. Sr_2CoO_4 is already ferromagnetic within LSDA (M=1.95 μ_B). At a critical value U_c=2.5 eV, a metal to half metal (M=1 μ_B) transition occurs. Keeping U at U_c, fixed spin moment calculations show similar behavior. Although the energy minima occur very near integer values of the moment/Co ($1\mu_B, 2\mu_B$), the strong $3d-2p$ mixing and resulting $3d$ orbital occupations seem to preclude any meaningful $S=\frac{1}{2}$ or $S=1$ assignment to the Co ion.

Contents

[1] This chapter has been published previously as a paper: "Infinite-layer $LaNiO_2$: Ni^{1+} is not Cu^{2+}", K.-W. Lee and W. E. Pickett, Phys. Rev. B **70**, 165109 (2004).

[2] This chapter has been published previously as a paper: "Correlation Effects in the High Formal Oxidation-state Compound Sr_2CoO_4", K.-W. Lee and W. E. Pickett, Phys. Rev. B **73**, 174428 (2006).

[3] E. C. Stoner, Ferromagnetism. *Rep. Prog. Phys.* **11**, 43 (1947).

List of Tables

List of Figures

Abbreviations

AFM: antiferromagnetic or antiferromagnetism

AMF: around mean field

CD: charge disproportionated

CDW: charge-density-wave

CLDA: constrained local density approximation

CO: charge order

DFT: density functional theory

FM: ferromagnetic or ferromagnetism

FPLO: full-potential nonorthogonal local-orbital approach

FSM: fixed spin moment

FLL: fully localized limit

MIT: metal-insulator transition

L(S)DA: local (spin) density approximation

LDA+U: local density approximation + Hubbard U

PM: paramagnetic or paramagnetism

SDW: spin-density-wave

UD: undisproportionated

VCA: virtual crystal approximation

Chapter 1

Introduction

Since the discovery of high temperature superconductivity in cuprates, there has been intense interest in transition-metal oxides with strongly layered (quasi) two-dimensional (2D) crystal structures and electronic properties. A second surprise appeared in 2001 with the discovery of T_c=40 K in MgB_2, where the physics is entirely different but the 2D character is crucial for the surprisingly high value of critical temperature T_c. A further stimulus for study of 2D transition-metal oxides was provided in 2003 with the discovery of superconductivity in hydrated Na_xCoO_2 at T=4.5 K.

The electronic structure of transition-metal oxides with incompletely filled $3d$ shells, for example monoxides, has been studied for a long time. From a bandstructure point of view, e.g., the local density approximation (LDA) within the density functional theory (DFT), the monoxides, such as MnO, CoO, and NiO, should be metals, owing to incompletely filled $3d$ states. In contrast to the prediction, experiments show these systems are insulators. A strong Coulomb correlation between the d electrons is responsible for the insulating gap of the monoxides. Briefly, the d electrons remain localized at the metal

ions, because their Coulomb correlations prevent them from forming an incompletely filled $3d$ band. LDA frequently fails to predict the ground states in the strongly correlated $3d$ or $4f$ systems. In particular, there are three well-known failures: this insulating gap problem, underestimating equilibrium lattice parameters, and under- or over-estimating magnetism. The failures of LDA require more accurate methods like LDA+U (local density approximation + Hubbard U), which have been relatively successful for some correlated materials. The LDA+U method has been suggested to classify the correlated orbitals and describe their electronic interactions as strongly correlated states.

In this thesis, I will focus on three layered transition-metal oxides (Na_xCoO_2, $LaNiO_2$, and Sr_2CoO_4), possibly showing strongly correlated behavior and analogies with the cuprates, using the LDA and LDA+U methods to study the correlation effects. In addition to the superconductivity, Na_xCoO_2 shows a rich variation of properties: phase separation between correlated and uncorrelated regimes at x=0.5, insulating antiferromagnetic phase with a tiny gap precisely at x=0.5, presumed Mott insulating phase at x=0, and magnetic phase diagram dependent on x. A striking picture is the triangular lattice of CoO_2 layers which can be frustrated when allowing antiferromagnetic interaction of Co ions. Second, $LaNiO_2$ is isostructural to $CaCuO_2$ which is a parent system of high T_c superconducting cuprates. Both Ni and Cu in each system have the same formal ionic configuration $3d^9$. Since it is reported to be nonmagnetic and probably metallic, correlation effects do not seem to be strong. Third, the recently synthesized Sr_2CoO_4 has the ideal (no tilting) 2D K_2NiF_4 structure as in La_2CuO_4, which is another parent system of high T_c superconducting cuprates. Instead of superconductivity, this system shows interesting ferromagnetic behavior with high Curie temperature. Two recent reports, using samples

synthesized by different methods, indicate different magnetic moments.

The thesis will be organized as follows. In Chapter 2, the theoretical background of my approach methods will be provided. In following separate chapters for each system, observations will be reviewed and then my results mainly obtained with the LDA+U method will be addressed. In particular, in Chapter 3, I will indicate how the frustration is relieved by charge disproportionation/ordering of Co ions in the sodium cobaltates, which is one of the most remarkable successes of the LDA+U method.

Chapter 2

Theoretical background

2.1 Density Functional Theory

Modern electronic structure calculation methods can be divided into the traditional wave function (for example, Hartree-Fock approach) and the density functional methods. The wave function method is based on the Schrödinger equation (for the many-electron wavefunction) obtained within the Born-Oppenheimer approximation, in which the much heavier nuclei than electrons are assumed to be fixed in space. Generally speaking, the wave function methods supply accurately properties of solids for sufficiently small atom systems. But, for a many-electron system, a lot of Slater determinants are required, so that they are too time-consuming to solve due to the so-called "exponential wall" named by Kohn.[1] Instead of the many-body wavefunction described by Slater determinant, the density functional theory (DFT) is focused on the electron density $n(r)$. At the current stage, DFT can be applied up to a system containing a order of 10^2 –10^3 atoms. In this section, I will review briefly DFT and the local density approximation, which is the

simplest approximation employed to solve the Kohn-Sham equations.

Two theorems given by Hohenbeg and Kohn (HK) are the foundation of the DFT.[2] First, the potential (to within a constant), and the resulting energy, is uniquely specified by the electron density $n(r)$. Second, the HK variational principle shows that the ground state energy is determined by minimizing the energy functional with respect to the density. One year later, Kohn and Sham[3] invented the energy functional, for an interacting electron system, as a sum of the kinetic energy term $T_s[\tilde{n}]$ of the ground state of the noninteraction electron system with the same density, the Hartree energy ($E_H[\tilde{n}] = \frac{1}{2}\iint \frac{\tilde{n}(r)\tilde{n}(r')}{|r-r'|}drdr'$), the exchange-correlation term $E_{xc}[\tilde{n}]$, and the electron-ion interaction term $E_{ext}[\tilde{n}]$:

$$E[\tilde{n}] \equiv T_s[\tilde{n}] + E_H[\tilde{n}] + E_{xc}[\tilde{n}] + E_{ext}[\tilde{n}], \tag{2.1}$$

where $\tilde{n}$ is a valid density. Applying the HK variational principle in the following form,

$$\frac{\delta}{\delta\phi_j^*(r)}\left\{E[\tilde{n}] + \sum_j \varepsilon_j \left[\int \phi_j^2 dr - 1\right]\right\} = 0 \tag{2.2}$$

with a Lagrangian multiplier ε_j. The effective single-particle equation is obtained[1] such as

$$[-\frac{1}{2}\nabla^2 + v_{eff}(r) - \varepsilon_j]\phi_j(r) = 0, \tag{2.3}$$

where the minimizing density $n(r)$ is taken in the form

$$n(r) = \sum_{j=1}^{\#\ of\ electrons} |\phi_j(r)|^2, \tag{2.4}$$

[1]Note that T_s is explicitly expressed as a functional of the orbitals, i.e., $T_s = -\frac{1}{2}\sum_j |\nabla\phi_j|^2$. Thus, $\frac{\delta T_s}{\delta\phi_j^*} = -\frac{1}{2}\nabla^2\phi_j$.

and the effective external potential $v_{eff}(r)$ is given by

$$v_{eff}(r) \equiv v_{ext}(r) + v_H(r) + v_{xc}(r). \tag{2.5}$$

The local exchange-correlation potential $v_{xc}(r)$ is defined by $\frac{\delta}{\delta\tilde{n}(r)}E_{xc}[\tilde{n}]_{\tilde{n}(r)=n(r)}$, depending on the density distribution $\tilde{n}(r)$. Equation (2.3) is called the Kohn-Sham equation. The ground state energy can be calculated from Eq. (2.1), or combination of Eqs. (2.1) and (2.5) gives an equivalent form:

$$E = \sum_j \varepsilon_j + E_{xc}[n] - \int v_{xc}(r)n(r)dr - E_H. \tag{2.6}$$

Equations (2.3)–(2.6) may be solved self-consistently: (1) guess approximately an initial $n(r)$, (2) construct v_{eff}, (3) solve Eq. (2.3), (4) recalculate $n(r)$ from Eq. (2.4). Then, check whether a new $n(r)$ is close to an old $n(r)$. If not, one must iterate until they are equal (to some prescribed tolerance) to each other. Note that $v_{eff}(r)$, and hence $v_{xc}(r)$ can be directly determined by the density $n(r)$ if the density is independently known from experiment or wave function based calculations for a small system.[4]

Local Density Approximation

The only unknown part of the Kohn-Sham equations is the exchange-correlation energy. The practical usefulness of the Kohn-Sham equations relies wholly on the accuracy and simplicity in approximation of the exchange-correlation energy functional $E_{xc}[n]$ which can be written in the form[1]

$$E_{xc}[n] = \int e_{xc}(r;[n(\tilde{r})])n(r)dr. \tag{2.7}$$

Here, $e_{xc}(r;[n(\tilde{r})])$ describes an exchange-correlation energy per particle at the point r. It is a functional of the density $n(\tilde{r})$ at points $\tilde{r}$ near r. (The "near" means a distance like

the Fermi wavelength or the Thomas-Fermi screening length.[1])

We need an approximation for $E_{xc}[n]$, coming from outside of DFT, in view of the physics of electronic structure. The simplest, but very successful, approximation is the local density approximation (LDA):

$$E_{xc}^{LDA} \equiv \int e_{xc}\left(n(r)\right) n(r) dr, \tag{2.8}$$

where $e_{xc}(n)$ is the exchange-correlation energy per particle of a uniform electron gas of density n. Although LDA is undoubtedly best for the systems having slowly varying density, practically it has been found to be effective for most systems, because underestimation for the exchange energy and overestimation for the correlation energy partially cancel out in most systems.[1] However, it is a well-known fact that LDA fails to produce some crucial properties, for example insulating gap and magnetic moment, in correlated systems having strong $d-d$ or $f-f$ interactions, like transition-metal oxides and heavy fermion systems. (I will address one of the correlated band theory methods in Sec. 2.3.) Nevertheless, LDA can still supply some useful information even in these systems.

2.2 Full Potential nonorthogonal Local Orbital Schemes

Methods to solve the Kohn-Sham equations are frequently based on one of two different physical pictures: the tight-binding and the weakly bound (free electron) pictures. The foundation of the former is atomic functions, which broaden into bands due to large overlap integrals as the atoms become closer together. It is a better choice for the briskly oscillating wave functions near the ion cores. On the other hand, the basic idea of the latter is that, when switching on the periodic potential, the free electron bands folded into

the first Brillouin zone open a gap. The weakly bound approach works well where the wave functions are free electron-like, and in practice requires a pseudo-potential technique[5] to produce plane waves representing the wave functions.

It seems most appropriate to use a local orbital method, based on the tight-binding picture, for the correlated materials. In these studies, I have used the full-potential nonorthogonal local-orbital (FPLO) scheme,[6] which originates from the linear combination of atomic orbitals (LCAO) method.[7] (FPLO has been shown to be computationally efficient yet accurate.) In the FPLO method, the orbitals are given by a linear combination of the atomic-like basis orbitals $\phi_{\mathbf{s}L}(\mathbf{r}-\mathbf{R}-\mathbf{s})$ which is centered at sites $\mathbf{s}$ in the primitive cell defined by $\mathbf{R}$:

$$\Psi_{\mathbf{k}n}(\mathbf{r}) = \sum_{\mathbf{R}\mathbf{s}L} \phi_{\mathbf{s}L}(\mathbf{r}-\mathbf{R}-\mathbf{s}) C_{L\mathbf{s},\mathbf{k}n} e^{i\mathbf{k}\cdot(\mathbf{R}+\mathbf{s})}, \tag{2.9}$$

where L is a set of an atomic quantum numbers and $C_{L\mathbf{s},\mathbf{k}n}$ is a coefficient of the wave function. The orbital $\Psi_{\mathbf{k}n}(\mathbf{r})$ is a Bloch state. Since the basis is nonorthogonal, the secular equation is given by

$$HC = SC\varepsilon, \tag{2.10}$$

where the Hamiltonian H and overlap S matrices are defined by

$$H^{LL'}_{\mathbf{s}\mathbf{s}'} = \sum_{\mathbf{R}} < \mathbf{O}\mathbf{s}'L'|\widehat{H}|\mathbf{R}\mathbf{s}L > e^{ik\cdot(\mathbf{R}+\mathbf{s}-\mathbf{s}')}, \tag{2.11}$$

$$S^{LL'}_{\mathbf{s}\mathbf{s}'} = \sum_{\mathbf{R}} < \mathbf{O}\mathbf{s}'L'|\mathbf{R}\mathbf{s}L > e^{ik\cdot(\mathbf{R}+\mathbf{s}-\mathbf{s}')}. \tag{2.12}$$

Furthermore, in the FPLO method the set of basis orbitals is divided into the core and the valence orbitals to reduce the size of the matrices. Then, the core orbitals are chosen to be orthogonalized, resulting in the simplified eigenvalue problem.[6]

Now, I will focus on the basis set in FPLO. The core orbitals are strongly localized, resulting in no overlap with different sites. So the core orbitals are satisfied with the equation

$$(\widehat{T} + v_{\mathbf{s}}^{at})\phi_{\mathbf{s}Lc} = \phi_{\mathbf{s}Lc}\varepsilon_{\mathbf{s}Lc}, \tag{2.13}$$

where the crystal potential $v_{\mathbf{s}}^{at}$ is spherically averaged around the site center $\mathbf{s}$ and $\widehat{T}$ is the Kohn-Sham kinetic energy operator. In contrast to the core orbitals, the valence orbitals have usually higher energy than the averaged crystal potential. As a result, if the valence orbitals were assumed to obey Eq. (2.13), i.e., atomic-like, the orbitals would have a long range tail, leading to many overlap integrals. In FPLO, an additional spherical confining potential is employed to compress the long range tail. The valence orbitals are defined by

$$[\widehat{T} + v_{\mathbf{s}}^{at} + v_{conf}]\phi_{\mathbf{s}Lv} = \phi_{\mathbf{s}Lv}\varepsilon_{\mathbf{s}Lv}. \tag{2.14}$$

Here, the confining potential $v_{conf} \equiv (\frac{r}{r_0})^{\alpha}$, with $r_0 = (\frac{x_0 r_{NN}}{2})^{\frac{3}{2}}$ for nearest-neighbor distance r_{NN} and dimensionless compression parameter x_0, and the exponent α=4 empirically chosen for most systems (except for rare earth compounds). Moreover, the confining potential pushes up the orbital resonance energies $\varepsilon_{\mathbf{s}Lv}$ to near the band centers of the orbital projected DOS. An important feature of the FPLO basis treatment is that the total energy is minimized with respect to the set of compression parameters. The basis is readjusted at every iteration and is optimized in the course of iteration, thus, the basis of FPLO is not fixed.

Although in principle there are two classes in the basis of FPLO, practically we must treat the basis more carefully since the result and efficiency may depend on the basis set chosen. A few orbitals near the top of the core orbitals may violate the orthogonality

with orbitals from different sites. These orbitals (semi-core orbitals) must be treated as valence orbitals, although in fact they are fully occupied. Another important set of orbitals to be considered carefully is polarization orbitals, which have very small occupancy (less than a few tenths). In spite of the small occupancy, including the polarization orbitals typically enhances the effectiveness and accuracy of FPLO. For example, basis orbitals for Co can be chosen such as $(3s3p)4s4p3d$, where the orbitals in parenthese denote semicore orbitals.

2.3 LDA+U method

Although LDA has been demonstrated to be very efficient and accurate for conventional (uncorrelated) systems, it often fails to produce a correct ground state in strongly correlated systems. Correlated systems typically contain partially filled d or f shells, so LDA predicts the system to be metallic. In fact, however, the d or f states are localized and Hubbard model studies[2] have shown there is an energy splitting between occupied and unoccupied bands due to Coulomb repulsion U. The problem of LDA can be addressed by the Hartree-Fock method[8] and the GW approximation[9]. The former has a serious problem, usually a 2–3 times larger gap than the experimental value, due to the nature of the unscreened Coulomb interaction in this method. For example, for a $3d$ metal, the Coulomb interaction is reduced efficiently (about 50%) by the screening of $4s$ and $4p$ electrons.[10, 11] The GW method seems to be appropriate for a weakly correlated case.

[2]In the Hubbard model, the many-body Hamiltonian consists of two parts: electron-hopping and electron-electron interaction (on-site Coulomb repulsion U) terms. The former leads to metallic behavior. On the other hand, the latter tends to localize electrons on a site, resulting in insulating behavior (driving the transition to a Mott insulator.)

For highly correlated systems, one of the improved methods is LDA+U.[12, 13] The main idea is to separate electron states into two classes. The first is the delocalized s, p electron states, which could be described by LDA. The second is the localized d (or f) electron states where the Coulomb $d-d$ (or $f-f$) interaction should be considered roughly by a term $\frac{U}{2}\Sigma_{i\neq j}n_i n_j$, with a d orbital occupancy n_i. With this correction, unoccupied orbital energies, in simple models, for large U raise by $\frac{U}{2}$, while occupied orbital energies lower by $\frac{U}{2}$, leading to energy gap.

Correlated Orbital and LDA+U Energy Functional

The essence of the LDA+U method is to identify correlated orbitals $\{\phi_{\mathbf{R}m\sigma}\}$,[15] which are assumed to be angular momentum eigenstates[3] centered at $\mathbf{R}$. (m is the azimuthal quantum number. Hereafter, we will use simply $\{\phi_{\mathbf{R}m\sigma}\} = \{\phi_m\}$.)

The LDA+U variational total-energy functional[12] is given by

$$E^{tot}(\rho, \hat{n}) = E^{LDA}(\rho) + \underbrace{E^{ee}(\hat{n}) - E^{dc}(\hat{n})}_{E^U}, \tag{2.15}$$

where $E^{LDA}(\rho)$ is the L(S)DA energy functional of the total electron density ρ. (Only in this subsection, the L(S)DA electron density is represented by the notation of ρ.) $E^{dc}(\hat{n})$ with the local orbital occupation matrix $\hat{n}^\sigma = n^\sigma_{mm'}$ for the orbitals $\{\phi_m\}$ is a "double-counting" term. This "double-counting" removes an averaged LDA energy contribution of these correlated orbitals from the LDA energy (see below). The electron-electron Coulomb interaction $E^{ee}(\hat{n})$ is represented by the Hartree-Fock type[13, 14]:

$$E^{ee} = \frac{1}{2}\sum_{\{m\},\sigma\sigma'}(\langle m_1 m_2|\tilde{w}|m_3 m_4\rangle - \delta_{\sigma,\sigma'}\langle m_1 m_2|\tilde{w}|m_4 m_3\rangle)n^\sigma_{m_1 m_3}n^{\sigma'}_{m_2 m_4} \tag{2.16}$$

[3] In the FPLO method, real orbitals $\frac{(\phi_m \pm \phi_{-m})}{\sqrt{2}}$ are used.

with the screened electron-electron interaction $\tilde{w}$. Here, $\langle|\rangle$ denotes an angular intergral. The corresponding effective single-particle U potential V^U is

$$\begin{aligned} V^U &= \frac{\partial E^U}{\partial n^{\sigma'}_{m_2 m_4}} \\ &= \frac{1}{2}\sum_{\{m\},\sigma\sigma'} (\langle m_1 m_2|\tilde{w}|m_3 m_4\rangle - \delta_{\sigma,\sigma'}\langle m_1 m_2|\tilde{w}|m_4 m_3\rangle) n^{\sigma}_{m_1 m_3} - V^{dc}, \end{aligned} \tag{2.17}$$

where V^{dc} is a "double-counting" potential. If the occupation matrix $\hat{n}^\sigma$ is diagonal,[13] the expression simplify

$$\begin{aligned} n^{\sigma}_{mm'} &= \delta_{mm'} n_{m\sigma}, \\ U_{mm'} &= \langle mm'|\tilde{w}|mm'\rangle, \\ J_{mm'} &= \langle mm'|\tilde{w}|m'm\rangle, \end{aligned} \tag{2.18}$$

where J is Hund's rule exchange parameter. The on-site Coulomb repulsion U is the Coulomb energy cost to place two electrons at the same site. Thus, the electron-electron Coulomb interaction E^{ee} can be written simply in terms of the Hubbard-like density-density interaction:

$$E^{ee} = \frac{1}{2}\sum_{m\neq m',\sigma\sigma'} [U_{mm'} - \delta_{\sigma,\sigma'} J_{mm'}] n_{m\sigma} n_{m'\sigma'}. \tag{2.19}$$

This form displayed in Eq. (2.19) is schematic in the sense that it does not display all of the indices involved in the full coordinate-system-independent form that is implemented in the code.

Since only on-site interactions are considered in the E^{ee} functional, U and J are determined by on-site matrix elements for the screened electron-electron interaction $\tilde{w}$ from the atomic expression

$$\langle m_1 m_2|\tilde{w}|m_3 m_4\rangle = \sum_{l=0}^{2l_i} F_l a_l(m_1 m_2 m_3 m_4). \tag{2.20}$$

Here, the matrix should be satisfied with the conditions $\sigma_1 = \sigma_3$ and $\sigma_2 = \sigma_4$. The coefficient a_l and the Slater's integrals F_l [16] are given by

$$a_l(m_1 m_2 m_3 m_4) = \frac{4\pi}{2l+1} \sum_{m=-l}^{l} \langle Y_{l_i m_1} | Y_{lm} | Y_{l_i m_3} \rangle \langle Y_{l_i m_4} | Y_{lm} | Y_{l_i m_2} \rangle^*,$$

$$F_l \approx \iint_0^\infty dr_1 dr_2 (r_1 R_i(r_1))^2 (r_2 R_i(r_2))^2 \frac{r_<^l}{r_>^{l+1}}, \quad \texttt{for } l > 0. \tag{2.21}$$

Here, $r_<(r_>)$ is the smaller (larger) of r_1 and r_2. Combining Eqs. (2.20) and (2.21) with the sum rules[15]

$$\begin{aligned} \sum_{m_1} \langle m_1 m_2 | \tilde{w} | m_1 m_4 \rangle &= \delta_{m_2, m_4} (2l+1) U, \\ \sum_{m_1} \langle m_1 m_2 | \tilde{w} | m_3 m_1 \rangle &= \delta_{m_2, m_3} (U + 2lJ), \end{aligned} \tag{2.22}$$

the relations between the Hubbard U and exchange J and the Slater's integrals are derived as

$$\begin{aligned} U = F_0; \quad J = (F_2 + F_4)/14 \qquad &, \quad \texttt{for 3d systems}, \\ U = F_0; \quad J = (286F_2 + 195F_4 + 250F_6)/6435 \qquad &, \quad \texttt{for 4f systems}. \end{aligned} \tag{2.23}$$

The ratio F_2/F_4 and F_2/F_6 are taken from atomic situations. For example, for all $3d$ ions, the ratio F_4/F_2 is between 0.62 and 0.63.[17]

Double counting

There are two popular schemes for treatment of the "double counting" term, intended to subtract out the shell-averaged interaction that has already been included in LSDA. One choice is the so-called "around mean field" (AMF) scheme[4], which is expected

[4]Note that the AMF scheme produces no contribution in case of orbital-independent occupation number, for example, $4f$-shell of Gd ($4f^7$ configuration).

to be more suitable when the on-site Coulomb repulsion U is not so strong.[18] The other choice, called the "fully localized limit" (FLL) (also called "atomic limit"), is more appropriate for large U systems.[19] The method to treat the double counting problem in each scheme is given by

$$\begin{aligned} E^{dc}_{AMF} &= \frac{1}{2} \sum_{m \neq m', \sigma\sigma'} [U_{mm'} - \delta_{\sigma,\sigma'} J_{mm'}] \; \bar{n} \; \bar{n}, \\ E^{dc}_{FLL} &= \frac{1}{2} \sum_{m \neq m', \sigma\sigma'} [U_{mm'} - \delta_{\sigma,\sigma'} J_{mm'}] \bar{n}_\sigma \bar{n}_{\sigma'}, \end{aligned} \tag{2.24}$$

where $\bar{n}$ is the shell-averaged occupation, while $\bar{n}_\sigma$ is its spin-decomposed analog. These double-counting terms can be written in other forms that emphasize other aspects of the interaction.[20] However, this form is illustrative because it emphasizes that the difference lies in the magnitude of the (self-consistent) atomic moment. Clearly it is only the spherically averaged values of U and J that enter the double-counting terms. The difference between the two forms given in Eq. (2.24) is that the double-counting term, and the resulting potential, includes a spin dependence in the FLL form.

Constrained LDA

The question (and also a weak point) for the LDA+U method is how to define the Coulomb repulsion strength U in a real system. Introducing a constraining field induces the change of electron density $\delta\rho$. The energy change due to $\delta\rho$ is often evaluated in LDA, and this approach is called the constrained LDA (CLDA).

The basis of Kohn-Sham equations can be divided into two classes: delocalized orbitals (I) and localized orbitals (L). LDA works well for the former, whereas the latter requests an improved approach. Herring[21] defined the Coulomb strength as the energy

cost required to move a localized electron between two atoms at $\mathbf{R}$ and $\mathbf{R}'$:

$$U_{\mathbf{R},\mathbf{R}'} = E(n_{L\mathbf{R}} + 1, n_{L\mathbf{R}'} - 1) - E(n_{L\mathbf{R}}, n_{L\mathbf{R}'}). \tag{2.25}$$

Here, $n_{L\mathbf{R}}$ and $n_{L\mathbf{R}'}$ are the occupation numbers of the localized electrons at $\mathbf{R}$ and $\mathbf{R}'$. Assuming a smooth function of the occupation numbers,[22] by a Taylor expansion the Coulomb repulsion is given by

$$U_{\mathbf{R},\mathbf{R}'} \approx U_1 = \frac{\partial^2 E}{\partial n_{L\mathbf{R}}^2} = \frac{\partial \varepsilon_{L\mathbf{R}}}{\partial n_{L\mathbf{R}}}, \tag{2.26}$$

where $\varepsilon_{L\mathbf{R}} = \frac{\partial E}{\partial n_{L\mathbf{R}}}$ is a single particle energy of the localized electron. The definition of Eq. (2.26) is usually used in CLDA calculations. Using Slater's transition state arguments, Solovyev and Dederichs[22] obtained an another form:

$$U_{\mathbf{R},\mathbf{R}'} \approx U_2 = \varepsilon_{L\mathbf{R}}(n_{L\mathbf{R}} + \frac{1}{2}, n_{L\mathbf{R}'} - \frac{1}{2}) - \varepsilon_{L\mathbf{R}}(n_{L\mathbf{R}} - \frac{1}{2}, n_{L\mathbf{R}'} + \frac{1}{2}). \tag{2.27}$$

That is, U is the energy difference of two transition states. McMahan *et al.*[23], and Solovyev and Dederichs[22] showed that the difference between the Coulomb repulsion strengths (U, U_1, and U_2) obtained from these definitions is less than 5%, indicating these definitions can be considered equivalently.

On the other hand, the delocalized orbitals stimulate charge-transfer excitations between a localized orbital and a delocalized orbital at $\mathbf{R}$ and $\mathbf{R}'$ independently. In a real system, these excitations (screening effect) compete with the mechanism of Eq. (2.25). Thus, the appropriate Coulomb repulsion strength U[22, 24] is given by

$$U_{\mathbf{R},\mathbf{R}'} = E(n_{L\mathbf{R}} + 1, n_{I\mathbf{R}} - \delta, n_{L\mathbf{R}'} - 1, n_{L\mathbf{R}'} + \delta) - E(n_{L\mathbf{R}}, n_{I\mathbf{R}}, n_{L\mathbf{R}'}, n_{L\mathbf{R}'}). \tag{2.28}$$

Here, the amount of charge transfer δ is determined by minimizing U. This representation

indicates that the value of U strongly depends on how well localized electrons are screened by the delocalized electrons.

2.4 Fixed Spin Moment Method

The fixed spin moment (FSM) method[25] is a procedure to calculate the total-energy $E(M)$ with respect to constrained magnetic moments M through spin-polarized DFT (LSDA) calculations. The fixed magnetic moment may be considered as an effective externally applied magnetic field given by $H = \frac{dE}{dM}$.[26] The stable states are located at minimum points in E vs. M plot where H=0 and $\frac{d^2E}{dM^2} > 0$. This method can be used to study metastable magnetic states and magnetic phase transition. Now, I will briefly address this method in a practical point of view.

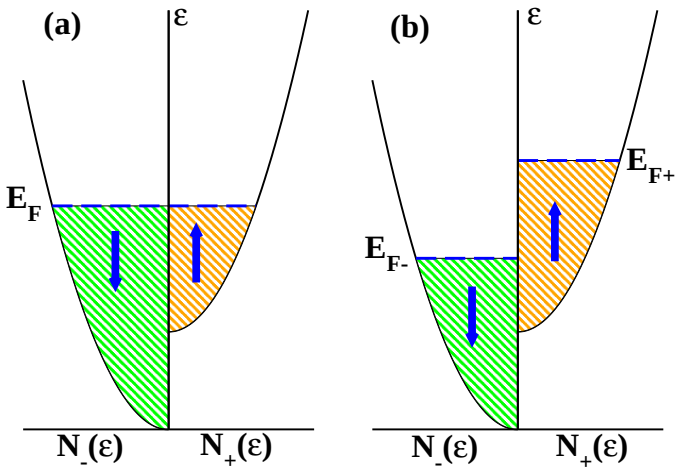

Figure 2.1. Schematic DOS for (a) a normal spin polarization and (b) a fixed spin moment (FSM) calculations. In the normal calculations, majority and minority states have a common Fermi energy, and the total magnetic moment M is determined self-consistently. However, in the FSM method, the densities of states for majority and minority states are separately calculated from M and $N = N_+ + N_-$ known in advance. Thus each state has a different Fermi energy.

The number of electrons N and the magnetic moment[5] M are given by

$$N = N_+ + N_- = \int_{-\infty}^{E_{F_+}} dE\ n_+(E) + \int_{-\infty}^{E_{F_-}} dE\ n_-(E), \tag{2.29}$$

$$M = N_+ - N_- = \int_{-\infty}^{E_{F_+}} dE\ n_+(E) - \int_{-\infty}^{E_{F_-}} dE\ n_-(E), \tag{2.30}$$

where $n_\sigma(E)$ is a spin-dependent DOS and E_{F_σ} is a spin-dependent Fermi energy. As illustrated in Fig. 2.1(a), in a normal spin polarization calculation, majority and minority

[5]Strictly speaking, M used here is the spin magnetic moment. In the FSM method, the orbital magnetic moment is always neglected. Only one of shortcomings due to neglecting the orbital contributions in the FSM method has been known. In principle, a threshold field of metamagnetic transition can be calculated from slope of total energy vs. fixed spin moment plot. The theoretical number is overemphasized. For example, in CoGd, the calculated field is 11% larger, due to neglecting the Co orbital moment.[27]

states have a common Fermi energy, and the total magnetic moment M is determined self-consistently. On the other hand, the spin dependent electron numbers N_σ are calculated from N and M given in advance in the FSM calculations,[25] so that $2N^\sigma = N + \sigma M$. Then, using Eq. (2.30), the spin dependent Fermi energies are determined, displayed in Fig. 2.1(b). The FSM self-consistently solved provides the lowest possible total energy for a given M. In general, $E_{F_+} \neq E_{F_-}$, but at metastable state (extrema in the E vs. M plot) difference between these Fermi energies becomes zeroes.

Applying FSM is specially useful for a system having more than one magnetic state. In some systems, the FSM procedure yields several extrema (meaning metastable or unstable states) in E vs. M plot. Near equilibrium, $E(M)$ gives the enhanced susceptibility, allowing to calculate the Stoner I (see Appendix A). The FSM method may result in predicting a metamagnetic transition in which a nonmagnetic system is rendered ferromagnetic.

Chapter 3

Sodium Cobaltates

3.1 Introduction

Initially, alkai-metal intercalated layered cobaltates, particularly Na_xCoO_2 at $x\sim$ 0.50–0.75, have been pursued for their high thermoelectric[1] properties.[30, 31, 32, 33, 34, 35, 36, 37, 38] In early 2003, Takatada *et al.* found superconductivity with $T_c\sim$4 K in the system $Na_xCoO_2{\cdot}yH_2O$ for x=0.3 when intercalated with water $y\sim$1.3.[39] The discovery and confirmation[38, 40, 41, 42, 43, 44, 45, 46, 47] of the superconductivity led to intense interest in the Na_xCoO_2 system. (So far, several hundred papers have been published.) Much has been made of the similarities of this cobaltate system to high T_c superconducting cuprates. Both are in the vicinity of a Mott insulator (although

[1] In a conducting isotropic solid, a temperature gradient should induce oppositely an electric field, the so called thermoelectric field. The phenomenon has been known as the "Seebeck effect". The field $\mathbf{E_Q}$ is written as $Q\nabla T$, where Q is the Seebeck coefficient, conceptually the average entropy per charge carrier divided by the electron charge. The efficiency of a thermoelectric solid depends on material properties through the dimensionless parameter ZT. The figure of merit Z is given by $Q^2/\kappa\rho$ with the thermal conductivity κ and electric resistivity ρ. The efficiency of power generator is $(T_h-T_c)(\gamma-1)/(T_c+\gamma T_h)$, and the coefficient of refrigerator performance is $(\gamma T_c-T_h)/[(\gamma+1)(T_h-T_c)]$. T_c and T_h are the temperature of a cold and hot ends, respectively. Here γ is given by $\sqrt{1+ZT}$ with the average temperature T. Therefore, when $ZT \gg 1$, the Carnot engine (or refrigerator) is achieved. But, the number for thermoelectric materials currently used is between 0.4 and 1.3.[28, 29]

CoO_2 seems to be metallic). The carrier concentration can be varied, and then there are specific superconducting regions: in the cuprates it is a dome-like shape in range of $0.06 \leq x \leq 0.33$, while in the cobaltates there are two different reports for the dome in both ranges of $0.27 \leq x \leq 0.33$ [47] and of $0.28 \leq x \leq 0.37$.[48] However, the distinctions between the cobaltates and cuprates are substantial. The Co layer forms a triangular lattice, which can be frustrated allowing AFM order (i.e., three neighbor spins cannot be antialigned simulataneously),[49, 50] instead of the bipartite square Cu lattice of the cuprates inviting AFM order. While the cuprates have corner-sharing CuO_6 octahedra (the Cu-O-Cu bond angle 180°), the CoO_6 octahedra are edge-sharing (the Co-O-Co bond angle 98.5°), resulting in much narrower bandwidth and smaller exchange coupling. In contrast to cuprates which are hole-doped AFM correlated insulators, the cobaltates are hole-doped band insulators.[51, 52] Most striking, in the cobaltates T_c^{max}=4.7 K compared with T_c^{max}=130 K (or higher under pressure) in cuprates.

In addition to interesting properties of the cobaltates in view of superconductivity, its normal state has a rich phase diagram depending on carrier concentration.[53] For x in the 0.5–0.8 range, the susceptibility $\chi(T)$ is Cuire-Weiss like with reported magnetic moment of order 1 μ_B per Co^{4+}.[33, 39, 40, 46, 54, 55] For x=0.75, A-type AFM ordering (FM layers stacked by AFM) at 22 K with small ordered moment has been observed through transport and thermodynamic data, [56] and separately μSR studies.[57, 58] Boothroyd *et al.* performed inelastic neutron scattering on x=0.75 single crystals and measured FM spin fluctuations.[59] Field dependence of the thermopower indicates that the spin entropy of the magnetic Co system is responsible for the unusual thermoelectric behavior.[38] Ando *et al.* for x=0.55, [60] and Jin *et al.*[61] and Miyoshi *et al.*[62] around x=0.74 reported a

rather large linear specific heat coefficient. Lupi, Ortolani, and Calvani shows five times mass enhancement of a carrier at $x = 0.57$ using measurements of optical conductivity.[63] At x=1, a band insulator, nonmagnetic Co^{3+} has been observed as expected.[64, 65] As a result, for $x > 0.5$, magnetic Co ions are evident and strongly influencing the electronic low energy excitations.[66, 67, 68, 69, 70] Specially at x=0.5, the system has been observed to undergo a metal-insulator transition at 50 K,[53, 71, 72] implying a charge disproportionation ($2Co^{3.5+} \rightarrow Co^{3+} + Co^{4+}$).[73, 74]

However, for $x < 0.5$, a Pauli-like susceptibility[2] has been observed.[40, 45, 46, 75] Besides, the linear specific heat coefficient is small,[41, 42, 61] comparable with my calculated value in LDA.[76] The local moments vanish in the region, so that the superconductivity emerges in the moment-free regime. In the strongly interacting single-band triangular lattice picture, the x=0 end member CoO_2 corresponds to the half-filled triangular lattice, but experiment finds it to be nonmagnetic and metallic, i.e., no local moments.[77] The x=0.3 region of superconductivity in Na_xCoO_2 initially reported[39] is well away from the expected Mott-insulator regime. It must be noted ,however, that several new reports identified the oxonium ion (also called hydronium) H_3O^+, leading to the effective doping level x_{eff}=0.5–0.6.[48, 78, 79, 80, 81]

Although the primary interest has been in the superconductivity, there is first a real need to understand the electronic structure of the normal state of the unhydrated material, and its dependence on the doping level x. The electronic structure at x=1/2 in the LDA has been described first by Singh.[82] Within LDA, all Co ions are identical and the t_{2g} manifold has a band width $W \sim 1.5$ eV. Singh expected the on-site Coulomb

[2]The unusual susceptibility observed by Sakurai *et al.*,[40] with $d\chi/dT$ positive above 130 K, was interpreted to include a Curie-Weiss term that would imply a Co moment of the order of 0.01 μ_B.

repulsion U=5–8 eV on Co, giving $U \gg W$ so that correlation effects can be anticipated.

Most theoretical researches[83, 84, 85, 86, 87, 88, 89, 90, 91] have been based on the strongly interaction limit, and (furthermore) presumed U is large enough to forbid double occupancy. But, the experiment observations, for example, change in enhancement of the linear specific coefficient and no local moments, suggests that a more realistic picture may be required. Since the near octahedral symmetry in the cobaltates makes the triplet t_{2g} states quasidegenerate, unquestionably the single band scenario is a limited one. Koshibae and Maekawa have reported unexpected complications of the t_{2g} manifold, including some analogies to a Kagomé lattice.[92]

Much of the interest in the cobaltates lies in the expectation that the system should be addressable in terms of nonmagnetic Co^{3+} and spin-half Co^{4+} ions as well as the triangular lattice of the Co layers. In this chapter, we focus on the correlation question for all x ranges, specifically x=0 (presumed Mott-insulator), 1/3 (close to the superconducting optimal concentration), 1/2 (unique insulating phase), and 2/3 (a representative of the correlation regime), by using the correlated band theory LDA+U method. The main achievement of the LDA+U method in this system is the charge disproportionation (CD),[73, 76] definitely reasonable for the insulating x=0.5 system. The critical on-site Coulomb repulsion U_c for CD shows strong x and magnetic ordering dependence. Comparison of experimental observations with my findings suggests x evaluation of moderate correlation strength.[93] Moreover, a crossover from a single-band regime to a three-band regime at x=0.5 results in dramatic reduction of the correlation strength below x=0.5.[76]

In the next section, I will summarize several important observations and controversies in the cobaltates: crystal structure (including effect of Na order), effect of

intercalating water, superconducting phase diagram, mechanisms of pairing, fermiology, insulating AFM phase at x=0.5, and magnetic tendencies around x=0.75. In the rest[3] of this chapter, I will address the uncorrelated behavior and correlated behavior in the cobaltates, using both LDA and LDA+U methods. In Sec. 3.3, I study the electronic structures, including variations dependent on x and Co-O bond length, for x=0, x=1/3, and x=2/3, using the virtual crystal approximation (VCA) within the local density approximation. In Na_xCoO_2, carriers donated from Na control valence states of Co ions, leading to xCo^{3+} and $(1-x)Co^{4+}$ formally. This charge-disproportionation (CD) can be expected from the Curie-Weiss behavior. Since it is impossible for the LDA method to produce CD, I employed the LDA+U method, accounting for correlation effects, and obtained successfully with a moderate on-site Coulomb repulsion. The mechanisms of CD will be discussed in Sec. 3.4. Then, I study two important phases, x=0 and 0.5. The former is a presumed Mott insulator, although observations seem to indicate a nonmagnetic metallic state, and the latter is a unique insulating phase with a tiny gap. In Sec. 3.5, I will account for how close to a Mott insulating state the phase is. Then, in Sec. 3.6, the AFM patterns which have been suggested will be contrasted and the observed stripe pattern will be compared with cuprates. Since there is no agreement on the best value of U, a combination of experiment observations and my results will supply the value, varying for x (Sec. 3.7). Finially, I will summarize my results and indications.

[3]Most of these parts will be based on my published papers.[73, 74, 76, 93, 94, 95, 96]

3.2 Summary of Observations

3.2.1 Structure

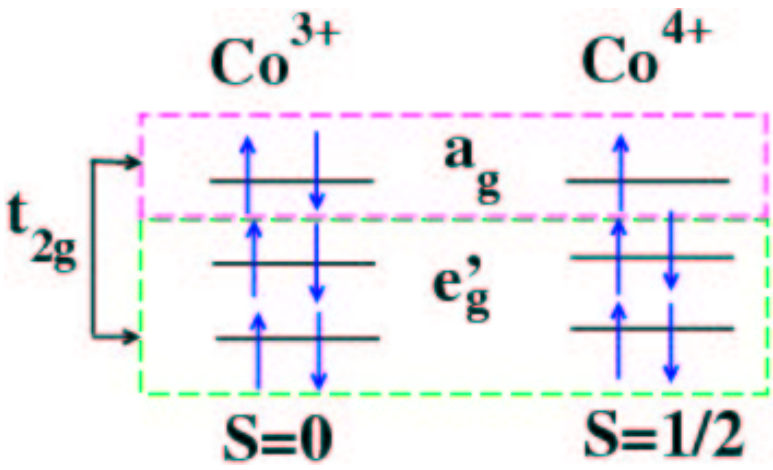

Figure 3.1. In the cobatates, the t_{2g} bands are broken in symmetry by the layered structure and the squashing of the CoO_2 layers away from ideal cubic coordination by six O ions. In view of low spin configuration, which has been observed in the system,[97] Co^{4+} ions are magnetic ones with $S = 1/2$, while Co^{3+} (d^6) ions become $S = 0$ nonmagnetic.

The crystal structure of both the normal and superconducting materials[33, 98, 99, 100, 101, 102, 103] is based on a two-dimensional CoO_2 layer in which edge-sharing CoO_6 octahedra lead to a triangular lattice of Co ions. The triangular lattice, which can be frustrated, stimulates one's interest more extensively. The layered structure and the distorted CoO_6 edge-sharing structure result in the symmetry lifting of the three-band t_{2g} states into singlet a_g + doublet e'_g. Additionally, in Na_xCoO_2, Na lying halfway between the CoO_2 layers donates its electron to the CoO_2 layers, hence x controls the doping level of the layer: x=0 corresponds to Co^{4+}, S=$\frac{1}{2}$ low spin ions with one minority t_{2g} hole, and

$x = 1$ corresponds to non-magnetic Co^{3+}.

Effect of Na order

There is some controversy of the effect of Na order: Na-Na repulsion accounts for the preferred order [104] without further mechanisms; Na^+ order and Co^{3+}/Co^{4+} order are coupled [105]; the observed Co^{3+}/Co^{4+} order can be obtained from a single-band extended Hubbard model [106] without any further complications; the small e_g' Fermi surfaces are destoryed by Na disorder.[107] Li *et al.*[108] used the observed Na superstructure [109] and included O ion relaxation but did not compare the results with simpler Na arrangements. Geck *et al.* have presented high-energy x-ray diffraction data and first principles calculations that provide new information, Na stripe-like ordering and connection with Co stripe ordering, in $Na_{0.75}CoO_2$.[110] I do not address this question in this research but note that the Na ordering I adopt [73, 74, 76] serves to break the the symmetry of the Co sites.

3.2.2 Superconducting state

Effect of Intercalating Water

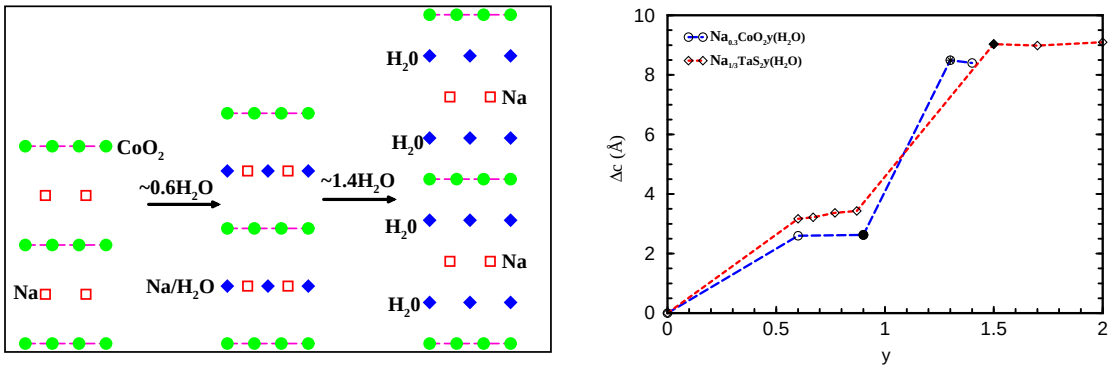

Figure 3.2. Left panel: Sketch of structure change, when intercalating water, showing two well-defined stages of hydration (see text). Note that the phase y ~0.6 is not a superconducting state yet. Right panel: Change in the c axis lattice parameter with the intercalating water, in two systems $Na_{0.3}CoO_2{\cdot}yH_2O$ and $Na_{1/3}TaS_2{\cdot}yH_2O$. The similarity in increase in the c lattice parameter between the two systems is evident. For the cobalates, the data are from Ref. [111] (empty circles), Ref. [46] (filled circle), and Ref. [47] (asterisk). For the chalcogenides, the data come from Ref. [112] (empty diamond) and Ref. [113] (filled diamond).

The hydration shows two well-defined stages, as illustrated in the left panel of Fig. 3.2. In the first stage, H_2O is incorporated into the same layer as the cation, and in the second stage two H_2O layers are formed on either side of the cation layer, resulting in superconductivity[4]. As a result, increase in c lattice parameter also shows two steps, displayed in the right panel of Fig. 3.2. (Note that, in the superconducting sample

[4]The superconductivity in the system also occurs in another structure, called a three-layer superconductor,[114, 115] due to different stacking pattern.[116] It has 50% larger c-lattice parameter than the intially reported superconductor, but similar T_c of about 4.3 K.

containing H_3O^+ ions, the ions are incorporated into the same layer as Na and act like a cation, although the stacking sequence[5] of the CoO_2 layers is different from the initially reported superconductor.) This trend is very similar with the transition metal disulfide based one $Na_{1/3}TaS_2 \cdot yH_2O$ having similar T_c.

Whether the system stays in the first or second stage strongly depends on humidity. Although high humidity is anticipated to weaken the quality of oxide superconductors, [118] all existing reports show that high humidity is a crucial factor in the superconductivity.[119, 120, 121, 122] Potavets *et al.* have reported that the superconducting phase having $\sim 1.2H_2O$ is stable at relative humidity higher than 30%, while the phase $\sim 0.6H_2O$ is stable below 30% humidity.[120] Foo *et al.* discuss in some detail that the superconducting phase exists above 43% humidty, the phase $\sim 0.6H_2O$ is stable between 10 and 50 %, and the normal state (without intercalating water) is stable below 35%.[119] Ohta *et al.* report the superconductivity also depends on the number of days stored in the humid atmosphere: observing no superconductivity less than 1 day and achieving final T_c after 7 days.[121]

The role of intercalating water in the system is still unclear. However, as seen before, intercalating water obviously increases the c lattice parameter, and subsequently squashes the CoO_2 layer.[111, 123] It results in enhancing two-dimensionality,[124, 125, 126, 127] which is believed by some to be a cause of the superconductivity. Recently, Arita showed that the a_{1g} band, which is a topmost valence band along Γ-Z line (i.e., c direction), in the bilayer hydrate (superconducting phase) becomes much flatter than

[5]The superconductor[80] is synthesized from a parent material having a $O3$-type structure, while the initial superconductor[39] from a parent material with a $P2$-type structure[117]. As a result, the new and initial superconductors are $P3$- and $P2$-type structures, respectively.

in the monolayer hydrate along the c direction, using first principles calculations.[126] Moreover, the water may shield a random Coulomb potential of Na ions,[111, 123, 128] resulting in redistribution of charge in CoO_2 layer.[124] Ning and Imai suggest that water intercalation leads to homogeneous CoO_2 planes and enhancement of spin fluctuation near T_c=4.5 K (probably due to nesting).[69]

Superconducting Phase Diagram

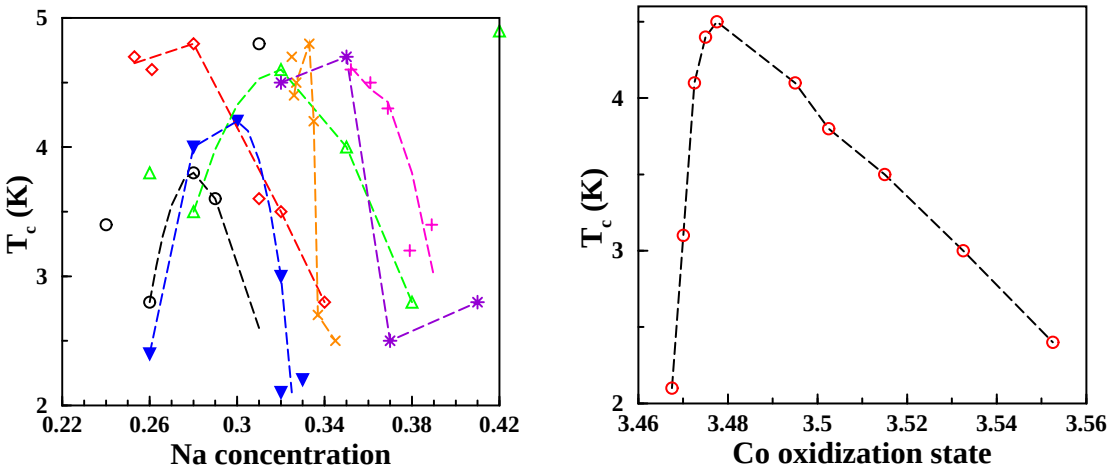

Figure 3.3. Left panel: Variation of the superconducting critical temperature T_c by Na concentration x. Neglecting a few deviating points, each phase line $T_c(x)$ can be fit well by dome-like shape, but each maximum lies on different position. The symbols of $\times$ and $+$ are for samples containing H_3O^+ ions and the asterisk symbols for samples intercalating D_2O instead of water. The data are from Ref. [129] (circle), Ref. [130, 131] (diamond), Ref. [132] (empty triangle), Ref. [47] (filled triangle), Ref. [48] ($\times$), Ref. [103] (asterisk), and Ref. [133] ($+$). Right panel: Change in T_c by Co oxidization state (see text). The data come from Ref. [134].

Although it is possible to vary Na concentration x, there are specific superconducting regimes, just as for cuprates. In contrast to the cuprates reported only a dome-shape, in the cobaltates there are two controversial reports: dome-like [47, 48, 134] and plateau.[132] But, as shown in Fig. 3.3, all reported data can be fit well by a dome even though each maximum lies on different concentration, if one neglects a few deviating points. (However, whether dome or plateau in shape of the phase diagram seems to be unclear yet.) Roughly, the maximum shifts to a little higher concentration when intercalating D_2O instead of H_2O. Compared with the cuprates having roughly a dome $0.05 \leq x \leq 0.33$, each dome exists in a much narrower range. These domes are reproduced within the charge-spin separation fermion-spin theory, as suggested in the cuprates, by Liu *et al.* who suggest the superconductivity is attributed to kinetic energy of dressed fermions.[135] Additionally, Barnes *et al.*[134] suggest an asymmetic dome having a maximum near Co oxidization state $\sim$+3.5, which is estimated from oxygen site occupancy, as displayed in the right panel of Fig. 3.3.

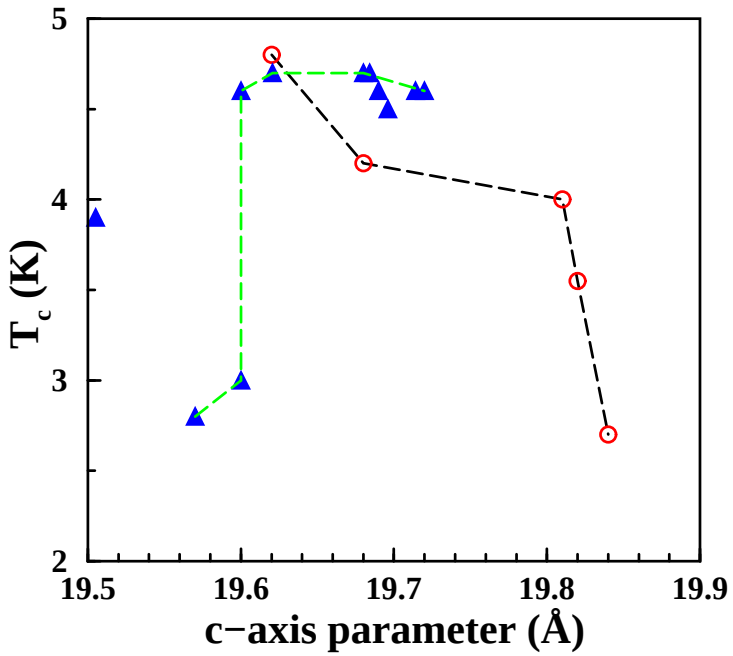

Figure 3.4. Effect of c lattice parameter on the superconducting critical temperature T_c. The maximum T_c is achieved in the range $19.6 < c < 19.8$ Å, and at the boundaries T_c decreases sharply. However, we should note that Na concentration is not fixed. The data are from Ref. [129] (circle) and Ref. [39, 46, 111, 120, 136, 137, 138, 139, 140] (triangle).

Another important factor to determine the superconducting phase diagram is believed to be the c lattice parameter (strictly, c/a ratio, but the a lattice parameter does not change much), because the two-dimensionality is considered by some to be a crucial element of the superconductivity. Lorenz *et al.* expected to increase T_c when intercalating larger molecules than water.[41] However, T_c drops sharply at $c \approx 19.8$ Å. A maximum T_c is achieved between $c \approx 19.6$ and 19.8 Å. Similar behavior has been observed in a sample containing H_3O^+ ions, but with no observation of sharp T_c-drop for the large c limit.[133]

In fact, as the various data diagrams imply, the system seems to have much more

distinct factors to determine superconducting phase diagrams than in the cuprates. In addition to carrier concentration and c/a ratio, there are a few known factors: air humidity keeping a sample, duration to store a sample in humidity, and amount of H_3O^+ ions[141]. More careful studies are required to determine the full nature of the superconducting phase diagram.

Correlation Strength of the Superconductivity

As said in the Introduction, comparison between experimentally measured and theoretically calculated values for linear specific heat coefficient indicates a phase separation of correlated and uncorrelated regime at x=0.5,[73, 76] starting to be confirmed by other more experimental observations[142, 143]. Furthermore, even for a sample intercalated with water, which becomes superconducting at T_c, the measured coefficient is comparable with that of a normal state $x \sim$0.3 (without water),[46, 144, 145, 146] implying the superconductivity is in an uncorrelated regime.

A system for comparison is the transition metal disulfide based one, with $Na_{1/3}TaS_2{\cdot}yH_2O$ as the primary comparison. One of two structures of the TaS_2 layer[147] is identical to that of the CoO_2 layer, consisting of edge-sharing transition metal chalcogenide octahedrons. In these dichalocogenides, as in the cobalates, two well-defined stages of hydration have been identified, as shown in the right panel of Fig. 3.2.[148] The electron concentration in $Na_{1/3}TaS_2{\cdot}yH_2O$ is specified by the Na concentration x=1/3, and superconductivity occurs at 4–5 K (the same range as in the cobalates) regardless of the concentration y of water molecules intercalated into the structure.[149] Specific thermodynamically stable phases were identified at y=0, 2/3, 0.8, 1.5, and 2.[112, 113, 150] The

long-known behavior of the tantalum disulfides also suggests that the superconductivity in the cobalates may be in the uncorrelated regime.

However, Chainani *et al.* have observed Co $2p$ core level spectra showing well-separated Co^{3+} and Co^{4+} in $Na_{0.35}CoO_2{\cdot}1.3H_2O$, using high-energy photoemission spectroscopy (for normal state bulk electronic structure) and cluster calculations.[151] The Co $2p$ spectrum of $Na_{0.35}CoO_2{\cdot}1.3H_2O$ is similar with that of $Na_{0.7}CoO_2$, which shows the A-type AFM ordering. The similarity has been also suggested by Ohat *et al.* using ^{23}Na NMR measurement.[152] Chou *et al.* reported heavy Fermi-liquid behavior through thermodynamic and transport measurements.[45] Moreover, several new reports characterizing the oxonium ions as leading to the effective doping level around x=0.5 suggest strongly that the cobalates may be in correlated regime. In the next subsection, I will summarize the details.

Mechanism of the Superconductivity

Magnetic fluctuations. There are several reports to show analogy to heavy fermion systems. Ishida *et al.* [137] and Ihara *et al.*[139] suggested the superconductivity is related to magnetic fluctuations, using ^{57}Co NQR measurement. This viewpoint has been confirmed by ^{23}Na NMR measurement[152]. High-enegy photoemission spectroscopy studies[151] also suggest that this superconducting sample shows similar behavior with x=0.7 which has been observed FM fluctuation (see below). However, ^{17}O NMR measurement gave no evidence of ferromagnetic correlation.[153]

Fermi liquid behavior, pseudogap and line nodes. These behaviors have been discussed for a decade in high T_c cuprates. Whether these phenomena enhance or weaken su-

perconductivity is still questionable.[154] In the cobalates, Fermi liquid behavior has been observed around x=0.7.[62, 155, 156] Even near the superconducting regime, Fermi liquid behavior has been measured by ^{59}Co NMR[157] and thermodynamic transport studies[45]. However, recently, Ribadulla *et al.* reported that the Fermi liquid behavior is suppressed to spin glass and non-Fermi liquid characteristics due to a magnetic quantum phase transition in the superconducting regime using magnetic measurement.[156] Shimojima *et al.*[158] and Lemmens *et al.*[159] suggest the formation of a pseudogap, which seems to be associated with charge ordering, below $T \sim$150 K. Several reports suggest the cobaltates show line nodes in the supercondcuting gap.[130, 145, 160, 161]

Superconducting pairing symmetry. According to Pauli exclusion principle, "pairs with a singlet (triplet) spin part have a corresponding even (odd) spatial part", represented by s-, p-, d-, or f-wave pairing.[162] At first, for the spin part, Sasaki *et al.* suggest a spin singlet pairing, indicated by upper critical field H_{c2} suppressed to the Pauli magnetic limit.[163] Using ^{59}Co-NMR Knight shift, Kobayashi *et al.* have measured the shift decreasing below T_c in both ab-plane and c-axis directions, suggesting singlet pairing.[164] However, both observations are contradicted by the Knight shift studies, interpreted as indicating spin triplet pairing.[44, 140, 165] Maśka *et al.* suggests a competition between the singlet and triplet pairing through careful measurements of H_{c2}: singlet in a weak field regime, but triplet in a high field regime.[166] Kuroki *et al.* also predict the competition depending on the size of off-site Coulomb interaction using effective single band mode.[167] More recently, Zheng *et al.* measured a ^{59}Co Knight shift due to spin susceptibility, being substantially large and anisotropic, in a single crystal.[168] The shifts along both a- and c-axis directions decrease below T_c, indicating spin singlet pairing.

Second, for the spatial part of superconducting pairing, Higemoto *et al.*[169] have observed no breaking of time reversal symmetry through ZF-μSR studies, excluding a $p + ip$-wave pairing (one of pairings theoretically suggested). ^{59}Co NMR studies by Kata *et al.* show invariant behavior of the Knight shift in high field ($\sim$7 T) below T_c and suggest a p- or f-wave pairing.[44]

Most theoretical predictions,[167, 170, 171, 172, 173] whether singlet, triplet, odd gap, p-wave, or f-wave, have been based on six small cylindrical Fermi surfaces forming along the Γ-K lines. Although the Fermi surfaces have been predicted by LDA calculations[76, 82], however, ARPES studies have been not observed these surfaces so far (see below).[174, 175, 176, 177] Recently, Kuroki et al. modeled the superconductivity from an assumption of no e'_g Fermi surfaces.[178] The assumption is of two Γ-centered Fermi surfaces having the a_g character. Their model of a_g originated superconductivity shows an unconventional s-wave pairing with a gap which changes its sign between the Fermi surfaces.

3.2.3 Normal state

Fermiology

Within LDA, Singh[82] at x=0.5 and my calculations[76] at x=1/3 produced two kinds of Fermi surface with very simple and strong two-dimensionality (cylindrical shape). One is a Γ-centered large cylinder having mostly a_g character, and another is six small cylinders near the K point in the hexagonal Brillouin zone. The latter has largely e'_g character and is a main gradient to model a mechanism of the superconductivity by several groups (as said previously). However, ARPES measurements for x=0.7 and x=1/3

have observed renormalization of the t_{2g} band width and more strikingly no e_g' Fermi surfaces.[174, 175, 176, 177]

At first, Zhang *et al.*[179] suggested the e_g' Fermi surfaces can disappear due to modest correlation strength: U_c=2 eV for low x and U_c=4 eV for large x. The critical values (dependent on x) are consistent with U_c for charge disproportionation suggested by my group.[76] Using the fluctuation-exchange approximation, Yada and Kontani claimed that for small $J(\sim U/10)$ strong AFM fluctuation emerges due to nesting and subsequently absence of the Fermi surfaces is required to reproduce the observed pseudogap behavior.[180, 181] (For no AFM fluctuation, the Fermi surfaces always exist in these models.) Although the models accounted for absence of the Fermi surfaces, they did not seem to explain well the bandwidth renormalization. Zhou *et al.* used the multiorbital Hubbard model within the Hartree-Fock and strong-coupling Gutzwiller approximations.[182] Both approximations explained why ther are no e_g' Fermi surfaces, but only the Gutzwiller approximation accounted for the bandwidth renormalization. On the contrary, Ishida, Johannes, and Liebsch showed the Fermi surfaces are stabilized by dynamical correlations through dynamical mean field studies.[183] More recently, Singh and Kasinathan claimed the Fermi surfaces are destroyed by Na disorder.[107] So far, this seems to be one of the important questions, still controversial, in the cobalates.

Insulating AFM phase at x=0.5

Since Foo *et al.* first observed a charge-ordered insulating phase precisely at x=0.5,[53] there have been many attempts to reveal the mechanism. As the temperature is lowered, a kink in the in-plane susceptibility χ_{ab} at T_{c1}=88 K signals antiferromagnetic

Table 3.1. Temperature dependent change in $Na_{0.5}CoO_2$. For details, see the text.

Temperature (K)	phenomena
T_{c1}=27	· sample dependence
	· (no) kink in χ_{ab}
	· (no) kink in ρ(T) or more highly insulating
	· commonly no entropy change
T_{c2}=52	· so called charge-ordered T
	· gap opening ~15 meV
	· kink in χ_{ab} and χ_c
T_{c3}=88	· kink in χ_{ab}
	· on-set AFM ordering (T_N)

(AFM) ordering of some Co spins.[53, 71, 72, 184] Infrared reflectivity studies[51, 185, 186] detect a gap of ~15 meV opening below T_{c2} = 52 K, where Foo *et al.* observed[53] the onset of insulating behavior in the resistivity $\rho(T)$. T_{c2} has been called the charge-ordering temperature but there is also additional magnetic rearrangement, signaled by a kink in the in-plane susceptibility χ_{ab} and the c axis susceptibility χ_c.[71, 72, 187] At T_{c3}=27 K Gašparović *et al.* observed an additional kink in χ_{ab} with no signature in $\rho(T)$; this is the temperature where Foo *et al.* had observed structure in $\rho(T)$ reflecting more highly insulating behavior.[53] Unlike the upper two transitions, there is no entropy change[109] at T_{c3}.

There are still some controversies for the AFM spin-ordering pattern at x=0.5.

(I will address in some details in Sec. 3.6.) Although Na zigzag ordering pattern has been reported,[188, 189, 190] Co ions seem to be ordered in stripe patterns.[188, 190, 191] Besides, Mendels *et al.* suggested a *A*-type AFM ordering as around x=0.75.[191] The Co charge-ordering pattern was unclear until neutron scattering studies showed a out-of-phase stripe AFM ordering in the Co layers (and also antiferromagnetic ordering along the c direction).[71, 72] However, the neutron studies cannot provide Na ordering pattern, resulting in making it impossible to decide how crucial Na-Co interaction in the system is for Co charge-ordering. Although my first principles calculations using the LDA+U method have achieved successfully both patterns, Co zigzag and stripe orderings, by breaking the symmetry of the Co sites,[74] it will be a further challenge for theorists to clarify whether the Na zigzag ordering produces a Co stripe pattern.

Magnetic Tendencies around x=0.75

Although the region $x > 0.5$ phase has been interesting initially due to high thermoelectricity, the various magnetic behaviors have stimulated much of interest. The cobaltates show strong x-dependent magnetic variation: roughly, nonmagnetic around x=0.35, AFM at x=0.5, nonmagnetic around x=0.65, *A*-type AFM between x=0.75 and 0.82,[192, 193, 194, 195] and an incommensurate spin density wave at x=0.9.[196] At x=0.7, Wang *et al.* suggest FM fluctuation to interpret two interband transition peaks.[197] Also, Ihara *et al.* indicate magnetic crossover dependent on temperature: FM fluctuations below 100 K and AFM fluctuations below 4 K.[198] There are another reports to claim a spin density wave around T=22 K.[199, 200] Theses various behaviors may be understood by observations of Luo *et al.* which show a metamagnetic transition

from AFM state to FM state at applied magnetic field 8 T at low temperature, indicating both states can be realized in the low temperature.[201] It is still an unanswered question why magnetic properties depend on x in the cobaltates and the existing AFM states are (seemingly) 3-dimensional in such a strongly 2-dimensional system.

3.3 Na_xCoO_2 in Weakly Correlated Limit

3.3.1 Method of calculation

My calculations have been based on the hexagonal structure, containing double CoO_2 layers and having lattice constants a=2.84 Å, c=10.81 Å, obtained by Jansen and Hoppe.[98] (The end member CoO_2 has considerably different lattice constants which will be specified below.) In most of the calculations, a single layer cell is chosen unless said otherwise, because the system has been observed to have very small interlayer coupling. In this section, the Na atom in Na_xCoO_2 was treated within the virtual crystal approximation (VCA): Na nuclear charge Z=10+x. In the treatment, leading to space group $P\bar{3}m1$ (No. 164), atomic positions are Na at 1b site (0,0,1/2) above and below the Co site at 1a site (0,0,0). Oxygens sit at 2d site (1/3,2/3,z_0). The O height z_0=0.168(c/2)=0.908 Å, relaxed within LDA by Singh, was used. It produces the Co-O-Co bond angle 98.5° (this angel would be 90° for undistorted octahedra).

In the section, we used the LDA method, implemented in the FPLO code (version 5). Valence orbitals included Na 2s2p3s3p3d, Co 3s3p4s4p3d, and O 2s2p3s3p3d for all calculations in Na_xCoO_2. The Brillouin zone was sampled by k-mesh containing 202 irreducible k-points.

3.3.2 Electronic structures at x=1/3

Nonmagnetic state

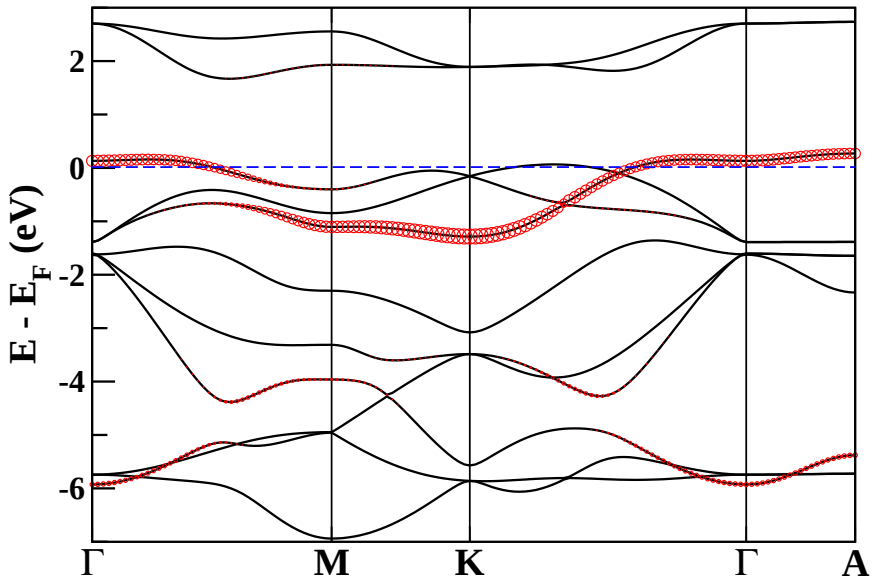

Figure 3.5. LDA PM band structure of $Na_{1/3}CoO_2$ in the virtual crystal approximation. The Co e_g manifold lies around 2 eV, whereas the t_{2g} manifold lies between -1.3 and 0.3 eV. The six O $2p$ bands lie below -1.5 eV. The thickened (and red colored) lines emphasize strong a_g character. The horizontal dashed line indicates the Fermi energy.

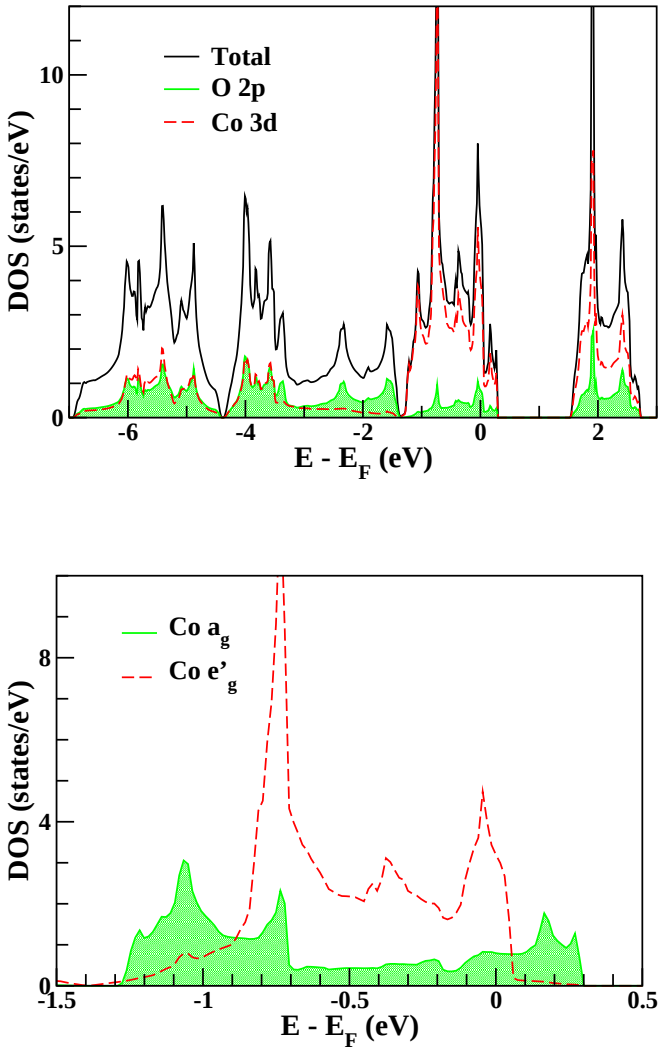

Figure 3.6. Top panel: Total and atomic-projected DOS for LDA PM $Na_{1/3}CoO_2$. The crystal field splitting between the unoccupied e_g and partially occupied t_{2g} manifold is 2.5 eV. The Co $3d$ states show considerable hybridization with the O $2p$ states, which can be seen by the $3d$ character in the O $2p$ region (below -1.5 eV) and vice versa. Bottom panel: Orbital projected DOS for Co e_g' and a_g characters near E_F. The a_g and e_g' states differ a little in width. although both states have indistinguishable centers. Nearly all of the e_g' states lie within 1.0 eV range, while the a_g bands spread over 1.5 eV.

As said previously, superconductivity is been observed around x=1/3 through intercalating water, so that it is important to investigate first the normal state (without water). First I will address the electronic structures for the nonmagnetic phase in the normal state. The $e_g - t_{2g}$ crystal splitting of 2.5 eV, which can be seen in the band structure and corresponding DOS given in Figs. 3.5 and 3.6 respectively, designates the unoccupied e_g states with width of 1 eV well out of consideration for most low energy effects. The t_{2g} manifold, which lies in the range of -1.3 to 0.3 eV and is intersected by the Fermi level, can be broken into singlet a_g + doublet e'_g by the hexagonal ligand field. The a_g state is highlighted by the thickened (and red colored) line using the "fatband" representation shown in Fig. 3.5. The symmetry-breaking in the t_{2g} manifold can be seen in the orbital-projected DOS for the e'_g and a_g states displayed in bottom panel of Fig. 3.6. The centers of both states are almost identical, but nearly all of the e'_g states lie within 1.0 eV range whereas the a_g bands extend over 1.5 eV.

It is of interest to view the band structure through a single isolated tight-binding picture to model the a_g band dispersion of 1.5 eV width. The dispersion corresponds to an effective hopping parameter t=0.16 eV. Although the a_g band dispersion resembles that of the simple tight binding model, the a_g projected DOS (shown in the bottom panel of Fig. 3.6) is nothing like that of the model. There are two reasons;(1) mixing with the e'_g bands through most of the Brillouin zone even though the hybridization is less evident along the K-Γ line than along the M-Γ line, and (2) the actual shape of the DOS comes from significant 2nd-neighbor hopping. Rosner *et al.* show that the 2nd-neighbor hopping makes the a_g band near the Γ point much flatter than in the tight-binding model.[202]

It is worthwhile to clarify some details of the a_g band near the Γ point. Interlayer

coupling would be expected to be suppressed near k=0, but the upward dispersion of the a_g band seems to be affected by the interlayer coupling. (For details, see the enlarged band structure shown in Fig. 3.8.) Johannes and Singh have reported[125] the upward dispersion even for the hydrated system, which has 80% larger separation between CoO_2 layers than in the dehydrated system and nearly zero of interlayer coupling.

Magnetic tendencies

Although no ferromagnetism has been observed in the system (except AFM at x=0.5 and A-type AFM[6] at x=0.7−0.9), Singh found that FM phases always seemed to be energetically favored for all noninterger x.[82, 203] So Na_xCoO_2 becomes another member in small but growing number of systems (for example, $ZrZn_2$, Sc_3In, and Ni_3Ga), whose tendency toward FM is overestimated by LDA because they are near a magnetic quantum critical point.[203, 204] In Na_xCoO_2 having the two-dimensionality that quantum fluctuation is an important aspect, the x=1/3 system may be a "fluctuation-induced paramagnet" due to lack of consideration of the effect of fluctuations in the electronic structure calculations.

My calculations confirmed the FM tendencies, a half metallic FM state with a magnetic moment $\frac{2}{3}\mu_B$/Co for x=1/3. The FM energy gain is about 45 meV/Co. The minority bands are metallic, and the Fermi level lies just above the top of the fully occupied majority states. The exchange splitting of the t_{2g} states is 0.5 eV, consistent with Singh's result.[82] Considering the minority t_{2g} bands filling of $\frac{2}{3}$ for the half metallic FM states, the FM phase has larger e'_g hole than for the PM states, which suggests a multiband

[6]In the A-type AFM ordering, the interlayer coupling is antiferromagnetic, while the intralayer coupling is ferromagnetic.

(a_g+e'_g) behavior rather than a popularly assumed single a_g behavior for around x=0.3 regardless of magnetic states. My attempts within LDA to obtain an AFM state within the CoO_2 layer always converged to the nonmagnetic or FM states.

Fermiology

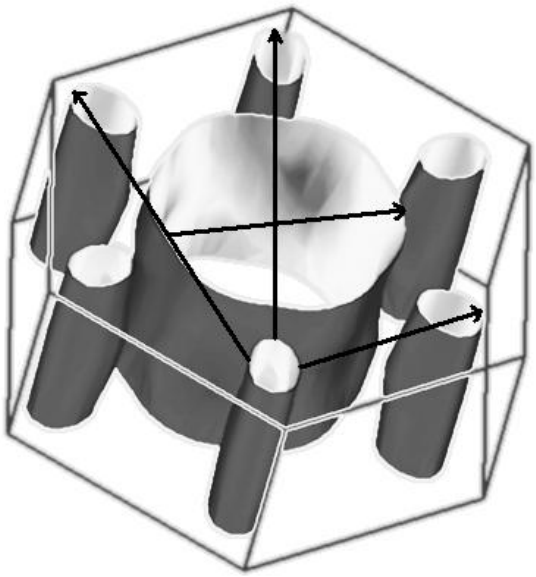

Figure 3.7. PM Fermi surface at x=1/3 (VCA). The Γ-centered large cylinder contains 0.43a_g holes/Co, while each six small cylinder holds 0.04 holes/Co which has mainly e'_g character. The total is the 0.67 holes.

The PM Fermi surface (FS) shown in Fig. 3.7 is consistent with the x=0.5 one given by Singh.[82] A lage Γ-centered cylinder (mean radius K_F) shows some flattening in the perpendicular direction to the Γ-K line. The six small cylinders (radius k_F) has become a central component of several models of the superconducting phase, as noted earlier.[170, 171] The total holes of 0.67 corresponds to the amount required by Luttinger's

theorem to account for the x=0.33 system. This FS geometry leads to several interesting features. There are three distinct intercylinder nesting vectors, as depicted in Fig. 3.7, to translate one of the small cylinders into another. If these cylinder with an eccentricity of 1.25 were perfect cylinders, these vectors would represent strong nesting vectors leading to charge- or spin-density waves. There are additional processes corresponding to $Q \leq 2K_F$ of the large cylinder.

3.3.3 Variation dependent on sodium concentration

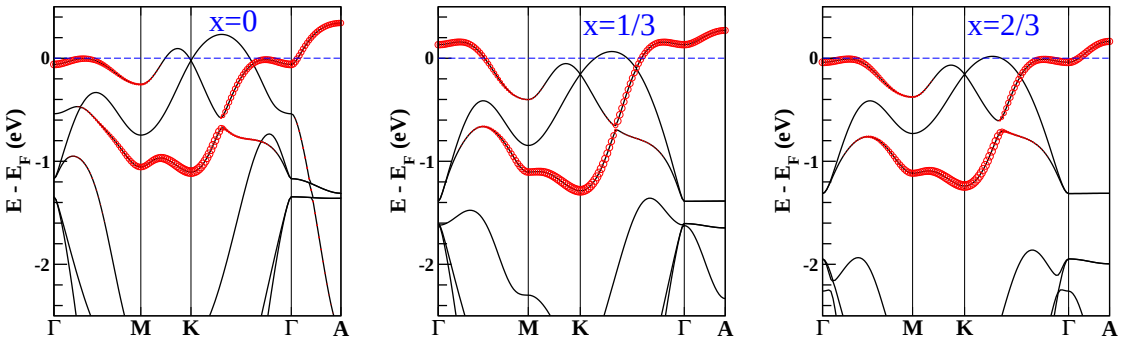

Figure 3.8. LDA PM blowup band structures near t_{2g} manifold at x=0, 1/3, and 2/3. The $t_{2g} - e_g$ crystal-field splitting of 2.5 eV remains unchanged regardless of x, so that the e_g states lie out of consideration (and out of these figures) for most low energy effects. Although the system is strongly 2-dimensional, the a_g bands (the top of the valence bands) show some dispersion along the c direction. The thickened (red colored) lines highlight the bands with strong a_g character. Lattice constants a=2.8048 Å, c=4.2509 Å and the oxygen height z_0=0.235 (0.999 Å) are used at x =0, while a=2.84 Å, c=5.405 Å, and z_0=168 (0.908 Å) at x =1/3 and 2/3.

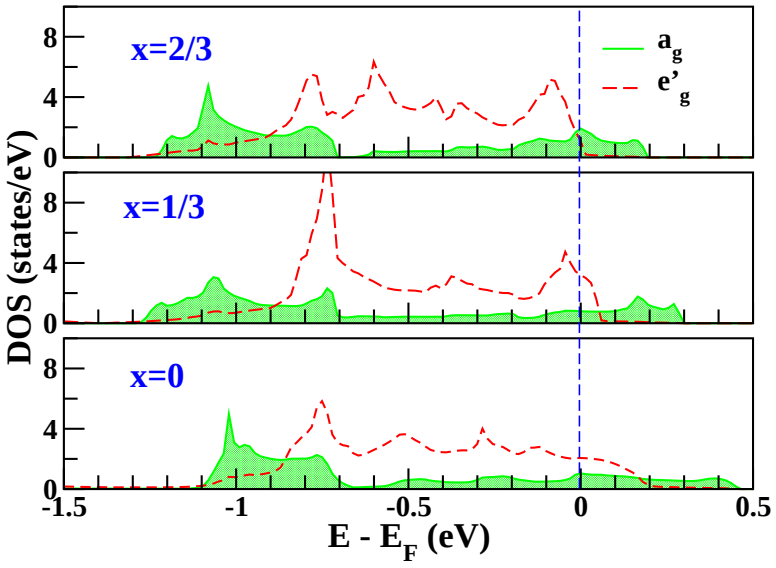

Figure 3.9. Orbital-projected DOS of the a_g and e'_g states for x=0, 1/3 and 2/3. Holes doped into the band-insulating $NaCoO_2$ phase go initially into the a_g band, and enter only the band until x ~0.6 where the e'_g holes begin to emerge.

The enlarged band structures near E_F with the emphasized a_g character (d_{z^2}, where z is perpendicular to the CoO_2 layer) using the "fatband" representation at x=0, 1/3, and 2/3, and corresponding orbital-projected DOS of the a_g and e'_g states are given in Figs. 3.8 and 3.9, respectively. The a_g band has strong character at the bottom of the t_{2g} manifold as well as at the top. Holes doped into the band insulating phase $NaCoO_2$ enter only the a_g states until x ~0.6 where an e'_g Fermi surface starts to emerge, as illustrated clearly in Fig. 3.9. Considering the indistinguishable centers of the a_g and e'_g states, this distinction is due to a little larger band width of the a_g band. In addition, increasing hole doping, i.e., decreasing x, produces several important aspects. The Co-O bond length at x=0 is 2.5% larger than at the others, suggesting less Co-O

coupling. However, the O $2p$ states move toward the t_{2g} complex, implying the $d-p$ mixing is strongest at x=0, because the decrease in mixing due to t_{pd} is compensated by the decrease in the $\varepsilon_{t_{2g}} - \varepsilon_p$ energy separation. It can be also come from a change in the Madelung potential, and rehybridization of Co $3d$ and O $2p$ states.[124] Second, as can be seen clearly in Fig. 3.9, the width of the t_{2g} complex shows some change, becoming a little narrower, i.e., more localized, as x increases. It is consistent with my suggestion that the on-site Coulomb repulsion depends on x (see Sec. 3.7, for details). As x increases, the downward movement of the O $2p$ states and little change of the t_{2g} manifold lead to increasing $p-d$ separation around -1.5 eV. The reason is still unclear in detail, whether it is due directly to change of carrier concentration $(1-x)$ or indirectly through change of the Co−O bond length. In the CoO_2 system, my calculation shows that a change of the Co−O bond length (keeping everything else fixed) hardly affects the separation, implying decreasing holes (or increasing electrons) has responsibility for the separation (see Sec. 3.5). However, another calculation for $Na_{0.5}CoO_2$ exposes that the separation decreases monotonically as the Co−O bond length increases (see Sec. 3.3.4). Third, as expected from 20% smaller c lattice constant and 25% larger Co−O bond length at x=0, the a_g band along the Γ-A line at x=0 has twice larger dispersion, about 200 meV, than in the others. This dispersion indicates a reduction of quasi-two dimensionality at x=0. A change of the a_g band dispersion along the Γ-A line between x=1/3 and 2/3 is little. As a result, it suggests that the amount of doped holes (or electrons) hardly affect the quasi-two dimensionality in the system.

3.3.4 Effect of change of the Co-O bond length

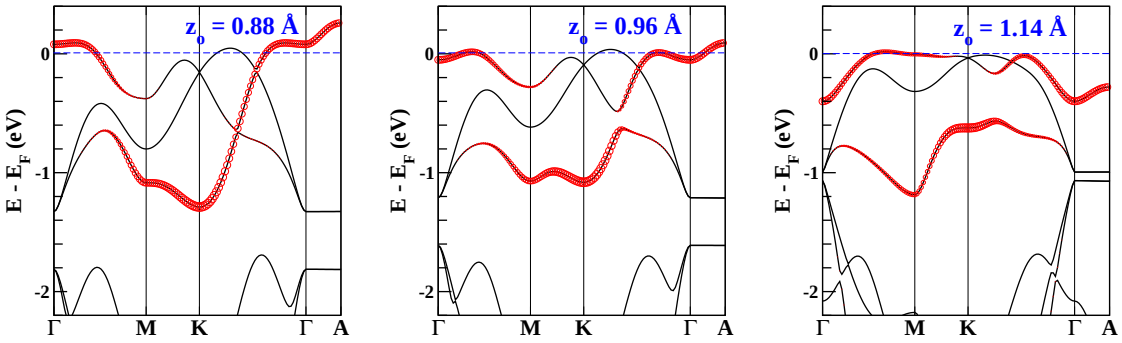

Figure 3.10. Effect of the O height z_0 on the t_{2g} bands of PM $Na_{0.5}CoO_2$ in the VCA. In the calculation, we used 20% larger c lattice constant than the experimentally observed value to remove unphysical O−O interlayer interaction as the O position was varied. The value z_0=1.14 Å corresponds to perfect CoO_6 octahedra. The thickened line emphasizes the a_g character. The horizontal dashed lines indicate E_F.

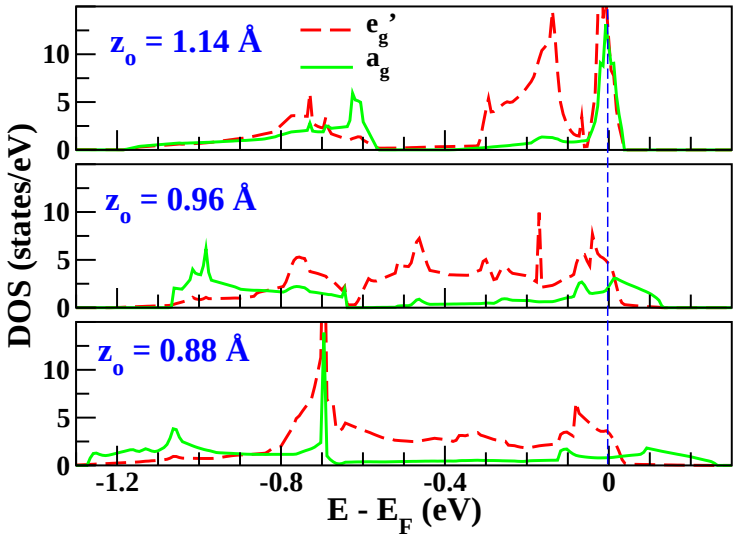

Figure 3.11. Effect of the O height z_0 on the orbital-projected DOS of the a_g and e_g' states. For the undistorted CoO_6 octahedra (1.14 Å), the a_g and e_g' bands have the same amount of holes, but below E_F the bands are considerably different from each other. However, the highly squashed case, the doped holes go into the a_g state before encountering the e_g' state. It should be noted that the densities of states are already different from each other near the Fermi level even for unsquashed octahedron. The vertical dashed lines indicate E_F.

I address next the effect of the O height.[7] The O height has been reported in range of 0.96 and 1 Å in the normal state ($0.33 < x < 1$), whereas the superconducting phase intercalating water has about 0.88 Å. Additionally, when intercalating D_2O ions instead of H_2O, the O height is in 0.90−0.95 Å range. To elucidate the question of the effect of squashing, I present the change of the t_{2g} bands and corresponding orbital-

[7] When using artificially large lattice constant, it tends for Na atom to be isolated, leading to nonphysically neutral Na atom rather than Na^+ ion in the system. It indicates that careful monitoring in the case is required.

projected DOS for O height (from the Co layer) of 1.14 Å (corresponding to perfect CoO_6 octahedra), 0.96 Å (typical value for intermediate x), and 0.88 Å (the smallest value reported) in Figs. 3.10 and 3.11.

Simple crystal-field analysis based on negatively charged O ions would suggest:(1) the a_g and e'_g DOSs should be the same for the perfect octahedron, and (2) the e'_g states should rise relative to the a_g band as the Co-O bond length decreases. My calculations show that these expectations are severely disobeyed. In fact, the effects of squashing are much complicated than what suggested by the crystal-field model. The mean energies of the a_g and e'_g bands are nearly identical, and remain unchanged for the squashed O height. The most remarkable change is in the a_g band width, compared with the e'_g band width. At the highly squashed end, doped holes can go into the a_g band before facing the e'_g bands. As seen in band separation around -1.5 eV, the squashing decreases $d-p$ interaction.

The changes in the band structure of Fig. 3.10 are more informative. For the cubic octahedron (z_0=1.14 Å) at the Γ point the a_g band lies around -0.4 eV, and the maxima occur midway along both Γ-M and Γ-K lines instead of the A point. The e'_g bands also display considerable changes not only in the Γ point but also in the degeneracy at the K point, on squashing. This behavior is similar to the result of a multiorbital Hubbard model using the fluctuation-exchange approximation with a variable of the $a_g - e'_g$ crystal field splitting (estimating distortion of CoO_6 octahedron) by Mochizuki *et al.*[205] However, my result at the Γ point is much more dramatic, while for both approaches the small e'_g hole FSs forming along the Γ-K line vanish as the octahedron is close to being ideal.

3.4 Charge Disproportionation

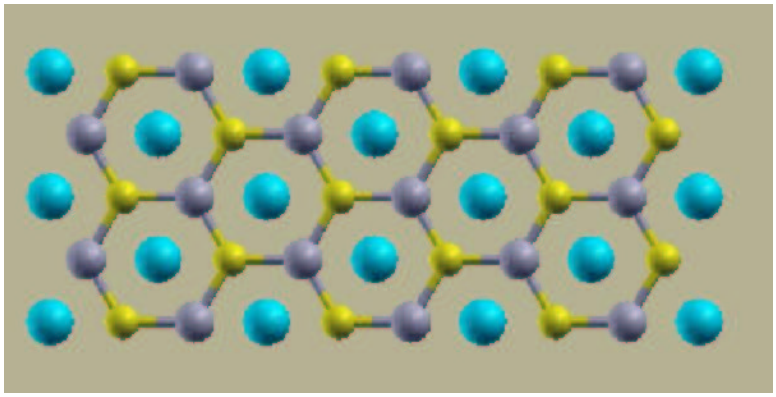

Figure 3.12. Depiction of CD and spin ordering in the $\sqrt{3} \times \sqrt{3}$ supercell used for x=1/3 and 2/3. In the supercell (space group $P31m$, No. 157 for FM ordering), Na atoms at $1a$ site (0,0,1/2) lie above/below the Co site at the $1a$ site (0,0,0). The other Co sites are $2b$ (1/3,2/3,0). Oxygens are at $3c$ site (2/3,0,$\bar{z}_0$) and $3c$ site (1/3,0,z_0) positions. The unconnected large blue spheres indicate S=0 Co^{3+} ions, while the connected spheres represent oppositely directed S=1/2 Co^{4+} when allowing AFM ordering.

As often occurs in transition metal oxides, in this system LDA cannot explain several important features. There are three important failures of LDA which request to include correlation effects;(1) favoring FM within LDA for all noninteger x although a FM is favored only for $0.7 \leq x \leq 0.9$, (2) existing e_g' cylindrical FS below x=0.5, and (3) no charge disproportionation (CD)[8] at x=0.5. In this section, I will focus on the issue of CD by applying the LDA+U method to model correlation effects. (Although it is well known that increasing U drives local orbital occupations to integral occupancy, there have

[8]Strictly, CD is different from charge ordering (CO). For example, when $M^{(4-x)+} \rightarrow xM^{3+}+(1-x)M^{4+}$, it is called charge disproportionated state. On the other hand, CO means to arrange different type ions in a mixture such as $xM^{3+}+(1-x)M^{4+}$.

been only a few pioneering applications, including mine, of correlated band theories to model CD.[73, 76, 206, 207, 208] In view of formal charge, Na_xCoO_2 consists of $x$$Co^{3+}$ + $(1-x)Co^{4+}$. But, within LDA, there are only one-type $Co^{(4-x)+}$ ions. Since Co has low spin configuration in the system,[97] Co^{3+} is S=0 nonmagnetic ion whereas Co^{4+} is S=1/2 magnetic ion. At first, I will show that moderate values of U drive CD at both x=1/3 and 2/3. x=1/3 is near the superconducting composition, while x=2/3 lies on the region ($x \geq 0.5$) that shows correlated behavior. In the calculations, a $\sqrt{3} \times \sqrt{3}$ supercell, leading to three Co sites, was used, as shown in Fig. 3.12. Second, I will address microscopic behaviors at $x = 0.5$, which shows a metal-insulator transition at T= 52 K, using a two Co supercell. According to my studies, the sodium cobaltates seem to be in an intermediate regime where the both popular schemes, AMF and FLL, (see Sec. 2.3) of the LDA+U functional supply similar results. (Because of this similarity, in this section I will show only figures obtained from the AMF scheme appropriate for relative small U and small moments since the system is metallic except precisely at x=0.5.) The similarity may come from small spin polarization, resulting in small difference in the double counting correlations. So far, there is no agreement on the best value of U in the system. Thus, the Coulomb repulsion U was varied within realistic range, while the intraatomic exchange integral J=1 eV remained fixed.[9] So in the LDA+U calculation, strength of U is varied. But, in a small range, varying U will be analogous to applying pressure which changes the U/W ratio. Hence, I expect my predictions to be detected by high pressure research.

[9]There is some dispute about the effect of Hund's rule exchange parameter J. In general, however, J is affected only little by screening effects, so that atomic value J=1 eV is accepted popularly in most systems without physically significant change in results.

3.4.1 Macroscopic behavior

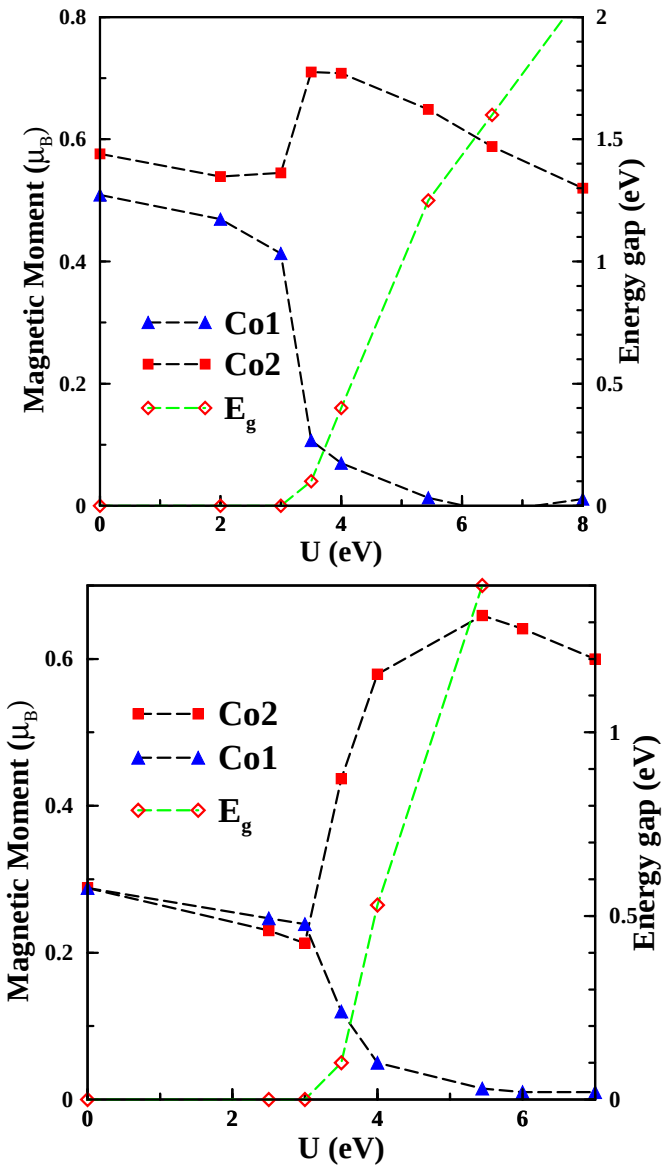

Figure 3.13. Effect of U on the Co magnetic moments and energy gap at x=1/3 (top) and 2/3 (bottom) in FM ordering. Changes in the magnetic moments show that charge disproportionation (CD) begins at U_c=3 eV for both cases. Above U_c, in view of the formal charge, Co1 becomes nonmagnetic Co^{3+}, while Co2 is magnetic Co^{4+}. In addition to CD, gap opening occurs simultaneously at U_c.

First, I studied the behavior for x=1/3 and 2/3. Changes in the Co magnetic moments and energy gap due to U for FM ordering are given in Fig. 3.13. At x=1/3, in LDA ($U \rightarrow 0$ limit), the difference between magnetic moments of both Co ions (Co1 and Co2) is very small, only less than 0.1 μ_B. (Note Na sits above Co1.) Before CD occurs at U_c=3 eV, Co1 and Co2 have similar magnetic moments to the LDA values. The magnetic moments show dramatic change above U_c, and CD into Co^{4+} (S=1/2) and Co^{3+} (S=0) ions is evident at U=3.5 eV. CD is accompanied by a metal-insulator transition (MIT), from half-metallic to insulating phase in this case, at U_c. The energy gap increases linearly at the rate of dE_g/dU=0.6 above U_c. Co2 has a maximum magnetic moment of 0.7 μ_B at U=4 eV, while Co1 has nearly zero magnetic moment around U=6 eV.

At x=2/3, the Co magnetic moments decrease slowly and are nearly identical with the LDA values below U_c=3 eV, where CD occurs suddenly. CD develops more slowly than at x=1/3, and is complete at U=4 eV. Co2 has a maximum magnetic moment of 0.63 μ_B at U=5 eV. As at x=1/3, gap opening occurs simultaneously at U_c=3 eV. Above U_c, the gap increases linearly at the rate of dE_g/dU=0.67, similarly to the x=1/3 case.

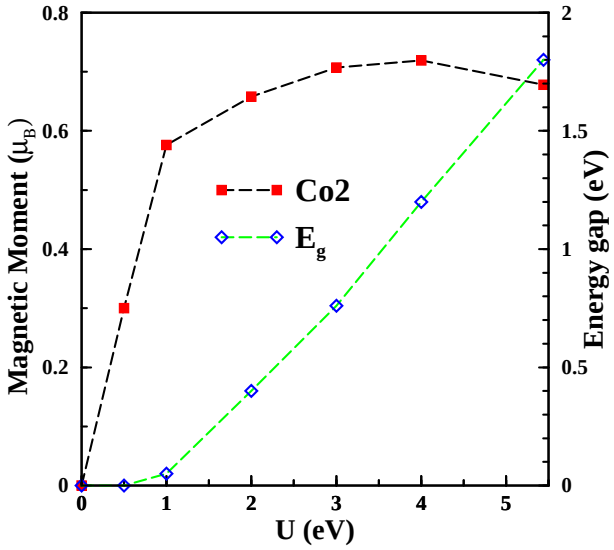

Figure 3.14. Effect of U on the Co magnetic moments at x=1/3 in AFM ordering. CD and gap opening occur at U_c=1 eV. The magnetic moment of Co1 is zero by the symmetry. Note that my attempts to obtain an AFM solution within LDA always converge to a nonmagnetic solution. Applying even small U, AFM ordering is recovered, although the gap only opens around U=1 eV.

When allowing AFM order in Co^{4+} (Co2) ions, the analogous calculation can be carried out. (In my choice of supercell, there is only one Co^{4+} ion at x=2/3, so only FM ordering can be considered.) The results for x=1/3 are shown in Fig. 3.14. On applying U, the magnetic moment of Co2 increases rapidly from zero moment. The Co1 magnetic moment remains zero for all U due to symmetry. The gap opens just around U=1 eV and grows at the rate of dE_g/dU=0.4. It is found that for AFM ordering at x=1/3 U_c is no higher than 1 eV. This easy gap opening is obviously stimulated by the narrower bandwidth of the unoccupied a_g band than in the FM case. A spin-up Co2, having six nearest neighbors, is surrounded by three spin-down Co2 and three Co1 ions. (It has

no spin-up Co2 nearest neighbor.) The nonzero bandwidth of the a_g band reflects the effective hopping between the a_g states of second neighbor Co ions.

There has been an earlier report[209] very different from my results showing CD at U_c=3 (FM) and 1 eV (AFM). In the earlier report, where symmetry breaking by CD was not allowed, change was very little even for large U. The difference implies that LDA+U result can be altered by allowed degrees of freedom.

Considering thermal and quantum fluctuations, even at a rational concentration, CD and charge ordering (CO) may not occur simultaneously. In my calculation which neglects fluctuation and uses a small supercell ($\sqrt{3} \times \sqrt{3}$), CD is necessarily coincided by CO. As a result, it leads to a honeycomb lattice of spin half ions, but the lattice relieves possible frustration due to CD. Accounting for CD, according to the Mullikan charge decomposition[10] in the FPLO method, the charges on the distinct Co sites differ by only $0.25 - 0.3$ electrons, much smaller than difference in the formal charges. The small value reflects the well-known knowledge that the formal charge designation does not represent actual charge correctly though the viewpoint of formal charge is very useful for physical understanding.

[10]The charge density in the nonorthogonal local basis consists of two contributions, net and overlap. While the former contains only products of the same-site basis function, the latter does products of basis functions from different sites. In the Mullikan charge decomposition, the overlap term is distributed equally to each site.

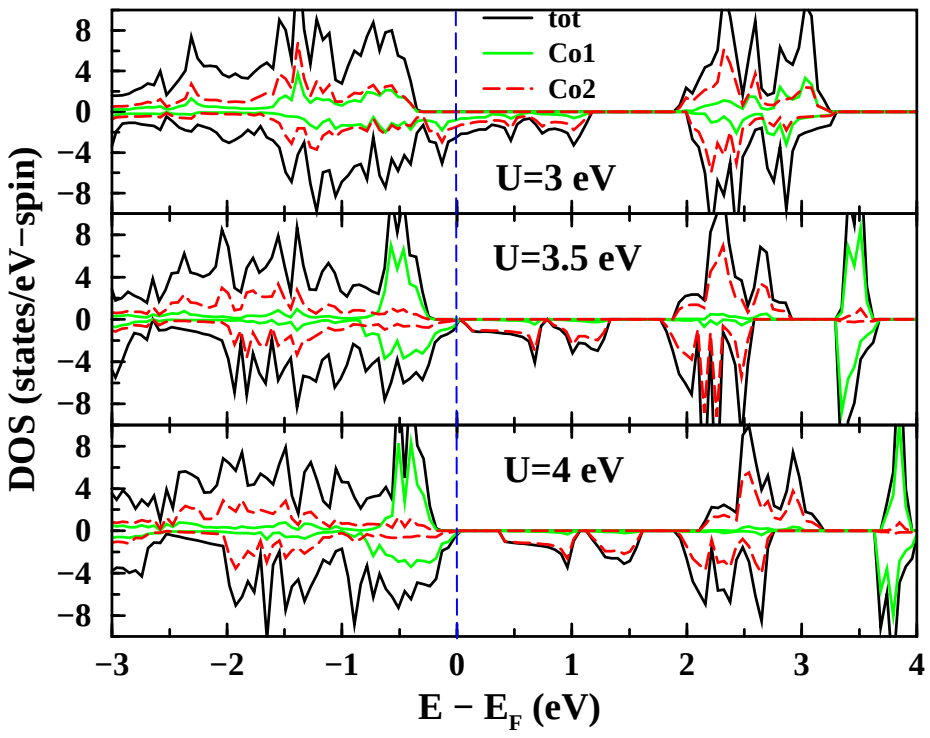

Figure 3.15. Progression of the Co1 and Co2 3d projected DOS in the critical region for x=1/3 in FM ordering. The middle panel for U=3.5 eV shows that the a_g minority state of Co2 (upper Hubbard band) starts to split off from the valence (occupied) state. Note that the progression starts from a half-metallic state.

Although CD, CO, and gap opening are expected physically to be closely related, it is unclear why the phenomena should occur simultaneously in this LDA+U calculation. The development of the Co1 and Co2 3d projected DOS for FM x=1/3 as CD occurs is given in Fig. 3.15. In LDA, the system shows a half-metallic behavior, which survives up to U=3 eV. The gap opening occurs just when the minority a_g band splits off from the valence band. At the point, the minority a_g bands containing 2/3 holes per Co split into an unoccupied band containing one hole for each Co^{4+} ion and an occupied band of Co^{3+}

ions. This CD can be classified by dramatic movement of bands around -0.6 to -0.3 eV along with seemingly continuous changes in 0–1 eV region. In principle, CD can occur before the gap opens, although it does not happen in these cases. (It has been realized at x=1/2 that CD occurs before gap opening, when using a bigger supercell which allows charge disproportionated AFM state. See Sec. 3.6.)

Additionally, one might expect CD to couple to the lattice. Considering the radii of Co^{2+} and Co^{3+} differ by 15% (0.74 Å and 0.63 Å), CD into the charge states can be expected to couple strongly with local oxygen mode. However, radius of the Co^{4+} ion is indistinguishable from that of the Co^{3+} ion in octahedral coordination. Thus, the coupling may be little even for Co^{3+}-Co^{4+} charge disproportionated configuration.

3.4.2 Microscopic mechanism

In Na_xCoO_2, I address a question of correlation versus band-filling effects in a multiband system with Na_xCoO_2. In this system, the effects relate to the mechanism of CD-CO-MIT transition. In the previous subsection, I looked at the mechanism with the $\sqrt{3} \times \sqrt{3}$ supercell at x=1/3 and 2/3. However, while the rest of the phase diagram is metallic, this x=0.5 phase experiences a CO+MIT around 50 K. Thus this research, which studies more extensively the x=0.5 case, will be more informative. I used a two Co supercell, which allows for CD into Co^{3+} and Co^{4+} ions. This doubled supercell contains only one magnetic ion, so there is no issue of spin order except simple alignment. In this subsection, I will investigate overall the FM case. (For issue of the CD AFM, see Sec. 3.6.)

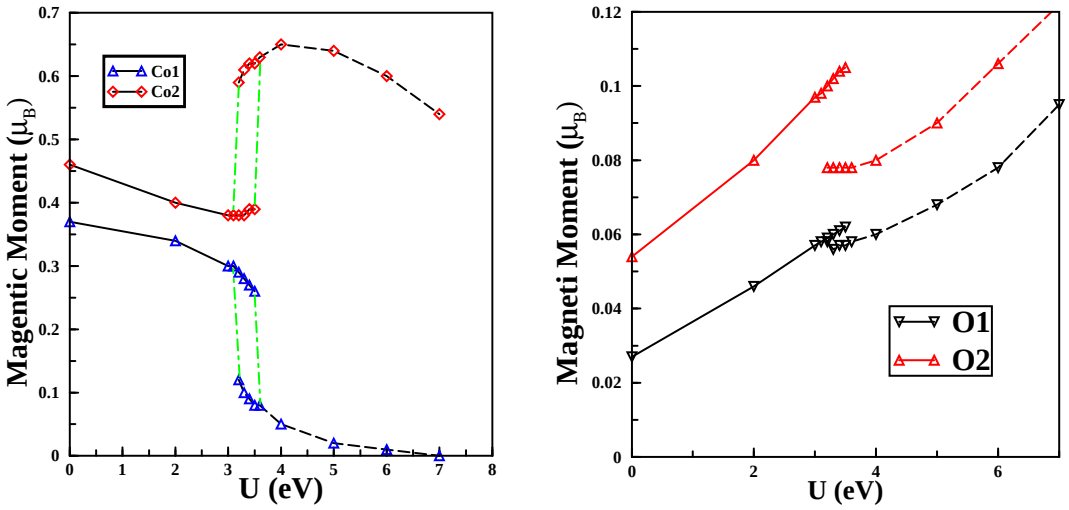

Figure 3.16. Effect of U on the magnetic moments of Co (left panel) and O (right panel) for FM $Na_{0.5}CoO_2$, using a two Co supercell. The supercell (space group $P2/m$) allows two ions, Co1 and Co2, to be realized in the cell. (The Brillouin zone was sampled with 306 irreducible $\mathbf{k}$ points.) The left panel shows that CD ($2Co^{3.5+} \rightarrow Co^{3+} + Co^{4+}$) and gap opening (metal-insulator transition) occur simultaneously due to a first-order transition at U_c=3.2 eV. Note that it is possible to follow hysteresis within the range $3.2 \leq U \leq 3.6$ eV, but outside this region only one of the states, the undisproportionated (UD) or CD states, is obtained. Solid and dashed lines denote UD and CD states, respectively. Right panel: charge transfer from Co to O results in a small increase in the O1 and O2 magnetic moments. O1 is the O site that is shared by two Co1 and one Co2, whereas O2 is shared by one Co1 and two Co2.

As reported first by Singh,[82] in LDA FM is favored energetically over the nonmagnetic state at x=0.5. The FM state has a total magnetic moment of 1 μ_B/doubled cell, which remains unchanged upon applying U though there is no presumed restriction.

The system shows half-metallic behavior in the metallic phase, i.e, below U_c, while a gap opens in the CD phase.

The effect of U on the Co magnetic moments is displayed in Fig. 3.16. In LDA, the Co ions have differing moments because the symmetry is already broken by the Na ordering. (The Na ions are ordered above the CD temperature.[101]) Increasing U, the both moments decrease slowly at the rate of $-0.025\ \mu_B$/eV, resulting from some charge transfer between majority Co and O. At U_{c2}=3.6 eV, the character of the solutions changes discontinuously, with a sharp change in the moments evidently identified with Co1$\rightarrow$Co^{3+} and Co2$\rightarrow$Co^{4+}. At U=4.5 eV, Co2 has a maximum moment, while Co1 is very tiny. Decreasing U, the magnetic moment undergoes sharp change again, but at slightly lower critical value of U_{c1}=3.2 eV. The solutions return to the initial undisproportionated (UD) state below U_{c1}. There is a 0.4 eV hysteresis region in this CD transition centered at U_c=3.4 eV. The hysteresis is different from the results at x=1/3 and 2/3 discussed in the previous section. At those concentrations, the hysteresis regime of deriving CD is inaccessible due to its higher energy than either UD or CD states. This CD first order transition is similar with low spin $\leftrightarrow$ high spin transitions in fixed spin moment calculations of two dimensional space of Co1 and Co2 magnetic moment. The fixed spin moment thechinique was considered first by Moruzzi *et al.*[26]

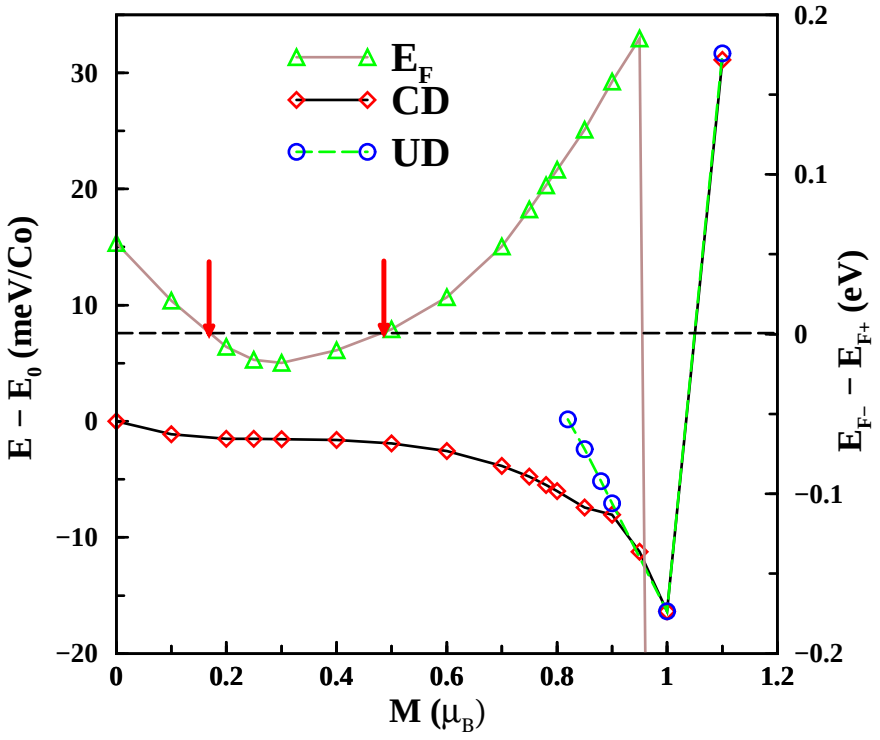

Figure 3.17. Fixed spin moment calculation for $Na_{0.5}CoO_2$ using a supercell containing two cobalts at U=3.3 eV. The total magnetic moment M is given in unit of μ_B/2Co. The left and right sides of the y axis indicate the total energy difference and difference between minority and majority Fermi energies, respectively. The arrows pinpoint zeros of the Fermi energy difference, corresponding to extrema of the energy (metastable state).

The two solutions can be probed in another way, using fixed spin moment (FSM) calculations within LDA+U in the critical region, as shown in Fig. 3.17. The energy vs. constrained total magnetic moment curve shows sharp jump at M= 1 μ_B, which is identical with the value obtained from the self-consistent calculations. As already noted by Singh,[203] this jump is due to the gap arising from the large $t_{2g} - e_g$ crystal field splitting. Interestingly, the energy vs. moment curve becomes two curves, in which one

state or the other is achieved depending on starting point. Comparison with Singh's LDA FSM results shows two main differences from my LDA+U FSM results. First, at M=0 μ_B, my system is AFM with the Co magnetic moment of 0.34 μ_B, while Singh started from a nonmagnetic state. Second, the plot is nearly flat at small M, whereas the LDA results show much steeper decrease. This nearly flat region has two extrema, a stable one at M=0.16 μ_B and an unstable one at M=0.5 μ_B, which can be identified from the zeros of the Fermi energy difference. Due to the trifling energy barrier, this small net energy moment minimum will be inaccessible experimentally.

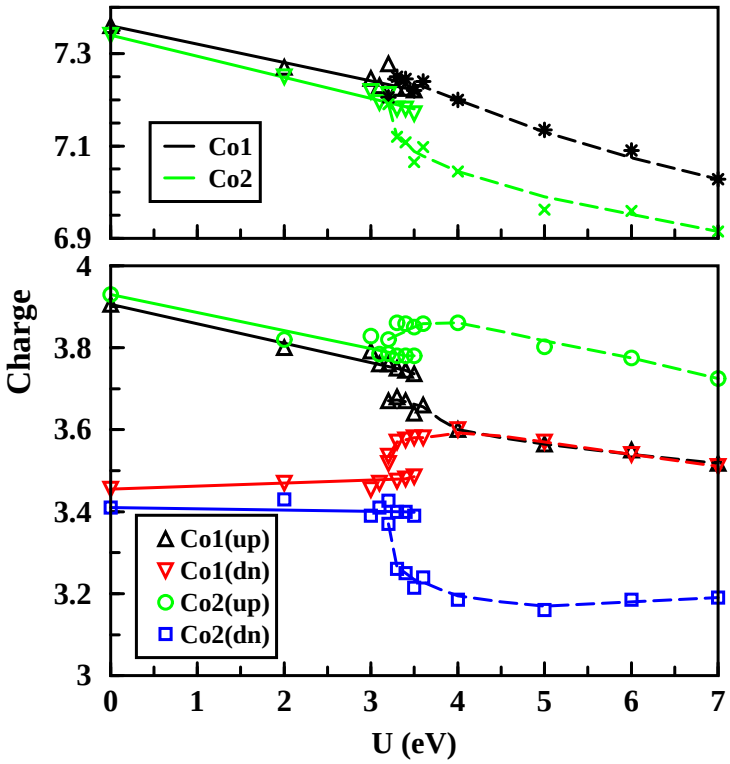

Figure 3.18. Change with U of d charge for the two Co ions. The top is for the total $3d$ charge and the bottom for the majority and minority charges separately. It is based on the Mullikan charge decomposition in the FPLO method.

At the CD transition, the Co1 charge is continuous, whereas the Co2 charge jumps by ∼0.1 electrons, as shown in the top panel of Fig. 3.18. The bottom panel of Fig. 3.18 displays the discontinuities in the majority and minority charges separately. The CD transition does not appear as strongly in the charge transfer as in the spin redistribution. In the CD state, the Co magnetic moments indicate clearly Co1→Co^{3+} and Co2→Co^{4+}, but the charge difference between the Co ions is only ∼0.15 electrons. Increasing U from zero, there is only small amount of charge transfer by $(0.04-0.05\ e/\text{eV})$ from Co ions into the O ions.

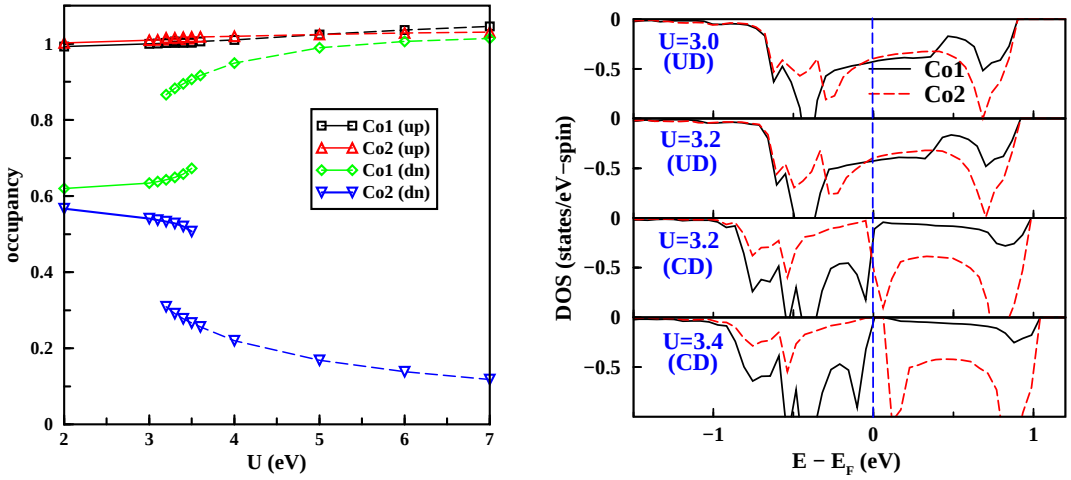

Figure 3.19. Left panel: Change of the occupancy of the a_g states versus U, revealing the strong a_g CD in the critical region. The minority states of both Co ions show a sharp jump at the transition, while the majority states are fully occupied regardless of U. Right panel: Effect of U on orbital-projected DOS of the minority a_g states for the Co1 and Co2 near the critical region. It discloses that CD arises from differentiation of the a_g minority states depending on U. As increasing U, holes of Co1 ion go into the Co2 ion. Note that the a_g majority states are fully occupied for all U. The e_g' states are magnetically dead before reaching the critical region.

The left panel of Fig. 3.19, picturing the change in the a_g occupation, shows clearly the charge rearrangement, i.e., spin redistribution. At the CD transition, a large charge transfer occurs from the minority a_g charge on Co1 to the majority charge on Co2. But, the total charge difference between the two Co sites is only a fraction of the transferred charge from the minority states, because it is compensated strongly by a rehybridization with the O ions and back polarization of the other $3d$ (e_g' and e_g) states. Although there is no large change in total charge, a large change in spin is realized due to the multiband character of the system near E_F.

The right panel of Fig. 3.19 shows the minority a_g orbital-projected DOS, lying within a l eV range from E_F, for the Co1 and Co2 near the critical regime. It reveals that movement of the a_g minority states due to the Coulomb repulsion U is a main cause of the CD transition. The a_g majority states are already occupied fully even at U=0. The e_g' states, which have a small amount of holes in LDA, are also occupied even for small U, resulting in magnetically dead character even before the critical region is reached.

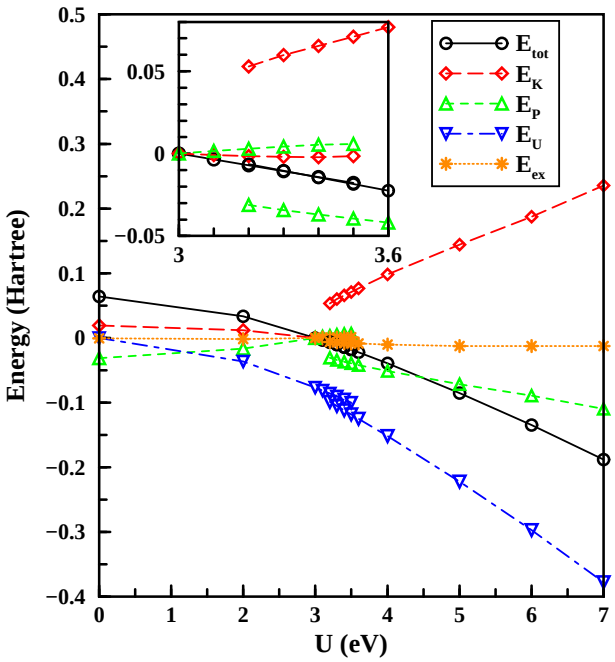

Figure 3.20. Change of energies versus U in FM $Na_{0.5}CoO_2$. The energy is relative to E(U=3 eV), except the LDA+U energy E_U whose actual value is plotted. Inset: Enlarged critical region.

To gain some insight into the cause of disproportionation, the change in energy $E(U)$, with various contributions, is displayed in Fig. 3.20. The total energy is basically continuous at the transition. During CD transition, large discontinuities occur in the (Kohn-Sham all-electron) kinetic energy E_K and (electron + nuclear) potential energy E_P. E_K jumps sharply by 0.74 eV/Co, while the other contributions decrease (in eV/Co): 0.46 for E_P, 0.09 for the LDA exchange-correlation, and 0.18 for the LDA+U correction energy. The LDA+U correction energy is rather small, but is large enough to compensate the balance at U_c.

In this system, Na ions order above MIT.[53] So my Na-ordered cell, leading to

CD at modest U, is realistic. In x=0.5 samples, $Co^{3+}-Co^{4+}$ CD occurs at high temperature (Curie-Weiss susceptibility), but charge/spin become ordered around 50 K (indicated by MIT). Considering my results in which CD occurs above U_c=3.4 eV and the experimentally observed tiny optical gap (∼15 meV)[51, 185, 186], the magnitude of U for x=0.5 phase (allowing FM ordering) should be near its minimum value for CD, i.e, $3.5-4$ eV. However, it must be noted that this U value is varied when allowing AFM ordering (see Sec. 3.6). Within LDA+U, the MIT is orbital selective,[210, 211] but the result is obviously affected by the larger a_g band width than that of the e'_g.

3.5 Is CoO_2 a Mott insulator?

Although in the x=0 end of the Na_xCoO_2 phase diagram Mott insulating behavior has been widely anticipated, there have been few theoretical studies because of limited experimental data, resulting from extreme difficulty to reach the phase. Most of the models in this system[124, 212, 213] assume that the Co on-site Coulomb repulsion U is large enough to produce a Mott insulator, and the existing LDA+U calculations[104, 209] also start from the same viewpoint to model the presumed insulating phase. From this point of view, the e'_g states remain occupied and out of picture, so that Mott physics occurs within the a_g states alone and the system becomes a Mott insulator. However, this scenario has two obstructions: (1) what breaks the balance between the a_g and e'_g orbitals?; and (2) since the existing experimental information states that CoO_2 is a nonmagnetic metal, is a CoO_2 close to a Mott insulating phase or not?

In this section, my study of the strength of correlations in Na_xCoO_2 is extended

to the x=0 phase, using the LDA+U method. Since the appropriate value of U for this system is not well determined,[11] I will vary its value within a realistic range to clarify its effects and require it to be consistent with the available data.

Experimental Information and Crystal Structure

Amatucci, Tarascon, and Klein [214] synthesized first CoO_2 powders, which had been thought to be too unstable to produce, reproducibly by deintercalation of Li from Li_xCoO_2 using a dry plastic battery technology. The group reproduced the CoO_2 material through subsequent research on the $Li_xNi_{1-y}Co_yO_2$ system.[215] The CoO_2 compound is metallic and nonmagnetic.[77] In the CoO_2 compound, the layers of charged "O^{2-}" ions are neighbors. This proximity of negatively charged layers has been thought to be the cause of the instability of CoO_2. The possibility of $O-O$ bonding across the van der Waals gap in CoO_2 has been discussed,[215] and is consistent with the observed metallic character.

All reports [215, 216, 217] of CoO_2 suggest the usual edge-sharing octahedral structure (space group $P\bar{3}m1$, No. 164) of the layers. I used the experimental lattice constants a=2.8048 and c=4.2509 (in units of Å).[215] The O height in the octahedrally coordinated CoO_6 arrangement was not established, being only weakly constrained in the range of $0.17 < z_0 < 0.23$. (Venkatraman and Manthiram measured z_0c=0.257c, but for a nonstoichiometric $CoO_{1.72}$ sample.[217]) Within LDA, I optimized the O height through minimizing energy for both FM and PM cases. I found identical values for both cases, so the value is insensitive to magnetic order. The resulting value of z_0c=0.235c=0.999 Å leads

[11] The size of U seems to be significantly x dependent. I will address the issue carefully in Sec. 3.7.

to a Co−O−Co bond angle of 95 deg and Co−O bond length of 1.90 Å (compare with $z_0c \approx 0.269c$=1.14 Å, 90° and 1.98 Å for perfect octahedra). Compared with the relaxed value (z_0c=0.908 Å, 98°) at $x = 0.5$ by Singh,[82] my value is 9% larger, implying a large effect of the Na^+ ions or the c lattice parameter, or perhaps as important, the added electronic charge. Zhang *et al.*[104] reported 0.1 Å smaller than my optimized z_0, because they used an 50% larger c lattice constant than the experimental value to remove artificial interlayer interaction. The difference suggests that the interlayer interaction (i.e., the effect of c lattice constant) is quite coupled to the O height. There is other data that shows the effect of the added electronic charge: when the c lattice constants are fixed for all x, the relaxed z_0 increases nearly monotonically for $x \geq 0.3$.[104, 218]

Nonmagnetic CoO_2 in LDA

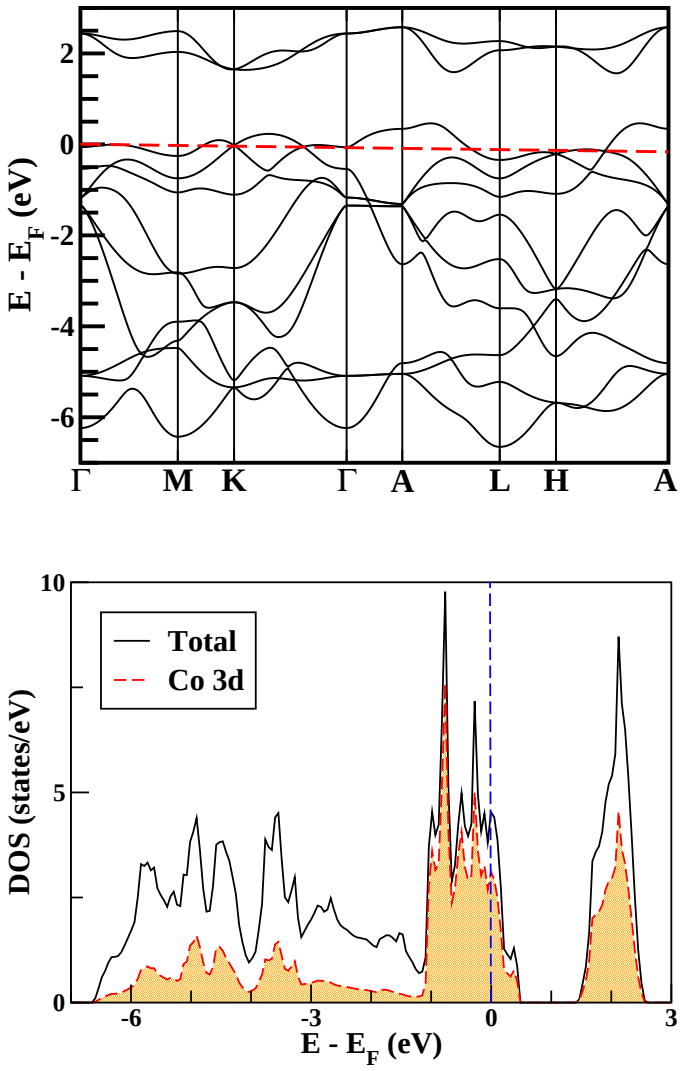

Figure 3.21. LDA nonmagnetic full band structure (top) and corresponding DOS (bottom) of CoO_2. The e_g bands lie above 1.5 eV, and the t_{2g} bands in the range of -1 to 0.5 eV, leading to the $t_{2g} - e_g$ crystal field splitting of 2.5 eV. Note that the t_{2g} manifold at x=0 (i.e., CoO_2) has much stronger hybridization with O $2p$ bands, which are mainly below -1 eV, than for the $x > 0$ case.

This nonmagnetic state is closest to nonmagnetic metallic state, observed by Tarascon and coworkeres.[77, 214, 215] The LDA PM band structure and corresponding DOS of CoO_2 in the region containing Co $3d$ and O $2p$ states are displayed in Fig. 3.21. The result is metallic, containing one hole per Co in the t_{2g} manifold, having a bandwidth of 1.5 eV. The $t_{2g} - e_g$ crystal field splitting is 2.5 eV, identical with the value for $1/3 < x < 2/3$.[73, 74, 76, 82] (The splitting seems to be identical independent of x in the system.) Additionally, although the t_{2g} manifold lies mainly in the range of -1 to 0.5 eV, the t_{2g} bands are strongly hybridized with O $2p$ bands, as addressed carefully in Sec. 3.3.3.

Effect of Co−O bond length in a FM order

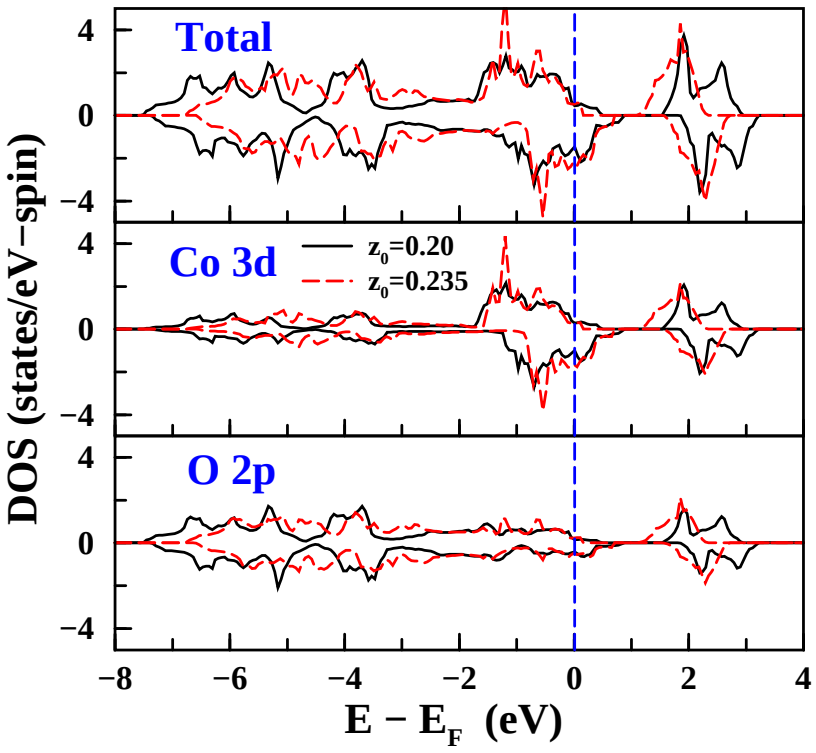

Figure 3.22. Effect of the oxygen height z_0 on the LDA FM DOS at x=0. Increasing the Co−O bond length (by increasing z_0, the $t_{2g} - e_g$ crystal field splitting decreases, but the mixing of Co $3d$ and O $2p$ states remains strong. In contrast to half-metallic behavior in the case of $0 < x < 1$, the system at x=0 is just metallic within LDA though it is nearly half-metallic at the relaxed z_0=0.235. The vertical dashed line denotes the Fermi energy.

Within LDA, a FM state at x=0 has lower energy by 18 meV/Co than a PM state. (This favoring of ferromangetism is generic for Na_xCoO_2 system.) The energy difference is quite small for a system with magnetic moment of 1 μ_B. Considering a simple Stoner instability for comparison, the energy gain is $Im^2/4 \approx 150$ meV, assumed $I \approx 0.7-0.8$ eV. The disagreement with experimentally reported nonmagnetic state will

be discussed below.

I already discussed the effect of the Co−O bond length for the PM state in Sec. 3.3.4, but I could expect additional information for the FM state. Figure 3.22 shows the FM DOS at the relaxed height z_0=0.235, compared with z_0=0.20 (corresponding to Co−O bond length of 0.85 Å).

In addition to narrowing of the t_{2g} bands, increasing the height in this range reveals several trends: narrowing of the unoccupied e_g bands as well as the t_{2g} manifold, leading to a reduction of the crystal field splitting; a shift of the occupied O $2p$ bands toward E_F; electrons transfer at the rate $\Delta Q_d/\Delta z_0 \approx 1$ from O $2p$ to Co $3d$ states. The charge transfers primarily into the a_g majority band, since the e'_g majority manifold is almost fully occupied even at z_0=0.20. As a related effect, the magnetic moment also increases as the O height increases within LDA.

Ferromagnetic tendencies in the correlated limit

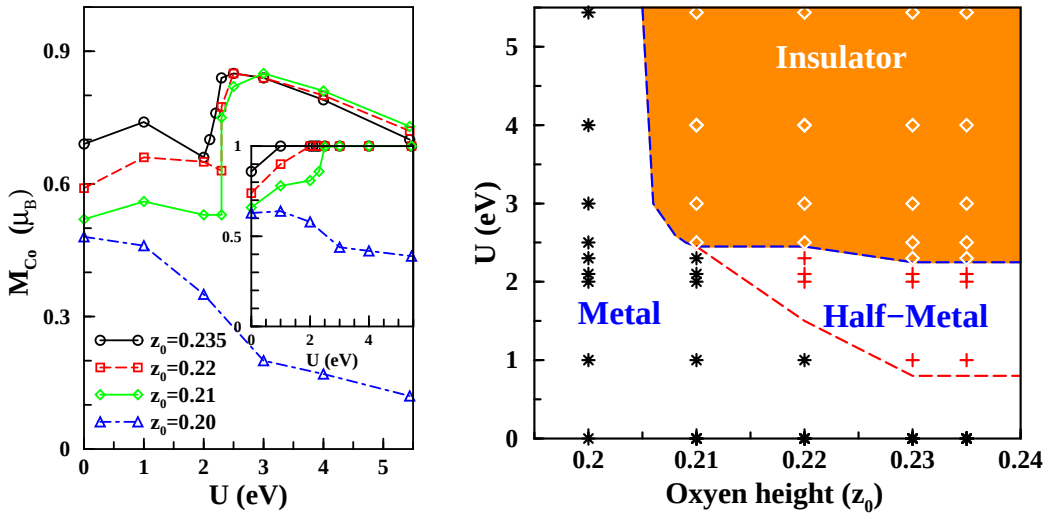

Figure 3.23. Left panel: Effect of the on-site Coulomb repulsion U and the oxygen height z_0 (from the Co layer) on Co magnetic moment in the FM state at x=0. At $z_0 \geq 0.21$, there is a first-order transition at U_c=2.5 eV. At $z_0 \leq 0.20$, the system shows a different behavior, always metallic independent of U. The inset shows the change of the total magnetic moment with respect to U. Right panel: phase diagram depending on the oxygen height z_0 and U in the FM state at x=0. Note that the lattice constant c=4.2509 Å is used. The change in O height between z_0=0.22 and 0.23 is the same variation as measured between x=0.3 and 0.7. The symbols describe metallic (*), half-metallic (+), and insulating (diamond) states.

The change in the magnetic moment with U is shown in the left panel of Fig. 3.23, for the range of $0.20 \leq z_0 \leq 0.235$. At $z_0 \geq 0.21$, the Co magnetic moment jumps sharply at U_c=2−2.5 eV, accompanying the gap opening (metal-insulator transition). The amount of jump tends to decrease as the O height increases. As a result, the z_0=0.235

case shows a slightly smoothed transition, but the slope at U_c remains sufficiently steep. In contrast to the x=1/2 FM case,[73], no hysteresis has been observed at x=0. Because a hysteretic region means that two states are nearly degenerate, no hysteresis indicates that the difference in energy slopes $\mathrm{d}E/\mathrm{d}U$ of the two states is much larger than for the x=1/2 FM case.

In addition to the MIT, for $z_0 \geq 0.21$, there is another feature to be noted. At U=1 eV, a kink results from a transition from metal to half-metal. The inset of the left panel in Fig. 3.23, displaying a change in the total magnetic moment with respect to U, elucidates the transition, because the total magnetic moment must be 1 μ_B for a half-metal or an insulator. The phase transition is illustrated in the right side of Fig. 3.23.

On the other hand, z_0=0.20 case shows no Mott/disproportionation transition even for large U, much different behavior from the $z_0 \geq 0.21$ cases. Applying U, the magnetic moment decreases rapidly, resulting from keeping metallic independent of U. The reason is not entirely clear. However, it may come from the increased hybridization between Co a_g states and O p_z states. Already at $U \rightarrow$0 (LDA), the a_g bandwidth at z_0=0.20 is about 25% larger than at z_0=0.235. The increased hybridization will make the a_g-derived Wannier orbital less localized and eventually less sensitive to correlation effects. While the O height of z_0=0.20 lies outside the accessible range, it does show that there is a regime where correlation effects are very strongly coupled with the Co$-$O bond length, and that the system is not so far from that regime.

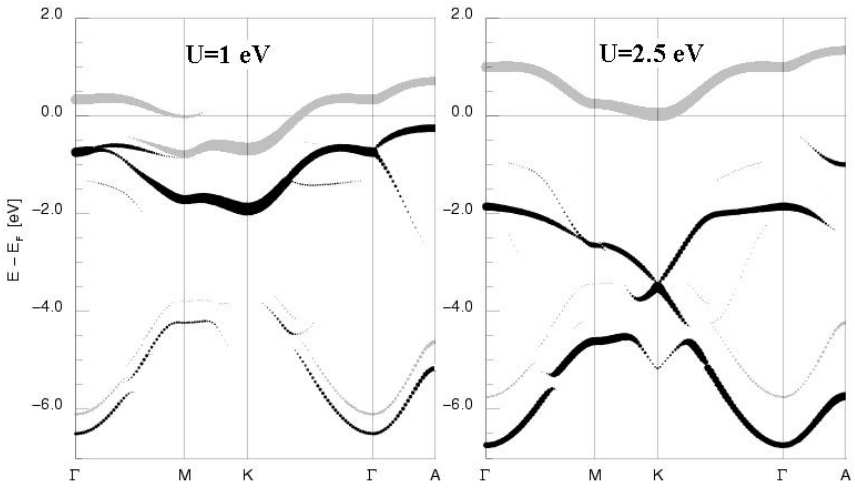

Figure 3.24. Change of the a_g states near the critical value of U in the FM state at the optimized O height z_0=0.235. This large difference elucidates the Mott transition within the a_g band. The gray and black lines indicate the a_g minority and majority band, respectively. The U=1 eV result is indistinguishable from the LDA (U=0) result.

I focus now on the optimized O height case. The transfer of the a_g spectral weight from U=1 eV to U_c=2.5 eV given in Fig. 3.24 reveals the dominating role of the a_g minority band for the MIT. Note that the majority orbitals of the a_g state as well as the e_g' (not shown here) are fully occupied regardless of U. At U_c=2.5 eV, the minority a_g band is completely unoccupied, so becoming the upper Hubbard band. The majority a_g band (lower Hubbard band) lies much deeper, resulting in mixing strongly with the O $2p$ bands. The Mott transition can be visualized by change in the occupancy of the a_g minority orbital (not shown here), decreasing by $0.27e$ at U_c. This Mott transition of the a_g orbital (rather than of the e_g' oribitals) would be favored by the slightly larger band width of the a_g orbital.

Antiferromagnetic tendencies in the correlated limit

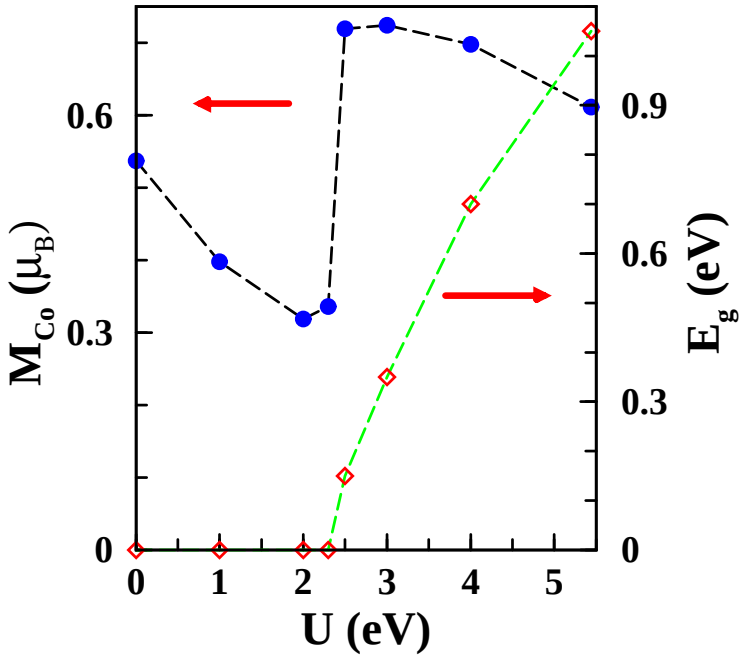

Figure 3.25. Effect of U on the Co magnetic moment in the AFM state of CoO_2 (x=0) at the optimized O height z_0=0.235 . There is a first-order transition at U_c=2.3 eV. The left axis represents a Co magnetic moment, while the right axis shows the energy gap.

Although FM is always favored energetically over AFM, I used a two-Co supercelll with the optimized z_0 to study AFM which can be obtained as a metastable state. The effect of U on the Co magnetic moment is shown in Fig. 3.25, with the change in energy gap. Below U_c, the moment decreases rapidly as U increases, being only 60% of LDA at U=2 eV. It is related with a tendency of Co$\rightarrow$0 charge transfer, as also found in the FM case. As in the FM case, a first-order MIT occurs at U_c=2.5 eV, little lower value than in the FM case. At the transition, the magnetic moment increases more dramatically than for the FM cases, to 0.72 μ_B.

Fixed Spin Moment Study

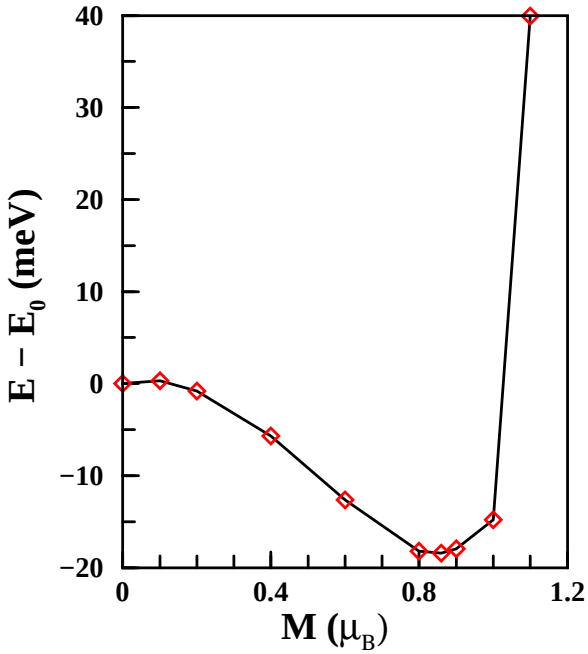

Figure 3.26. LDA fixed spin moment calculation at x=0. In contrast to the cases of $0 < x < 1$, showing a sharp jump at M=1 μ_B due to the large $t_{2g} - e_g$ crystal field gap, it has a minimum at M=0.86 μ_B before the jump. M is the total magnetic moment per formula unit in μ_B.

As already noted, Na_xCoO_2 shows an energetically favored FM state throughout all x within LDA. However, while for $x \geq 0.75$ the CoO_2 layers are FM (and stacked with alternating spin direction), for $x < 0.75$ no FM is observed. This favoring within the local density theory can be changed when correlation effects are considered, i.e., applying U.[74, 108] In the CoO_2 system the FM state is always favored in both LDA and LDA+U calculations, though it is reported to be metallic and nonmagnetic. Fixed spin moment (FSM) calculations help to understand the contradiction to some extent. Figure 3.26

displays the total energy vs. fixed total magnetic moment (on a per formula unit) plot. It is very similar to the FSM result of Singh at x=0.3, 0.5, and 0.7, specially the sharp energy increase at M=1 μ_B due to the large $t_{2g} - e_g$ crystal field splitting.[203] However, the plot at x=0 shows different behavior, a minimum at M=0.86 μ_B (the value from the self-consistent calculation).

I have evaluated the Stoner (exchange interaction) I from these FSM calculation. The method accordingly explains the small contribution from the O sites. The enhanced susceptibility is given by

$$\chi = \frac{\chi_0}{1 - N(0)I} \tag{3.1}$$

where the bare susceptibility is given by $\chi_0 = 2\mu_B^2 N(0)$ and $N(0)$ is the single-spin density of states at the Fermi level. At small M, the energy difference is given by $(1/2)\chi^{-1}M^2$. Since $N(0)$ for FM is 1.36 states/eV-spin, we obtain I =0.89 eV, $[IN(0) = 1.2]$. This value of I is comparable with the value obtained from the exchange splitting.

Although there are now several metals where enhanced paramagnets are predicted by local or semilocal density theory to be FM, it is somewhat peculiar for this state to extend to x=0 and a moment of nearly 1 μ_B. It might be that the Moriya theory for the correction of the susceptibility of weak ferromagnets [219] or perhaps dynamical effects such as are contained within dynamical mean field theory [183] will be necessary to correct the prediction. These questions give important directions for further work.

3.6 Insulating AFM $Na_{0.5}CoO_2$

Rather unexpectedly for a hole-doped band insulator, the system shows correlated behavior for $x > 0.5$, while it displays uncorrelated behavior for $x < 0.5$.[76, 93] The correlation strength can be measured by an enhanced linear specific coefficient and Curie-Weiss susceptibility for $x > 0.5$. Whereas both of the regimes are metallic, as said already, precisely at x=0.5 the system becomes insulating[53] with a tiny gap ($\sim$15 meV) through Na ion ordering, charge ordering, and magnetic ordering transitions.

The LDA results by Singh at x=0.5 [82] predict FM to be much more stable than a simple AFM arrangement, consistent with my LDA results. He also showed that accurately treating the Na ions rather than using the virtual crystal approximation does not change the conclusion. So I employ the LDA+U method to find that CD and AFM ordering is favored energetically, with the disproportionation resulting in relieving the frustration on the triangular lattice. It must be noted that correlation effects must be strong enough to drive CD but small enough to leave a tiny gap. In this section, I will address the energetics, behavior of the magnetic moments, and characteristics of the electronic structure in the insulating phase for two recently observed superlattices shown in Fig. 3.27.

Structure

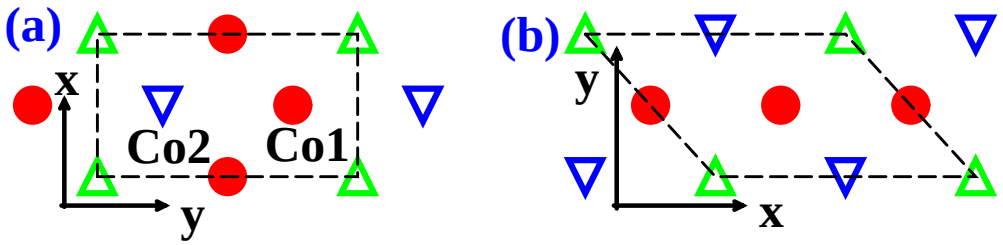

Figure 3.27. Charge and spin ordering of (a) zigzag (ZZ) and (b) stripe patterns in the Co layer of AFM $Na_{0.5}CoO_2$. In the stripe pattern, the Co1 ion lies at a site of inplane inversion symmetry and is neighbored symmetrically by up and down spins. The triangle and solid circle indicate magnetic (Co2) and nonmagnetic (Co1) cobalts, respectively. In the calculations, Na lies above Co1, which become the nonmagnetic Co^{3+} sites. (I used the same conditions as my previous calculations,[73, 76] but with attention to Brillouin zone sampling up to 312 irreducible **k** points.)

In the triangular lattice with one spin per site, the nonbipartite nature frustrates AFM ordering, and several nearly degenerate charge order patterns are suggested.[104, 106, 220] However, x=0.5 with CD correponds to one spin for every two sites allowing for patterns that relieve the frustration. In this calculation, I used two experimentally suggested patterns, the zigzag and stripe patterns as displayed in Fig. 3.27. Cava and coworkers [109, 188, 190] have presented electron diffraction data, indicating robust Na ion zigzag (ZZ) ordering in an orthorhombic four-Co supercell as shown in Fig. 3.27 (a). The Na ordering survives above room temperature. The Na ZZ ordering, including the two distinct types of Na sites, was confirmed by Yang *et al.*[189] Zhang *et al.* calculated the Coulomb interaction energy between the Na^+ ions and concluded that the ZZ ordering

is favored.[104] Note that the Na ion ZZ phase is not the same as the Co ZZ order. The Na ZZ order contains one site on top of Co and another site not on top of any Co, so it is "less zigzag" than this Co ZZ order.

Although the insulating behavior begins at T_{c2}=52 K, the interpretation of the onset was suspected to be charge ordering. So, it invited neutron diffraction studies. The two recent studies[71, 72] have confirmed two types of Co ions, ons consistent with spin-half but with reduced moment ($0.25 - 0.34\mu_B$) and another with much smaller moment, and AFM ordering at T_{c1}=88 K of stripe pattern as shown in (b) of Fig. 3.27. The observed structure shows also antiparallel spin ordering along c direction. But, in this calculation, I used the simplified single layer, i.e, parallel spin ordering along the direction.

The symmetrical difference in the Co1 ions is clear. In the ST pattern of Fig. 3.27(a), the Co1 ions are surrounded symmetrically (by in-plane inversion) by two spin-up Co2, spin-down Co2, and two nonmagnetic Co1. Although the ions in the ZZ pattern of Fig. 3.27(b) are surrounded by the same six-nearest neighbor ions, there is no inversion symmetry. So, the ST pattern has the higher symmetry of the Co1 ions than in the ZZ pattern.

Energetics

As for all other values of x,[82] FM is favored energetically over AFM for both ZZ and ST patterns. But the energy difference between FM and AFM is substantially large for ZZ, while surprisingly small for ST. This favoring of FM by LDA requests to include correlation effects in the system, so I utilize the LDA+U method. Although an appropriate value of U is essential, especially for CD, gap opening, and favored AFM

ordering, almost independent of U the ZZ pattern is favored over the ST pattern by the very small amount of 22 meV/Co. Considered that I use simplified model for the patterns, however, I can conclude that these two patterns are nearly degenerate in view of energy.

Effect of U on the Co magnetic moment

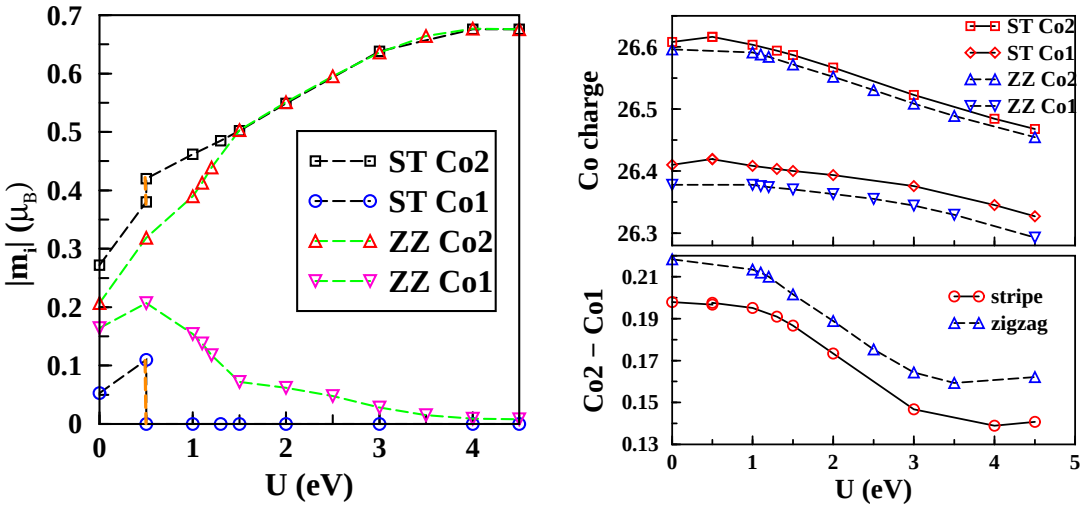

Figure 3.28. Left panel: Effect of U on magnitude of the Co local magnetic moments m_i in the stripe and zigzag patterns of AFM $Na_{0.5}CoO_2$. At U_{c2}=1.5 eV, gap opening occurs, whereas CD (Co1→Co^{3+} and Co2→Co^{4+}) starts already at U_{c1}=0.5 eV. Note that Hund's rule J=1 eV has been kept fixed. Right panel: Change in Co $3d$ charges by U in the both patterns. The bottom panel shows that the charge difference between two Co sites is only ∼0.2 e. As seen in the top panel, this difference is ∼0.02 e smaller for ST than for ZZ. It is based on the Mullikan charge decomposition in the FPLO method.

I first review behavior vs. the on-site Coulomb repulsion U. The left panel of Fig. 3.28 shows the change in magnitude of the Co1 and Co2 magnetic moment for both patterns, varying U. Even for LDA (U→0 limit), the effects of the symmetry determined

by the position of Na ions are obvious. For ZZ, the Co1 and Co2 magnetic moments are almost identical. But, for ST, the Co1 moment is already very tiny, only half of μ_B, while the Co2 moment is 0.27 μ_B. The difference reflects the higher symmetry of the Co1 ions in the ST patterns. Increasing U, the Co2 magnetic moments increase monotonically and become identical at U_{c2}=1.5 eV, where the band gap opens for the both patterns. The Co1 moments show more different behavior in both patterns. For ZZ, above U_{c1}=0.5 eV, the Co1 moment decreases almost linearly, but undergoes one more discontinuity at U_{c2}. Whereas the Co1 moment for ZZ never becomes zero due to no in-plane inversion symmetry at the Co1 sites, the moment for ST becomes immediately zero at U_{c1}=0.5 eV, where might be identified as the CD transition. While the Co1 and Co2 ions are clearly disproportionated, the charge difference is only $\sim$0.2 e as shown in the right panel of Fig. 3.28.

It is worthwhile to note that CD had occurred already at smaller U=U_{c1} than the critical value U_{c2} for the gap opening. Recalling that CD and gap opening occurs simultaneously when the smaller supercell or different Na concentration is used,[73, 76] we find here a richer behavior. This difference of the critical values between the CD and the gap opening was also obtained for a similar supercell by Li *et al.*, but a little higher critical value.[108]

Electronic structure at U=2 eV

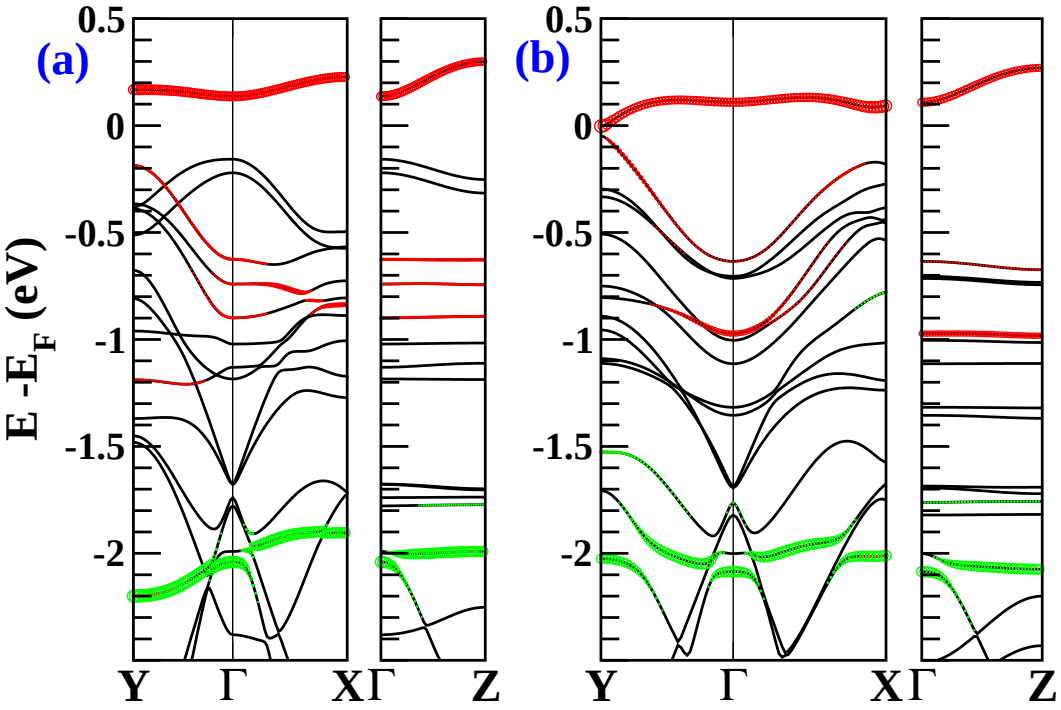

Figure 3.29. Blowup of the AFM band structures in the t_{2g} manifold at U=2 eV for (left) the zigzag (ZZ) and (right) the stripe (ST) patterns. For ZZ, the minimum gap occurs at a corner of the zone that is not shown. The plot is along perpendicular (Γ-Y) and parallel (Γ-X) directions for the each chain. Z indicates the zone boundary point along the $\langle 001 \rangle$ direction. The thickened lines highlight the band having strong a_g character for each spin of a magnetic Co2.

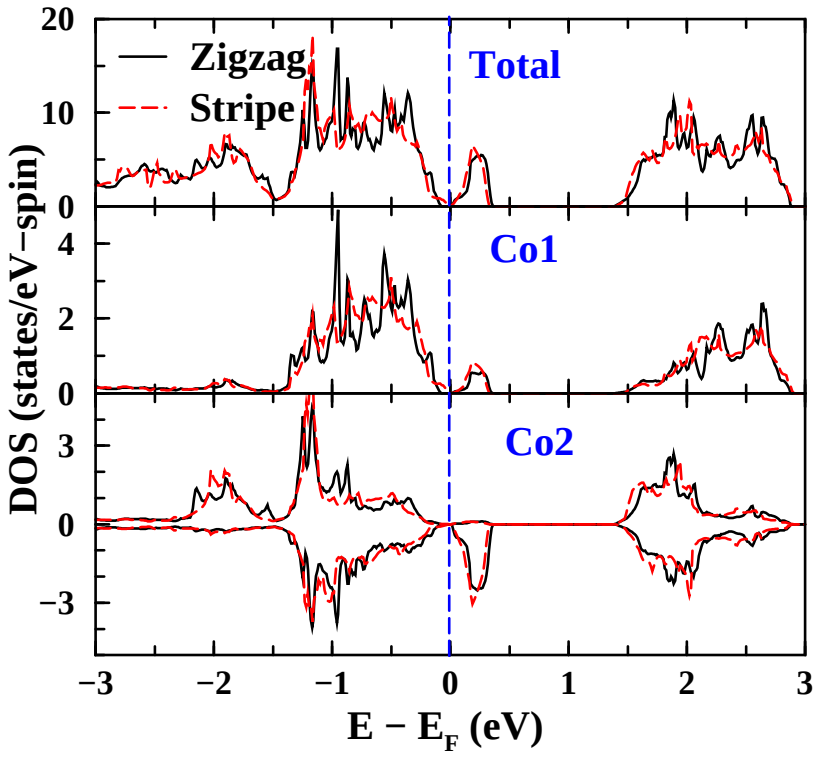

Figure 3.30. Total and atom-projected DOS for both patterns at U=2 eV. Although the band structures are different in dispersion through the zone, the DOSs are extremely similar for the both patterns. For the total and (nonmagnetic) Co1 only the majority spin channel is shown, whereas the (magnetic) Co2 DOS is displayed for both channels. The dashed vertical line denotes E_F (set to zero).

Since the results depend on U, as emphasized previously, the appropriate value of U is necessary. In this system (at x=0.5), it is rather straightforward to determine the required value. The system should have CD, AFM ordering, and a tiny gap. So the appropriate value should lie slightly above U_{c2}, i.e, U=1.5−2 eV.

I will address the results at U=2 eV, a value chosen slightly higher than U_{c2} to make the gaps more clearly visible. The critical interaction strength accompanies a Mott-

like transition in the Co2 a_g states, with upper and lower Hubbard bands separated by 2.2 eV which can be seen in the the band structure of Fig. 3.29. The band structures are described along directions parallel ($\hat{x}$) and perpendicular ($\hat{y}$) to the ZZ or ST chains of Co ions at U=2 eV. The upper Hubbard band, unoccupied Co2 a_g, is nearly flat, but shows some 3-dimensionality; there is more dispersion perpendicular to the layers (200 meV) than within the layers. The most different behavior between the ZZ and ST patterns is in dispersions going away from the zone center (Γ point) of the uppermost two valence bands having primarily Co2 e_g' character. The dispersions are positive for ST and negative for ZZ. Nevertheless, the corresponding DOS, pictured in Fig. 3.30, are extremely similar for both patterns.

From now on, I focus on the observed ST pattern. As displayed in Fig. 3.29 (b), the unoccupied Co2 minority a_g state is above the gap and primarily Co1 e_g' states lie below the gap. This is an unusual $d-d$ charge transfer gap (not the usual $p-d$ case). Since the crystal field ($t_{2g} \rightarrow e_g$) gap is $\sim$2 eV, the optical transitions in the IR for the magnetically disordered metallic phase (T>T_{c1}) reflect $e_g' \rightarrow a_g$ excitations, *i.e.* transitions within the t_{2g} complex. Below the metal-insulator transition at T_{c2}, the excitations across the gap are to the upper Hubbard band, and the main weight of these transitions – the new (Co1 $\leftrightarrow$ Co2) charge-transfer type – is shifted up in energy by only a few tens of meV.[51, 185, 186] This small shift is consistent with the small bandwidth that we find for the unoccupied Co2 a_g band (upper Hubbard band).

Moreover, in the ST pattern, the upper Hubbard band shows stronger dispersion along the Y-Γ line than along the X-Γ line. The stronger dispersion can be understood as follows. Electrons excited into the upper Hubbard reside in the minority a_g states on

Co2, for example, a spin ↑ electron will hop between Co2 ions with moments oriented ↓. Propagating in the $\hat{y}$ direction, it can hop through a single Co1 ion; in the $\hat{x}$ direction, however, it must avoid the U cost of hopping onto an oppositely aligned Co2 ion, thus requiring hops through *two* Co1 ions before returning to another Co2 ↓ ion, and its dispersion is reduced accordingly. Valence band holes introduced into the system will occupy nonmagnetic Co1 e_g' states, while electrons will occupy minority a_g states on Co2.

Temperature evolution: possible SDW?

My results suggest a specific picture of the temperature progression at x=0.5. Considering that the FM ordered layers for $x \geq 0.75$ are consistent with itinerant character and the $0.5 < x < 0.75$ regime with fluctuation-suppressed magnetism, the magnetic ordering below T_{c1} may be more of a spin density wave (SDW) character which gaps some but not all of the Fermi surface; recall that for the ST pattern the FM-AFM energy difference is tiny at small U, and that even at U=0 there is a substantial difference in moments on Co1 and Co2, that is an SDW. Several band structure studies have designated nesting features in the paramagnetic Fermi surface.[76, 82, 170] The challenge that this picture must face is that the primary magnetic order is unchanged at the insulating transition T_{c2}: Gašparovic *et al.* find that the principal ordered moment grows with decreasing temperature[72] continuously through the insulating transition at T_{c2}. The additional order that results in a kink in χ_c at T_{c2} has not yet been clarified, but my results are consistent with the dominant picture that CD arises finally at T_{c2}. The redistribution of spectral weight below T_{c2} observed in optical experiments shows differences (weight shifted to 20-30 meV[186] or 70-100 meV[51]), but they seem consistent with the correlated band

Table 3.2. Analogy and distinctions between the strip pattern and cuprates (see text, for details). Note that the first 2 lines (analogy) apply to both systems.

	ST	Cuprate
Analogy	· AFM	
	· bipartite lattice, with axes at 90 deg	
Energy gap	15 meV	2 eV
U	1.5−2 eV	6−8 eV
metal-metal nn hopping	10−20 meV	30−50 meV
Low energy excitation	three d bands	single $d_{x^2-y^2}$

structure of Fig. 3.29 and particularly the narrowness of the unoccupied band.

It can reasonably be asked whether the ground state of this system should be considered as a correlated insulator, as outlined above, or instead as perhaps a SDW (at T_{c1}) – CDW (at T_{c2}) system. Balicas *et al.* have found that, when an applied in-plane field increases beyond 25 T the conductivity increases by a factor of two (a sort of insulator-metal transition), and observation of magnetoresistance oscillations suggests the restoration of part of the Fermi surface.[187] Certainly the insulating phase is delicate. However, the observation of a substantial ordered moment on Co1 (0.25-0.34 μ_B)[71, 72] and little or none on Co2 speaks for a CD picture (into identifiable Co^{4+} and Co^{3+} moments) and hence a correlated insulator below T_{c2}.

Comparison of the stripe pattern with cuprates

Finally, I will address an interesting similarity of the AFM configuration of the ST pattern, illustrated in Fig. 3.27 (b), with the AFM cuprate layer. The ST AFM ordering has the bipartite (and 90°) topology of spins, characteristic of the cuprate plane. However, in contrast with the cuprate layer, the ST ordering shows anisotropy of (Co^{4+}-Co^{4+}) parallel and perpendicular hopping amplitudes t_x, t_y and exchange couplings J_x, J_y. Note that J_x is between near neighbors, while J_y is between second Co neighbors.

In spite of this similarity, there are obvious differences. Cuprates are robust Mott insulators represented by the 2 eV gap, and the value of U required to explain the insulating character is $3-4$ times larger. Besides, the effective metal-metal near neighbor hopping is $2-3$ times greater. In the cobaltate, the tiny gap indicates a marginally insulating correlated state, and the low energy excitations require three t_{2g} bands instead of the dominance of the single $d_{x^2-y^2}$ state in the cuprates. It also seems that magnetic coupling cannot be treated in the usual Heisenbeg form, because the superexchange mechanism is not dominant and the somewhat flimsy moments depend strongly on the type of magnetic order. (A spin Hamiltonian might be reasonable to treat spin waves within a given ordered state.)

3.7 Correlation Strength $U(x)$ Dependent on Na Concentration

Enhancement in Linear Specific Coefficient

For $x > 0.5$, local moments are obvious in thermodynamic and transport data, and spin fluctuations have been observed in neutron scattering studies. In particular, the linear specific coefficients are large, γ=48−56 mJ/mol K^2,[60] or more recent data $\sim$ 34 mJ/mol K^2 [61]. Compared with my calculated value γ_0=10±2 mJ/mol K^2, dynamic correlation effects lead to at least three times enhancement. My finding of CD for $U > 3$ eV is consistent with the experimental information indicating a correlated behavior: for example, a large field-dependent thermopower [30, 38] and a large Kadowaki-Woods ratio [155].

In the superconducting regime x≈0.3, similarities with cuprates seemed to say that correlation effects might play an essential role in the superconductivity. However, the existing data seem to suggest otherwise. The specific heat coefficient is customary, with the reported values around γ=12 − 13 mJ/mol K^2.[41, 42, 61] The value is nearly identical with my calculated value γ_0=13 mJ/mol K^2. It is consistent with the fact that evidence of correlation effects is lacking for $x < 0.5$: Pauli susceptibility (no local moment) and small magnetic field dependence of the resistivity. In addition, as discussed in Sec. 3.5, the x=0 phase is not a Mott insulator, but rather a nonmagnetic metal. This comparison with the experiments suggests that $U(x)$ is significantly dependent on the carrier concentration x, i.e., Na concentration.

Change in the critical on-site Coulomb repulsion for charge disproportionation

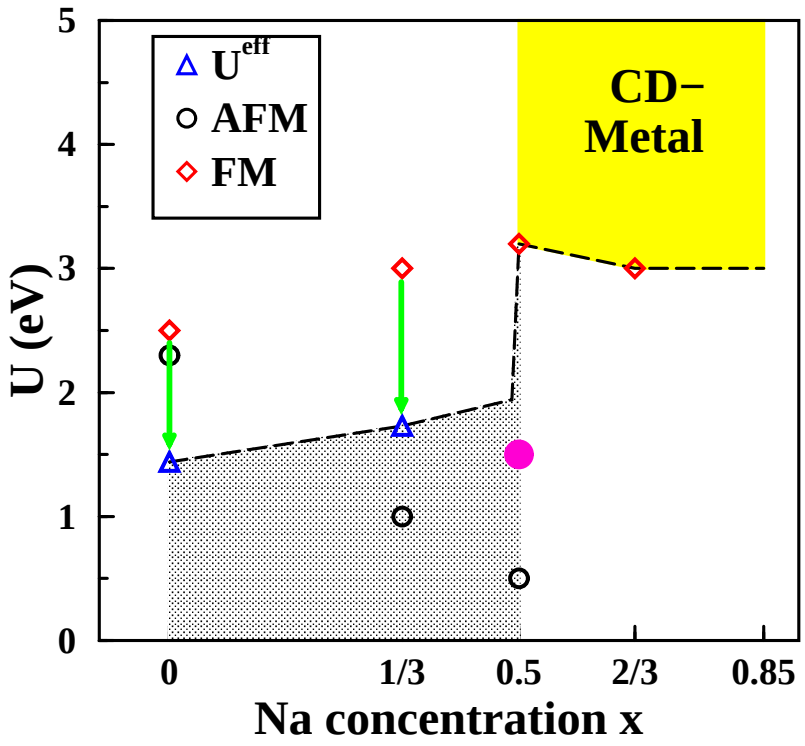

Figure 3.31. Effect of Na concentration x on the critical on-site Coulomb repulsion U_c for CD. The CD accompanies gap opening, except for the AFM order at x=0.5. ($U \rightarrow U^{eff} = U/\sqrt{3}$) Considering FM ordering, comparison with the experiments indicates a change of U with sharp jump at x=0.5, depicted by the shaded region. The arrows represent decrease of the effective on-site Coulomb repulsion U^{eff} due to three-band nature for $x < 0.5$. In this case, CD occurs at U=0.5 eV (open circle), while the gap opens at U=1.5 eV (filled circle).

Since there is no agreement on the best value of U in the system, it is essential to harmonize my finding values with observations. Change in $U(x)$ required by my studies is depicted in Fig. 3.31. At first, focusing on FM ordering, U_c for CD increases linearly below

x=0.5 and is almost flat above x=0.5. For the end member x=0, Tarascon and coworkers have been observed nonmagnetic and metallic behavior,[77] suggesting $U(x = 0)$ should be less than U_c=2.5 eV for a Mott-like transition. Below x=0.5, no observation[12] for CD (Pauli-like susceptibility) nor any significant correlation effects indicates $U(x < 0.5) < U_c$=3 eV. Since only a tiny gap (∼15 meV) has been observed at x=0.5,[51, 185, 186] $U(x = 0.5)$ should be near the minimum value for the CD (3.5 − 4 eV). As said in the previous subsection, for $x > 0.5$ the Curie-Weiss susceptibility as well as other evidence of strong correlation effects have been observed. The observed susceptibility indicates $(1 - x)\mathrm{Co}^{4+}$ and $x\mathrm{Co}^{3+}$ ions, resulting in CD even though it is a good metal. It leads to $U(x > 0.5) < U_c$=3 eV, perhaps over 4 eV.

On the other hand, there are several indications that the simple single band picture is oversimplified. In particular, the a_g band center is nearly degenerate with the e_g' states, with slightly smaller bandwidth of the e_g' bands. Due to the form of dispersion (a little wider bandwidth of the a_g band) in the CoO_2 layers, holes doped into the band (not Mott) insulator $NaCoO_2$ initially go into the a_g band. Thus, it is reasonable to use a single band model for the small $1-x$ regime with a rather strong value of U. But, for $x < 0.5$, the LDA band structure is quite consistent with observations, suggesting the system crosses over into a three-band regime where the full t_{2g} manifold plays a role. The multiband nature tends to diminish correlated behavior. Carriers doped into a multiband system may simply find a smaller phase space for reaching the Mott-Hubbard insulating phase, as the carriers have more degrees of freedom. According to extensive study of Gunnarsson

[12]There are two exceptions. One is the temperature-dependent shift of spectral weight that has been interpreted in terms of (real or incipient) orderings at x=1/4.[185] Another is measurements of resistivity and magnetization for $0.4 < x < 0.5$ that show similar kinks as the x=0.5 phase below 100 K, and suggest an emerging charge ordering transition.[221]

and coworkers,[222, 223, 224] in a multiband system of N bands the effective Coulomb repulsion becomes U^{eff}=$U/\sqrt{N}$. In the system having carriers in the t_{2g} manifold (N=3), U_c=3 eV at x=1/3 would become U_c^{eff}→3 eV/$\sqrt{3}$∼W, so correlation effects reduce greatly. Such a strong decrease in the effective repulsion could readily account for the observed severe decrease in correlation effects. Moreover, more carriers will lead to more screening, resulting in decreasing correlation effects.

Finally, allowing AFM ordering (realistic case for x=0.5), the critical value U_c is 2 eV less than for FM ordering, except for the x=0 case having nearly identical value for the both orders. (My choice of small supercell has only one Co^{4+} ion at x=2/3, so it allows only a trivial simple AFM arrangement, which is not observed.) As said previous, the easy CD (and gap opening) stems from narrower band width of the unoccupied a_g band in the AFM ordering. It must be noted that for the AFM order at x=0.5 the critical value for CD is different from the gap opening, as emphasized in Sec. 3.6. It remains for further research to decide how realistic LDA+U should be for the band gap, or whether dynamics of the correlations are important.

3.8 Summary

The strength and effect of Coulomb correlations of Na_xCoO_2 for all ranges of x are evaluated using the correlated band theory LDA+U method. I show that moderate values of U lead to CD for 0≤ x <1. For the x=0 system there is a critical value U_c≈2.3 eV for both FM and AFM orderings. For $x > 0$ the critical value strongly depends on the magnetic ordering. When allowing FM order, CD occurs at U_c≈3 eV, while when allowing

AFM order U_c drops to about 1 eV. Additionally, comparison with observations suggests that the correlation strength strongly depend on carrier concentration x. A crossover from a three-band regime to a single-band regime decreases more dramatically the correlation effect below x=0.5.

I remind that recent evidence suggests the oxidation state of Co for the superconducting materials is representative of an effective doping level x_{eff} = 0.50–0.60. If true, this puts superconductivity in a more interesting part of the phase diagram, where superconductivity would arise from electron doping of the x=0.5 disproportionated, charge-ordered, and spin-ordered magnetic insulator.

In particular, for x=0.5 (unique insulating phase in the system), my calculations reveals the mechanism of CD: a first-order transition of $2Co^{3.5+} \rightarrow Co^{3+} + Co^{4+}$. This orbital selective CD of the Co a_g orbital, due to slightly wider band width than that of the Co e'_g, leads to half of the ions (Co^{3+}) becoming electronically and magnetically dead, and subsequently undergoing the observed charge ordering or metal-insulator transition. In contrast to the simultaneous CD and gap opening when smaller cells or different Na concentration are used, the CD occurs already at smaller U than the gap opening using the two AFM ordering patterns recently reported at x=0.5. One of the patterns, "out-of-phase stripe", shows interesting analogies, but substantial distinctions with cuprates.

Finally, there are two points that must be noted. First, the transitions with varying U discussed here should be of special interest for high pressure research: applying pressure changes the U/W ratio and could drive the x=0.5 unsulator back to metallic. Second, my results imply careful exercises to be required to determine an appropriate U, because the CD occurs in regimes where the precise value of U is crucial.

Acknowledgment

I acknowledge important collaboration with J. Kuneš in the earlier stages of this work and have had helpful communications with H. Alloul, V. I. Anisimov, C. Bernhard, R. J. Cava, A. Eguiluz, O. Gunnarsson, J. D. Jorgensen, M. D. Johannes, D. Khomskii, D. Mandrus, P. Novak, B. C. Sales, R. T. Scalettar, D. J. Singh, R. R. P. Singh, K. Takada, and J. M. Tarascon. This work was supported by DOE Grant DE-FG03-01ER45876 and DOE's Computational Materials Science Network.

Chapter 4

$LaNiO_2$ [1]

4.1 Introduction

The perovskite oxide $LaNiO_3$, purportedly an example of a correlated metallic Ni^{3+} system, has been investigated over some decades by a few groups[225, 226, 227] for possible exotic behavior. The oxygen-poor lanthanum nickelate $LaNiO_x$ has also attracted attention, because of characteristic changes of its electronic and magnetic properties as the oxygens are removed. It is metallic at $2.75 < x < 3$, but semiconducting for $2.50 < x < 2.65$.[228] For $x = 2.6$, it shows ferromagnetic ordering with 1.7 μ_B/Ni below 230 K [228] and magnetic behavior of the $x = 2.7$ material has been interpreted in terms of a model of ferromagnetic clusters.[229] At $x = 2.5$, where formally the Ni is divalent, a perovskite-type compound $La_2Ni_2O_5$ forms in which NiO_6 octahedra lie along c axis directed chains and NiO_4 square-planar units alternate in the $a-b$ plane. This compound shows antiferromagnetic ordering of the NiO_6 units along the c axis but no magnetic

[1] This chapter has been published previously as a paper: "Infinite-layer $LaNiO_2$: Ni^{1+} is not Cu^{2+}", K.-W. Lee and W. E. Pickett, Phys. Rev. B **70**, 165109 (2004).

ordering of the NiO_4 units.[230]

Since $LaNiO_2$ with formally monovalent Ni ions was synthesized by Crespin *et al.*[231, 232] it has attracted interest[233, 234, 235] because it is isostructural to $CaCuO_2$,[236] the parent "infinite layer" material of high T_c superconductors, and like $CaCuO_2$ has a formal d^9 ion amongst closed ionic shells. However, it is difficult to synthesize and was not revisited experimentally until recently by Hayward *et al.* who produced it as the major phase by oxygen deintercalation from $LaNiO_3$.[237] Their materials consist of two phases, the majority being the infinite-layer (NiO_2-La-NiO_2) structure and the minority being a disordered derivative phase. Magnetization and neutron powder diffraction reveal no long-range magnetic order in their materials. Its paramagnetic susceptibility has been fit by a Curie-Weiss form in the $150 < T/K < 300$ range with $S=\frac{1}{2}$ and Weiss constant $\theta = -257$ K, but its low T behavior varies strongly from this form. More recently, this same group has produced the isostructural and isovalent nickelate $NdNiO_2$.[238]

One of the most striking features of $LaNiO_2$ is that it potentially provides a structurally simple example of a *monovalent open shell transition metal d^9 ion.* Except for the divalent Cu^{2+} ion, the d^9 configuration is practically nonexistent in ionic solids. In particular, the formal similarity of Ni^{1+} and Cu^{2+} suggests that Ni^{1+} compounds might provide a "platform" for additional high temperature superconductors. It is these and related questions that we address here.

In this paper we present results of theoretical studies of the electronic and magnetic structures of $LaNiO_2$, and compare with the case of $CaCuO_2$ (or isovalent $Ca_{1-x}Sr_xCuO_2$) which is well characterized. A central question in transition metal oxides is the role of correlation effects, which are certainly not known *a priori* in $LaNiO_2$ as

there is little characterization of the existing material. We look at results both from the local density approximation (LDA) and its magnetic generalization, and then apply also the LDA+U correlated electron band theory that accounts in a self-consistent mean-field way for Hubbard-like intraatomic repulsion characterized by the Coulomb repulsion U. Our results reveal very different behavior between $LaNiO_2$ and $CaCuO_2$, in spite of the structural and formal d^9 charge similarities. The differences can be traced to (1) the difference in $3d$ site energy between Ni and Cu relative to that of Cu, (2) the ionic charge difference between Ca^{2+} and La^{3+} and associated Madelung potential shifts, and (3) the participation of cation $5d$ states in $LaNiO_2$.

We also discuss briefly our discovery of anomalous behavior in the transition metal $3d^9$ ion as described by LDA+U at large U. Although well beyond the physical range of U for $LaNiO_2$, we find that LDA+U produces what might be characterized as a d^8 "singlet" ion in which the internal configuration is one $d(x^2-y^2)$ hole with spin up and one $d(3z^2-r^2)$ hole with spin down, corresponding to an extreme spin-density anisotropy on the transition metal ion but (nearly) vanishing net moment.

4.2 Structure and Calculation

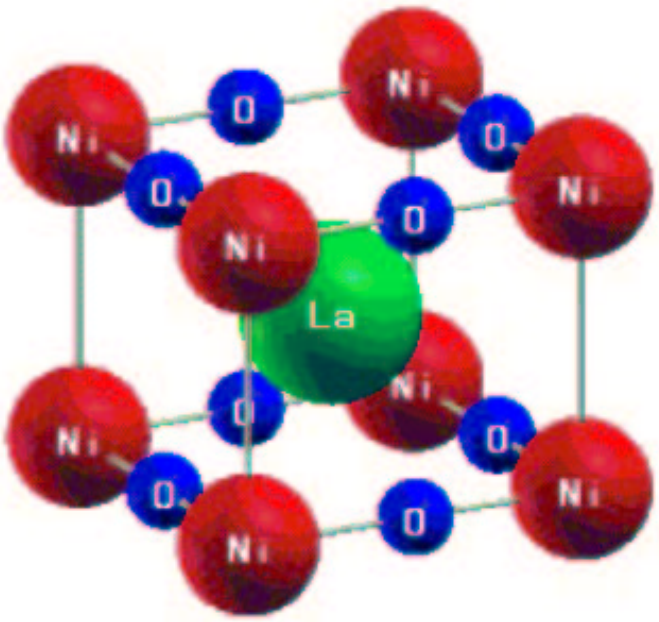

Figure 4.1. Crystal structure of $LaNiO_2$, isostructural to $CaCuO_2$. Ni ions are in the origin and La ions in the center of the unit cell. It has no axial oxygens.

In the samples of $LaNiO_2$ synthesized and reported by Hayward *et al.*, there exist two phases with space group $P4/mmm$ (No. 123) but different site symmetry.[237] We focus on the majority infinite-layer phase, which is isostructural with $CaCuO_2$.[236] In the crystal structure shown in Fig. 4.1, Ni ions are at the corners of the square and La ions lie at the center of unit cell. The bond length of Ni-O is 1.979 Å, about 2% more than that of Cu-O in $CaCuO_2$ (1.93 Å). We used the lattice constants a=3.87093 Å, c=3.3745 Å,[237] with a $(\sqrt{2} \times \sqrt{2})$ supercell space group $I4/mmm$ (No. 139) for AFM calculations.

The calculations were carried out with the full-potential nonorthogonal local-orbital (FPLO) method[6] and a regular mesh containing 196 **k** points in the irreducible

wedge of the Brillouin zone. Valence orbitals for the basis set were La $3s3p3d4s4p4d5s5p6s$ $6p5d4f$, Ni $3s3p4s4p3d$, O $2s2p3s3p3d$. As frequently done when studying transition metal oxides, we have tried both of the popular forms of functional[18, 19] of LDA+U method[12] with a wide range of on-site Coulomb interaction U from 1 to 8 eV, but the intra-atomic exchange integral J=1 eV was left unchanged. For $CaCuO_2$, we used the same conditions as the previous calculation done by Eschrig *et al.* using FPLO.[15]

4.3 Uncorrelated Regime

Electronic structure for nonmagnetic state

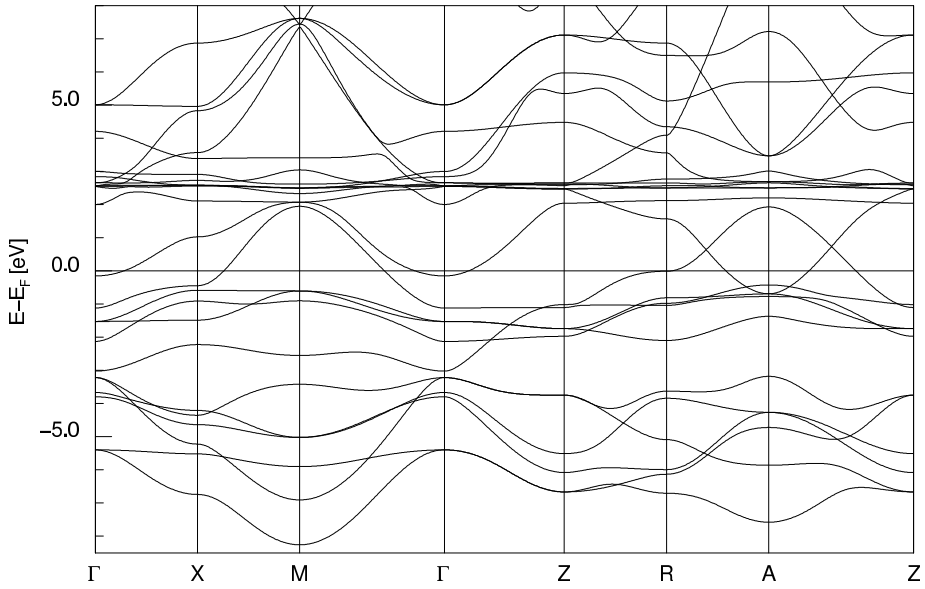

Figure 4.2. LDA paramagnetic band structure of $LaNiO_2$. The Ni $3d(x^2-y^2)$ band crosses the Fermi level (zero energy) very much as occurs in cuprates (see Fig. 3). The La $4f$ bands lie on $2.5-3.0$ eV. The La $5d(3z^2-r^2)$ band drops below E_F at Γ and A. The symmetry points are given in Fig. 4.4.

We present first the LDA results. The paramagnetic (PM) band structure with its energy scale relative to Fermi energy E_F is given in Fig. 4.2. A complex of La $4f$ bands is located at +2.5 eV with bandwidth less than 1 eV. The O $2p$ bands extend from about -8 to -3.2 eV. The Ni $3d$ bands are distributed from -3 to 2 eV, with the localized t_{2g} complex near -1.5 eV, while the broad La $5d$ states range from -0.2 to 8 eV. Unlike in PM $CaCuO_2$, there are two bands crossing E_F. One is like the canonical $d(x^2-y^2)$ derived band in the cuprates, rather broad due to the strong $dp\sigma$ antibonding interaction with oxygen p_x, p_y states and enclosing holes centered at the M point. The other band, lying at -0.2 eV at Γ and also having its maximum at the M=$(\frac{\pi}{a}, \frac{\pi}{a}, 0)$ point, is a mixture of La $5d(3z^2-r^2)$ states and some Ni $3d(3z^2-r^2)$ character. Already this band indicates importance of Ni $3d$ - La $5d$ band mixing.

Tight binding model

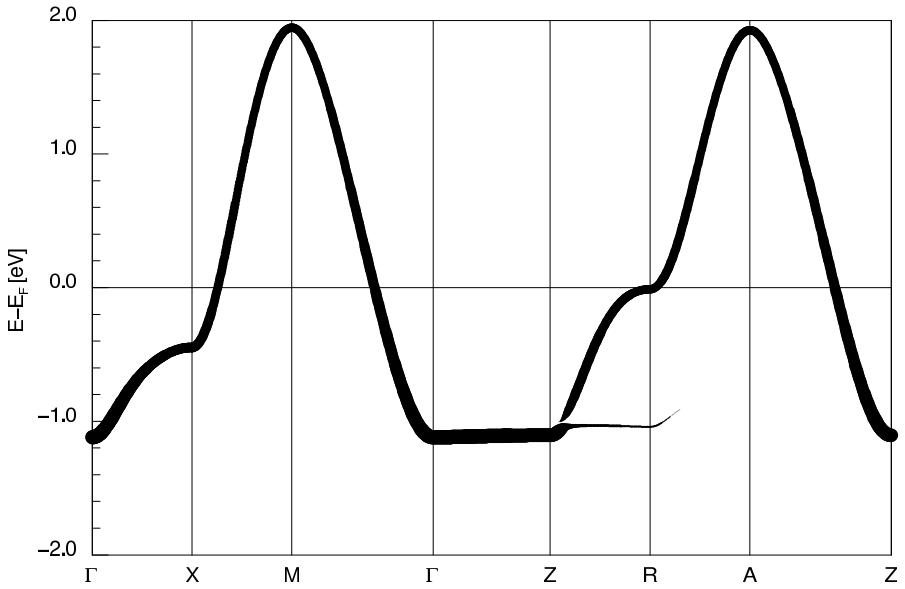

Figure 4.3. "Fatband" representation of Ni $3d(x^2 - y^2)$ in LDA. This band appears at first very two-dimensional, but is not because (1) the saddle point at $X(0, \pi/a, 0)$ is not midway between the Γ and $M(\pi/a, \pi/a, 0)$ energies, and (2) k_z dispersion between the X and $R(0, \pi/a, \pi/c)$.

Using a simple one-band tight binding model

$$\varepsilon_k = \varepsilon_\circ - \sum_R t_R \, e^{i\vec{k}\cdot\vec{R}},$$

the Ni $3d(x^2 - y^2)$ band shown in Fig. 4.3 can be reproduced with a few hopping amplitudes, but requiring more than might have been anticipated. The site energy is $\varepsilon_\circ = 93$ meV, slightly above the Fermi level, and the hopping integrals (in units of meV) are $t(100) = 381$, $t(110) = -81$, $t(001) = 58$ and $t(111) = -14$. There is no hopping along the (101) direction. As anticipated from the cuprates, the largest hopping is via $t(100)$. However, to correctly describe the k_z dispersion from X-R (*i.e.* along $\pi/a, 0, k_z$) together with

Table 4.1. Tight binding parameters (in units of meV) for Ni $3d(x^2-y^2)$ of $LaNiO_2$ and Cu $3d(x^2-y^2)$ of $CaCuO_2$. ε_0 is the site energy and t's are hopping integrals. *Ratio* (in %) is hopping integrals for $LaNiO_2$ to those for $CaCuO_2$.

parameters	$LaNiO_2$	$CaCuO_2$	$\|Ratio\|$ (%)
ε_0	93	-200	
$t(100)$	381	534	71
$t(110)$	-81	-84	96
$t(001)$	58	83	70
$t(101)$	0	-2	0
$t(111)$	-14	-19	74

the *lack of dispersion* from Γ-Z $(0,0,k_z)$ and also M-A $(\pi/a,\pi/a,k_z)$, the third neighbor hopping terms $t(111)$ must be included.

The comparison of the single band tight binding parameters with those of $CaCuO_2$ is given in Table I. It should be noted that the state in mind is an x^2-y^2 symmetry state that is orthogonal to those on neighboring Ni/Cu ions, *i.e.* an x^2-y^2 symmetry Wannier orbital. In Ni, the on-site energy is 0.3 eV above what it is in $CaCuO_2$, lying above E_F rather than below. This difference is partially due to the different Madelung potential in the two differently-charged compounds, but it also reflects some intrinsic hole-doping in the nickelate that leads to a lower Fermi level. The largest hopping amplitude (the conventional t) is 71% of its value in the cuprate, while the second (t') is essentially the same. The $t(001) \equiv t_z$ is also 70% of its value in the cuprate, while the other amplitudes

are the almost unchanged.

Fermiology

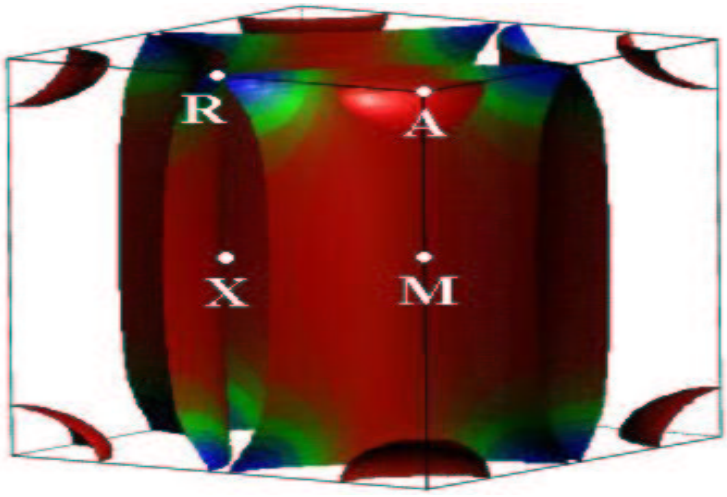

Figure 4.4. Paramagnetic Fermi surface in the local density approximation. In the center (not visible), i.e. Γ, there is a sphere (a radius $0.25(\pi/a)$) having $d(3z^2 - r^2)$ character of Ni and La. The cylinder with radius $0.8(\pi/a)$ contains Ni $d(x^2 - y^2)$ holes, whereas another sphere (a radius $0.4(\pi/a)$) at each corner contains Ni $d(zx)$ electrons.

The LDA Fermi surfaces are shown in Fig. 4.4. As for the cuprates, the Fermi surface is dominated by the M-centered hole barrel. In this system neighboring barrels touch at R=$(\pi/a, 0, \pi/c)$ because the saddle point at R happens to lie at E_F. The Fermi surfaces also include two spheres containing electrons. The sphere at Γ, with mixed Ni and La $d(3z^2 - r^2)$ character, contains about 0.02 electrons. The A-centered sphere is mainly Ni $d(zx)$ in character and contains approximately 0.07 electrons per Ni. The barrel, whose radius of 0.8 π/a in the (1,1,k_z) direction is almost independent of k_z but which varies

along (1,0,k_z), possesses about 1.1 holes, accounting for the total of the 1.0 hole that is required by Luttinger's theorem and also fits the formal Ni^{1+} valence (which, being a metal and also mixing with La as well as with O states, is not very relevant).

Magnetic Tendencies

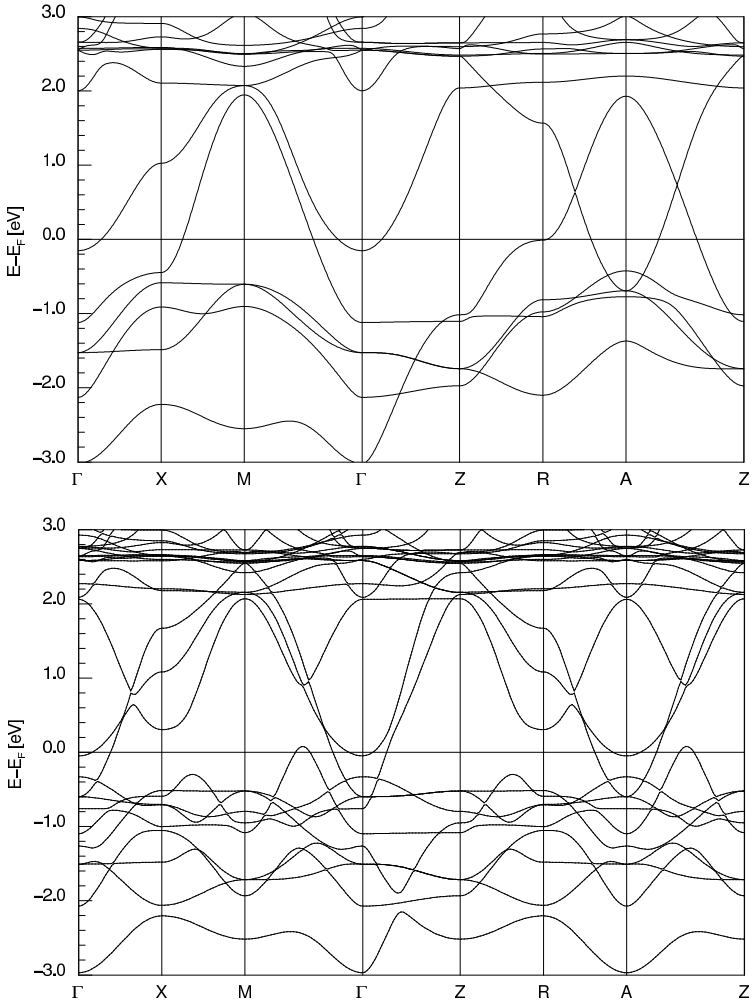

Figure 4.5. LDA antiferromagnetic band structure of $LaNiO_2$, graphed on the same energy scale. Top panel: paramagnetic; bottom panel: antiferromangetic. The Ni $3d$ bands lie above -3 eV and are disjoint from the O $2p$ bands (not shown) which begin just below -3 eV. The antiferromagnetism introduces the gap in the Ni $dp\sigma$ band midway between Γ and M in the range 0–1 eV. The symmetry points are given such as (0,0,x) for $\Gamma(Z)$, (1/2,1/2,x) for $X(R)$ and (1,0,x) for $M(A)$. x is zero for the first symbols and 1 for the symbols in parentheses.

To investigate magnetic tendencies, attempts to find both ferromagnetic (FM) and antiferromagnetic (AFM) states were made. A stable $\sqrt{2} \times \sqrt{2}$ AFM state, whose band structure is shown in Fig. 4.5, was obtained, with spin moment 0.53 μ_B per Ni. This state has lower energy by 13 meV/Ni than that of PM state. This is a very small energy difference for this size of moment, suggesting the energy versus moment curve is very flat. Just as for the paramagnetic case, the AFM state has entangled bands of La *5d*, Ni *3d* and O *2p* character near the Fermi energy. In contrast to the unpolarized case (and $CaCuO_2$), with AFM order the large electron pocket has primarily La $5d(xy)$ character and the slightly occupied electron pocket at Γ has a combination of La $5d(3z^2 - r^2)$ and Ni $3d(3z^2 - r^2)$ character. Attempts to obtain a FM solution always led to a vanishing moment.

The strong difference between $CaCuO_2$ and $LaNiO_2$ is therefore already evident from the LDA results as well as from the experimental data. $CaCuO_2$ is strongly AFM, a result which LDA entirely fails to predict, and only nonmagnetic solutions are found. $LaNiO_2$ shows no magnetism, whereas LDA finds the antiferromagnetically ordered state is lower in energy (albeit by a small amount). The differences between these two systems also are highlighted in the following sections.

4.4 Consideration of Correlations with LDA+U

As noted in Sec. 4.1, no magnetic order has been observed in $LaNiO_2$, either by magnetization or by neutron scattering. Although the local density approximation often does quite well in predicting magnetic moments, for weakly or nearly magnetic systems

renormalization by spin fluctuations becomes important[204, 239, 240] and such effects are not included in the local density approximation. The small energy difference in energy between the AFM and nonmagnetic solutions indicates the error is in some sense small.

There is still the unsettled question of the strength of correlation effects due to an intra-atomic repulsion U on the Ni site. For example, there is not yet any specific heat data to show whether the carrier mass is enhanced or not. Making the analogy to $CaCuO_2$ (same formal d^9 configuration, neighboring ion in the periodic table), which is a strong antiferromagnetic insulator, suggests that effects due to U might have some importance. As we have noted above, this analogy seems to be rather weak. Here we apply the LDA+U "correlated band theory" method to assess effects of intra-atomic repulsion and compare with observed behavior. In Sec. 4.5, we compare and contrast with $CaCuO_2$.

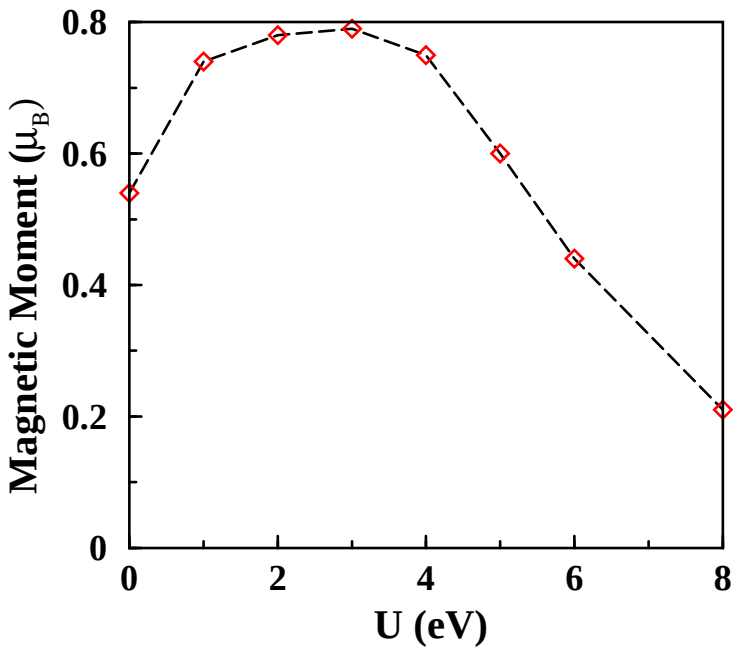

Figure 4.6. Behavior of the Ni magnetic moment vs the interaction strength U in antiferromangetic $LaNiO_2$.

Upon increasing U from zero in the antiferromagnetically ordered phase, the spin magnetic moment of Ni increases from the LDA value of 0.53 μ_B to a maximum of 0.8 μ_B at $U = 3$ eV. Surprisingly, for $U > 4$ eV the moment steadily decreases and by $U = 8$ eV it has *dropped* to 0.2 μ_B/Ni, which is less than half of its LDA value, as shown in Fig. 4.6. We emphasize that this behavior is unrelated to the observed behavior of $LaNiO_2$ (which is nonmagnetic). However, this unprecedented response of the transition metal ion to the imposition of a large U gives new insight into a feature of the LDA+U method that has not been observed previously. We now relate some details of the results that are intended to enhance our understanding of the LDA+U method in materials such as these; the remainder of this subsection is probably irrelevant to the interpretation of data on $LaNiO_2$.

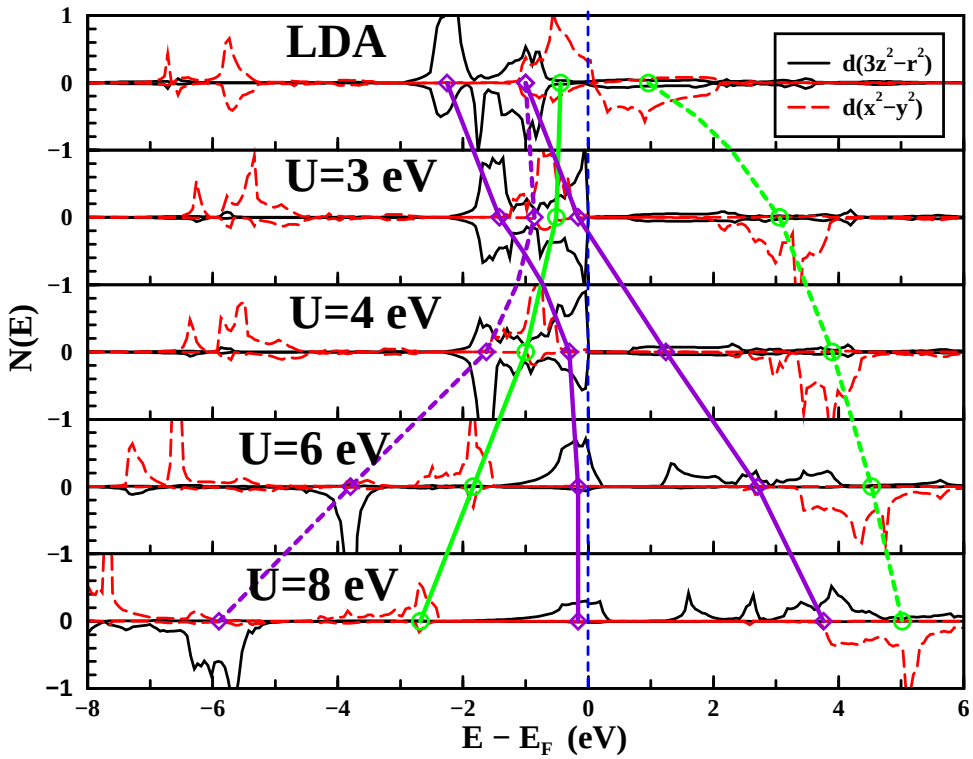

Figure 4.7. Change of the Ni $3d(3z^2 - r^2)$ and $3d(x^2 - y^2)$ densities of states as on-site Coulomb interaction U increases. One can easily identify a splitting ("Mott transition") of the $3d(x^2 - y^2)$ states occurring near U=0, and the light (green) lines outline their path with increasing U (majority is solid, minority is dashed). A distinct Mott transition involving oppositely directed moment of the $3d(3z^2 - r^2)$ states is outlined with the dark (purple) lines. This moment is oppositely directed. The conceptual picture is also complicated by the splitting even at U=0 which persists in the majority states, leaving a band at E_F with strong Ni $3d(3z^2 - r^2)$ character as well as the expected upper Hubbard band at 4 eV.

This "quenching" of the local moment with increasing U results from behavior of Ni $3d(3z^2 - r^2)$ states that is analogous to those of the $3d(x^2 - y^2)$, but with the

direction of spin inverted (then with additional complications). As usual for a d^9 ion in this environment, the majority $3d(x^2 - y^2)$ state of Ni is fully occupied even at U=2 eV, while the minority state is completely unoccupied at U=3 eV, where the moment is maximum and the system is essentially Ni^{1+} S=$\frac{1}{2}$. One can characterize this situation as a Mott insulating $3d(x^2 - y^2)$ orbital, as in the undoped cuprates. At U=3 eV, the density of states has a quasi one-dimensional van Hove singularity due to a flat band just below (bordering) the Fermi energy as can be seen in the $3d$ DOS shown in Fig. 4.7. Upon increasing U to 4 eV, rather than reinforcing the $S = \frac{1}{2}$ configuration of Ni and thereby forcing the La and O ions to cope with electron/hole doping, the Ni $d(3z^2 - r^2)$ states begin to polarize. The charge on the Ni ion drops somewhat, moving it in the $Ni^{1+} \rightarrow Ni^{2+}$ direction, with the charge going into the La $5d$ – O $2p$ states. Idealizing a bit, one might characterize the movement of (unoccupied) *majority* character of $3d(3z^2 - r^2)$ well above E_F as a Mott transition of these orbitals, which is not only *distinct from* that of the $3d(x^2 - y^2)$ states, but is *oppositely* directed, leading to an on-site "singlet" type of cancellation.

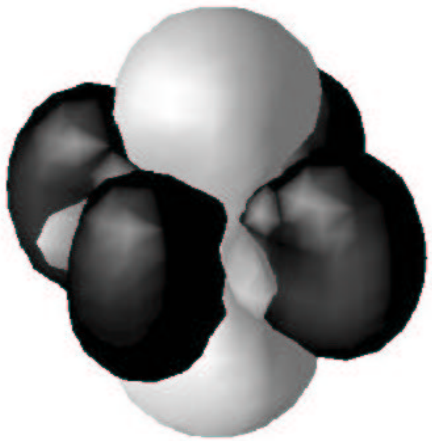

Figure 4.8. Isocontour plot of the spin density of the "singlet" Ni ion (U = 8 eV) when there is an $x^2 - y^2$ hole with spin up and a $3z^2 - r^2$ hole with spin down. Dark and light surfaces denote isocontours of equal magnitude but opposite sign.

This movement of states with increasing U has been emphasized in Fig. 4.7 for easier visualization. The resulting spin density on the transition metal ion at U=8 eV is pictured in Fig. 4.8. There is strong polarization in all directions from the core except for the position of nodes. The polarization is strongly positive (majority) in the lobes of the $3d(x^2 - y^2)$ orbital, and just as strongly negative (minority spin) in the lobes of the $3d(3z^2 - r^2)$ orbital. The net moment is (nearly) vanishing, but this results from a singlet combination (as nearly as it can be represented within classical spin picture) of spin-half up in one orbital and spin-half down in another orbital that violates Hund's first rule. The magnetization density is large throughout the ion, but integrates to (nearly) zero.

This behavior is however more complicated than a Mott splitting of occupied and unoccupied state, as can be seen from the substantial Ni $3d$ character that remains, even for U=8 eV, in a band straddling E_F while the rest of the weight moves to ~4 eV. In

both of these bands there is strong mixing with La $5d(xy)$ states. What happens is that as the "upper Hubbard $3d(3z^2 - r^2)$ band" rises as U is increased, it progressively mixes more strongly with the La $5d(xy)$ states, forming a bonding band and an antibonding band. While the antibonding combination continues to move upward with increasing U, the bonding combination forms a half-filled band which remains at E_F.

Thus we have found that for the Ni^{1+} ion in this environment, increasing U (well beyond what is physically plausible for $LaNiO_2$) results in $S = \frac{1}{2}$ Ni^{+1} being converted into a nominal Ni^{+2} ion (the actual charge changes little, however) in which the two holes are coupled into an intraatomic $S = 0$ singlet. This behavior involves yet a new kind of correlation between the $3d(3z^2 - r^2)$ states and the $3d(x^2 - y^2)$ states, but one which is due to (driven by) the local environment.

This behavior is quite different from the results for U=8 eV reported by Anisimov, Bukhvalov and Rice[234] using the Stuttgart TBLMTO-47 code. They obtained an AFM insulating solution analogous to that obtained for $CaCuO_2$,[15] with a single hole in the $3d$ shell occupying the $3d(x^2 - y^2)$ orbital that antibonds with the neighboring oxygen $2p_\sigma$ orbital. The reason for this difference is not known. Their code makes shape restriction on density and potential that are relaxed in our code, it appears that La $4f$ states were not included, and the LDA+U functional form was not strictly identical to what we have used, but we do not expect any of these differences would be responsible for the difference in solutions. It is established that multiple solutions to the LDA+U equations can occur,[241, 242] we have also found (in other applications)[73, 76] that different starting points can be used to encourage the discovery of alternative solutions. Our attempts to do so have always led only to the solutions given in Fig. 4.7.

4.5 Comparison with $CaCuO_2$

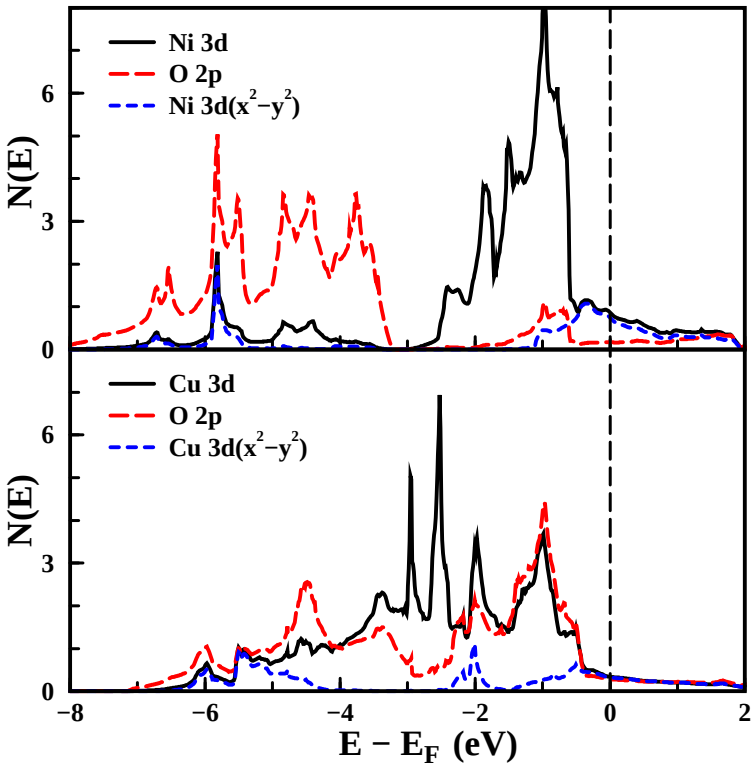

Figure 4.9. Comparison of LDA projected paramagnetic DOS $LaNiO_2$ (upper panel) and $CaCuO_2$ (lower panel). Note the separation of the Ni $3d$ states from the O $2p$ states in the upper panel, which does not occur for the more strongly hybridized cuprate.

Although Ni^{+1} is isoelectronic to Cu^{+2}, both the observed and the calculated behavior of $LaNiO_2$ are very different from $CaCuO_2$. In contrast to $CaCuO_2$, $LaNiO_2$ is (apparently) metallic, with no experimental evidence of magnetic ordering for $LaNiO_2$. The differing electronic and magnetic properties mainly arise from two factors. First, the Ca $3d$ bands lying in the range of 4 and 9 eV are very differently distributed from the broader and lower La $5d$ bands in the range of -0.2 and 8 eV. Second, in $CaCuO_2$, O $2p$ states extend to Fermi level and overlap strongly with Cu $3d$ states, and the difference

of the two centers is less than 1 eV, as can be seen in Fig. 4.9. Thus, there is a strong $2p - 3d$ hybridization that has been heavily discussed in high T_c materials. In $LaNiO_2$, however, Ni $3d$ states lie just below the Fermi level, with O $2p$ states located $3 - 4$ eV below the center of Ni bands. Therefore, $p - d$ hybridization, which plays a crucial role in the electronic structure and superconductivity of $CaCuO_2$, becomes much weaker.

4.6 Summary

Aside from the formal similarity to $CaCuO_2$, the interest in $LaNiO_2$ lies in the occurrence of the unusual monovalent Ni ion. As we have found and in apparent agreement with experiment, this compound is a metal, and the "charge state" of a transition metal atom in a metal usually has much less significance than it is in an insulator. It may be because the compound is metallic that it is stable, but in this study we are not addressing energetics and stability questions.

Hayward *et al.*[237] had already suggested that the experimental findings could arise from reduced covalency between the Ni $3d$ and O $2p$ orbitals, and the 30% smaller value of the hopping amplitude t indeed reflects the smaller covalency, as does the increased separation between the Ni $3d$ and O $2p$ bands. It is something of an enigma that in $CaCuO_2$ and other cuprates, LDA calculations fail to give the observed antiferromagnetic states, while in $LaNiO_2$ LDA predicts a weak antiferromagnetic state when there is no magnetism observed. In the cuprates the cause is known and is treated in a reasonable way by application of the LDA+U method. In this nickelate, application of the LDA+U method does not seem to be warranted (although novel behavior occurs it if it used).

Rather, the prediction of weak magnetism adds this compound to the small but growing number of systems ($ZrZn_2$,[243] Sc_3In,[244] and Ni_3Ga,[240] for example) in which the tendency toward magnetism is overestimated by the local density approximation. It appears that this tendency can be corrected by accounting for magnetic fluctuations.[239, 240] The isovalent compound $NdNiO_2$ reported by Hayward and Rosseinsky[238] may help to clarify this unusual nickelate system, although its microstructure is not simple and the Nd magnetism will impede the study of the Ni magnetic behavior.

Acknowledgment

We acknowledge useful communication with M. Hayward during the course of this research, and discussions with J. Kuneš and P. Novak about the behavior of the LDA+U method. This work was supported by National Science Foundation Grant No. DMR-0114818.

Chapter 5

Sr_2CoO_4 [1]

5.1 Introduction

First row ($3d$) transition metal ions in high oxidation states have been of interest for some time, due to their competing and delicate spin states. There are still several cases where behavior is not understood, indeed sometimes (due to sample questions arising from difficulty in synthesis) the data is not unambiguous. The best known, and most thoroughly studied, example is that of the quasi-two-dimensional (2D) cuprates, which when hole-doped become high temperature superconductors. In their undoped state they are Cu^{2+}-based antiferromagnetic insulators. Hole doping drives the Cu oxidation state toward the unstable (practically non-existent) Cu^{3+} state. At a doping level of 0.15–0.20 holes/Cu optimal superconductivity is reached. They can be doped beyond that level, when they become conventional metallic Fermi liquids. Upon hole doping the 'oxidation state' designation must be interpreted with care, since it is clear that the holes go onto

[1] This chapter has been published previously as a paper: "Correlation Effects in the High Formal Oxidation-state Compound Sr_2CoO_4", K.-W. Lee and W. E. Pickett, Phys. Rev. B **73**, 174428 (2006).

the oxygen ions to a large degree.

Another high-oxidation-state ion is Co^{4+}. This ion has recently gained wide exposure due to the unusual properties of Na_xCoO_2, including the discovery[39] that this system becomes superconducting (4.5 K) around x=0.3 when it is hydrated. This value of x suggests that the Co ion is 70% of the way to being Co^{4+}, or alternatively, 70% of the ions are Co^{4+} while 30% are Co^{3+}. This system is however metallic for all x except for Na ion/orbital/spin/charge ordering[53] precisely at x=0.5 (precisely what is responsible is not yet clear). There is magnetism and correlated electron behavior for $x > 0.5$ (the Co^{3+} end) while for $x < 0.5$ the materials appear to be weakly correlated nonmagnetic metals. While there has been much expectation that the (metastable) endpoint member CoO_2 (nominally Co^{4+}, d^5) is a Mott insulator, the evidence is that it remains a nonmagnetic metal.[214, 215] Calculations indicate[245] that, as in the cuprates, upon hole doping from the Co^{3+} end, much of the charge difference occurs on the O ion.

The $La_{2-x}Sr_xCoO_4$ system (LSCoO) with two-dimensional layered K_2NiF_4 structure has become interesting because of its magnetic and electrical properties. In this system the formal oxidation state $Co^{(2+x)+}$ near the La end is not unusually high, so its behavior might be expected to be readily understandable. With increasing Sr concentration x, LSCoO shows a structural transition from orthorhombic to tetragonal (i.e., a lattice constant $b \rightarrow a$) around x=0.5, with enhanced two-dimensional electronic properties.[246] The structural transition may be connected to an antiferromagnetic-ferromagnetic transition (the maximum Curie temperature T_C=220 K at x=0.9),[247] accompanying a magnetic change that has been interpreted in terms of a Co^{3+} spin-state transition from high spin to intermediate spin configurations around x=0.7.[248] There is another suggestion that

at x=1 the system is a high-spin, low-spin charge-ordered state.[249] However, there is no agreement amongst the measurements on the magnetic behavior [247, 250, 251, 252] nor metallic behavior[247, 253]. The end member x=0 is an antiferromagnetic (AFM) insulator with Neel temperature T_N=275 K.[254]

Although earlier studies were confined to the range below x=1.4, recently the end member Sr_2CoO_4, formally Co^{4+}, was synthesized by Matsuno *et al.*[255, 256] and by Wang *et al.*[257, 258], and characterized as FM with high Curie temperature $T_C \approx$250 K. However, their differing synthetic methods have led to different properties. Matsuno *et al.* synthesized a single-crystalline thin film using pulsed-laser deposition, while Wang *et al.* produced polycrystalline samples under high pressure, high temperature conditions. The former shows metallic T-dependent resistivity below T_C, although it has definitely higher resistivity of order of $10^{-4} - 10^{-3}$ Ω cm at low T than in a typical metal. The pressure-synthesized samples show nearly temperature independent resistivity (perhaps due to polycrystallinity), but with similar magnitude. The more confusing difference is in the observed saturation magnetic moment, 1.8 μ_B and 1 μ_B/Co respectively. Nevertheless, the sample with the smaller ordered moment has been observed[257] effective (Curie-Weiss) moment p_{eff}= 3.72 μ_B, characteristic of a much higher $S = 3/2$ spin configuration. Such a moment would suggest a much higher ordered moment, $< S_x > \sim 3\mu_B$.

The related perovskite system $La_{1-x}Sr_xCoO_3$ (formally $Co^{(3+x)+}$) has been studied for some time.[259, 260, 261, 262, 263, 264, 265] Its magnetic properties are also altered by Sr concentration x: nonmagnetic for $x < 0.05$, spin glass for $0.05 \leq x < 0.2$, and ferromagnetic above x=0.2. For the end member, $SrCoO_3$ ("Co^{4+}") shows metallic conductivity and has magnetic moments 1.25 and 0.1 μ_B for Co and O respectively,[259] whereas

the ground state of $LaCoO_3$ is a nonmagnetic band insulator. Excitations of $LaCoO_3$ have been interpreted in terms of a locally orbitally-ordered excited state.[265, 266]

In this paper, we look in some detail at the electronic and magnetic structure of Sr_2CoO_4 both as uncorrelated, using the local spin density approximation (LSDA), and viewing effects of correlation as described by the LDA+Hubbard U (LDA+U) method. Both commonly used LDA+U functionals are employed, and their results are compared and contrasted. A number of unusually rich magnetic phenomena arise (including a half metallic phase), reflecting the strong hybridization with O $2p$ states that complicates the accommodation of correlation effects on the Co ion.

5.2 Structure and Calculation

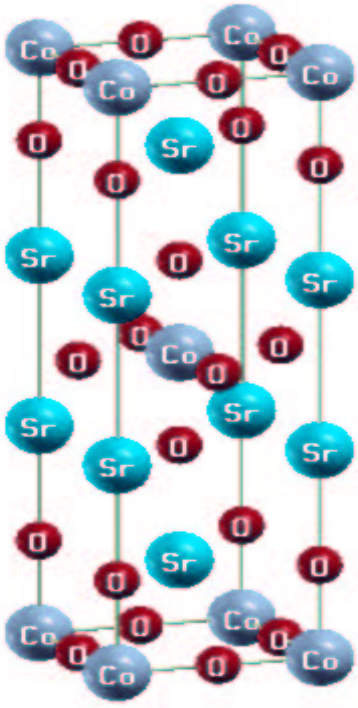

Figure 5.1. Crystal structure of Sr_2CoO_4, a body-centered-tetragonal type. The planar O-Co bond length is 1.878 Å, about 6% shorter than the apical O-Co bond length. Lattice constants used here are a=3.755 Å and c=12.6 Å.

Sr_2CoO_4 has the bct K_2NiF_4-type structure, space group $I4/mmm$ (No. 139), pictured in Fig. 5.1. The Co - planar O (PO) bond length (1.878 Å) is shorter by about 6% than that of Co - apical O (AO) (1.988 Å). The distorted CoO_6 octahedron, elongated along c-axis, leads to crystal field splitting of $t_{2g} \rightarrow \mathrm{E}_g(d_{xz}, d_{yz}) + \mathrm{B}_{2g}(d_{xy})$ and $e_g \rightarrow \mathrm{A}_g(d_{3z^2-r^2})$ + $\mathrm{B}_{1g}(d_{x^2-y^2})$ states. We have used the lattice constants a=3.755 Å, c=12.6 Å, and apical O (0.1578) and Sr (0.3544) internal parameters optimized by Matsuno *et al.*,[255] which are consistent with the experimentally measured values by Wang *et al.*[257]

Our calculations were carried out within the LSDA and LDA+U approaches with the full-potential nonorthogonal local-orbital (FPLO) method.[6] Both commonly used schemes, the so called"around mean field" (AMF)[18] and "fully localized limit" (FLL)[19], of the LDA+U method were employed so comparisons of the predictions could be made. The choice of basis orbitals were Sr $(4s4p)5s5p4d$, Co $(3s3p)4s4p3d$, and O $2s2p(3s3p3d)$. (The orbitals in parentheses indicate semi-core or polarization orbitals.) The Brillouin zone was sampled by a regular mesh containing up to 641 irreducible $\mathbf{k}$ points for LSDA and LDA+U, and 1639 irreducible $\mathbf{k}$ points for fixed spin moment (FSM)[25] calculations that require more carefully treatment near the Fermi level (E_F).

5.3 Uncorrelated Treatment

5.3.1 Electronic structure

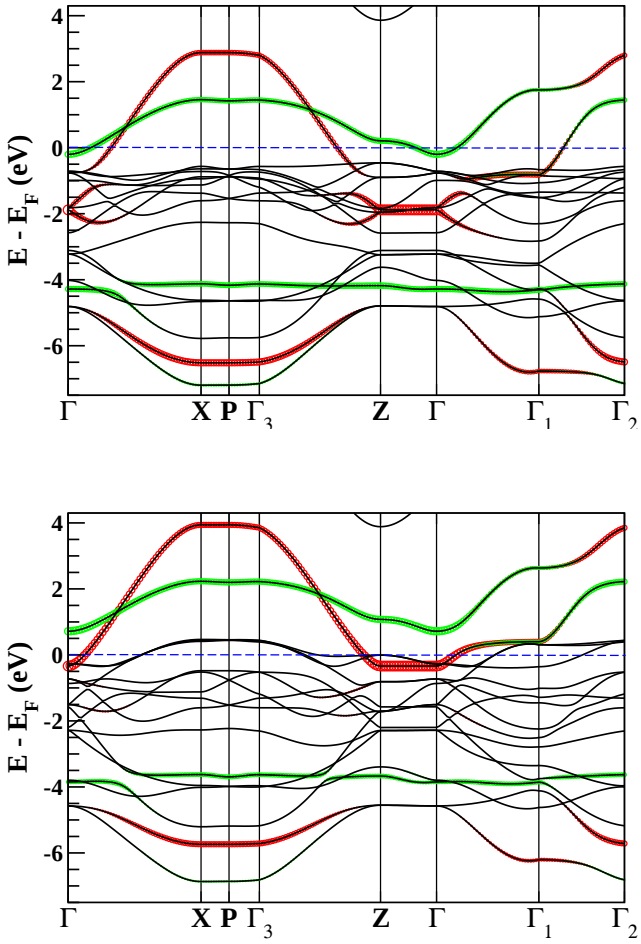

Figure 5.2. FM LSDA majority (top) and minority (bottom) band structures along symmetry directions. The thickened (and colored) lines emphasize Co $d_{3z^2-r^2}$ (green or light) and $d_{x^2-y^2}$ (red or black) characters, which form bonding and antibonding bands with apical and in-plane O p_σ states respectively. The symmetry points for the body-centered-tetragonal structure follow the Bradley and Cracknell notation as given in Fig. 5.6. The dashed horizontal line denotes the Fermi energy.

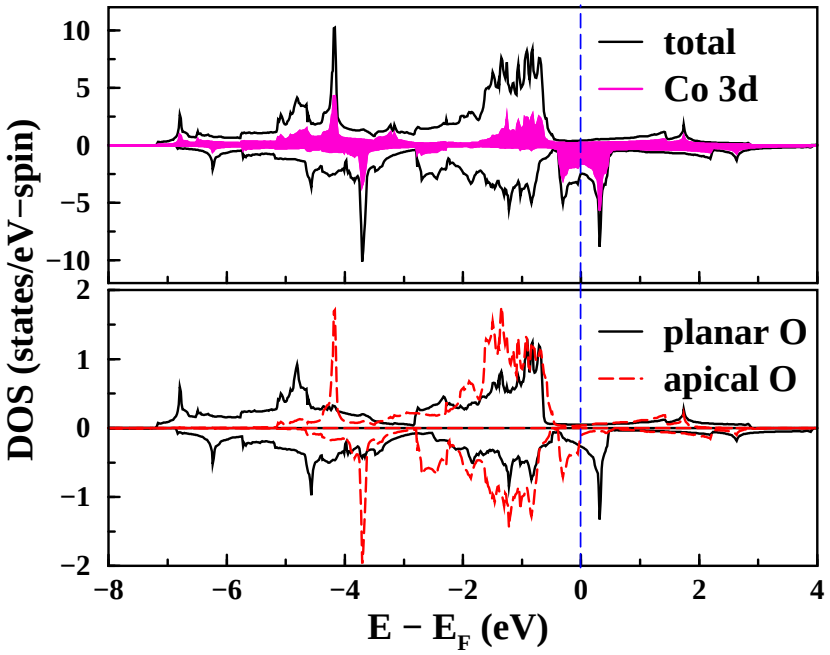

Figure 5.3. Total and atom-projected densities of states for LSDA FM calculation. Near E_F, there is a van Hove singularity in the minority channel. While AO is almost fully occupied, the minority of PO is partially occupied, resulting in large magnetic moment for PO (for details, see text). Additionally, the band width of AO is by 40% less than that of PO. The DOS at E_F $N(0)$ is 2.90 states/eV per both spins.

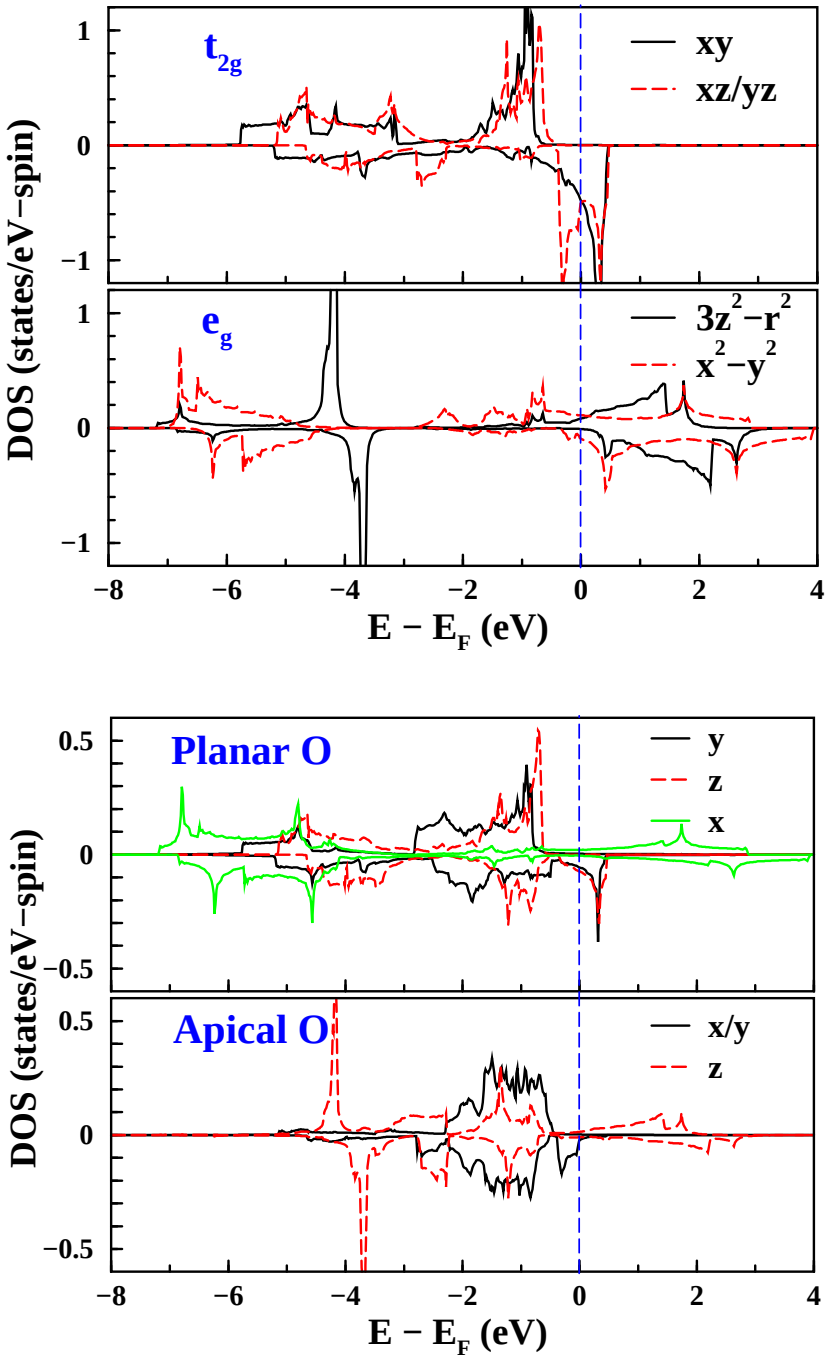

Figure 5.4. Orbital-projected densities of states for Co $3d$ (top) and O p states (bottom) in LSDA FM calculation. The d_{xz} and d_{yz} states are degenerate. The crystal field splitting of 2 eV between t_{2g} and e_g manifolds is only a little higher than the exchange splitting 1.3 eV. The PO p_x and AO p_z are the σ-orbital.

The FM LSDA band structures, exhibiting total magnetic moment M=1.95 μ_B that is only accidentally near an integer value, are shown in Fig. 5.2. The five Co $3d$ bands and three $2p$ bands of each O constitute an entanglement of 17 hybridized bands for each spin, with total $p-d$ bandwidths of 10 eV and 11 eV for the majority and minority bands respectively. The strong hybridization throughout the bands is evident in the corresponding total DOS and accompanying atom-projected DOS, shown in Fig. 5.3. The crystal field splitting of 2 eV, identified from the density of states, between t_{2g} and e_g manifolds is only a little higher than the exchange splitting 1.3 eV. As noted earlier, these t_{2g} and e_g designations are broken down by the $4/m$ symmetry of the Co site. The electronic structure shows clear quasi-two-dimensionality, consistent with resistivity measurement by Matsuno *et al.*

In Fig. 5.2, the $pd\sigma$ and $pd\sigma^*$ bands (for each of $d_{x^2-y^2}$ and $d_{3z^2-r^2}$ orbitals) are highlighted. The more dispersive bands (darker, or red) arise from bonding and antibonding interactions between Co $d_{x^2-y^2}$ and PO p_σ states. The bonding and antibonding bands have a separation of 10 eV at the X point, this total width arising from a combination of the differences between the t_{2g} and $2p$ site energies, and the hybridization between them. The dispersion of the antibonding (upper) band can be described roughly by effective hopping amplitude $t = 0.40$ eV (majority) and $t = 0.53$ eV (minority). The behavior of the $d_{x^2-y^2}$ band is similar to that observed in the high T_c superconductor La_2CuO_4, in which this antibonding band plays a central role,[267, 268] but it is mostly unoccupied here. However, with the lower number of $3d$ electrons the cobaltate electronic structure is influenced more strongly by the t_{2g} manifold, which forms relatively flat bands, the top of which hovers around the Fermi energy. In the minority bands a van Hove singularity

Table 5.1. Co $3d$ orbital (Mullikan) occupancy in LSDA, where M=1.95 μ_B. The difference of occupancies between both spin channels is directly related with contribution of each orbital to spin magnetic moment, which can be seen to be spread over all five $3d$ orbitals.

	t_{2g}			e_g	
	E_g		B_{2g}	A_g	B_{1g}
	xz	yz	xy	$3z^2-r^2$	x^2-y^2
majority	1.00	1.00	1.00	0.56	0.67
minority	0.68	0.68	0.54	0.36	0.32
difference	0.32	0.32	0.46	0.20	0.35

lies at E_F at the Z point, perhaps contributing to the positioning of the Fermi level and hence to the total moment.

The less dispersive highlighted bands (green, or lighter), lying in the 0–2 eV range, arise from the antibonding interaction of Co $d_{3z^2-r^2}$ and AO p_σ states. The bonding band of this pair consists of a remarkably flat band at -4 eV for each spin direction.

5.3.2 Magnetic Tendency

The FM state is favored energetically over the nonmagnetic state by 0.37 eV/Co, similar to the value given by Matsuno *et al.* The spin magnetic moments are 1.95 total, 1.52 from Co and 0.22 from each PO (in units of μ_B). The large magnetic moment for PO, due to strong hybridization with Co $3d$ bands, has been observed previously in Li_2CuO_2[269] and a few other cuprates. The Mullikan decomposition of O charges as well as the band

filling of related bands indicates that AO is consistent with its formal designation O^{2-}, whereas PO contributes considerably to the conduction bands and cannot be considered fully ionic. According to the Co $3d$ orbital occupancies given in Table 5.1, however, every $3d$ orbital contributes to the magnetic moment due to itineracy. The variation from average contribution occurs in two states: d_{xy} has 40% larger, and $d_{3z^2-r^2}$ orbital 40% smaller, contributions than the average contribution to the moment. The strong itinerant character (all $3d$ orbitals are neither fully occupied nor fully unoccupied) explains why no Jahn-Teller distortion is observed in Sr_2CoO_4.

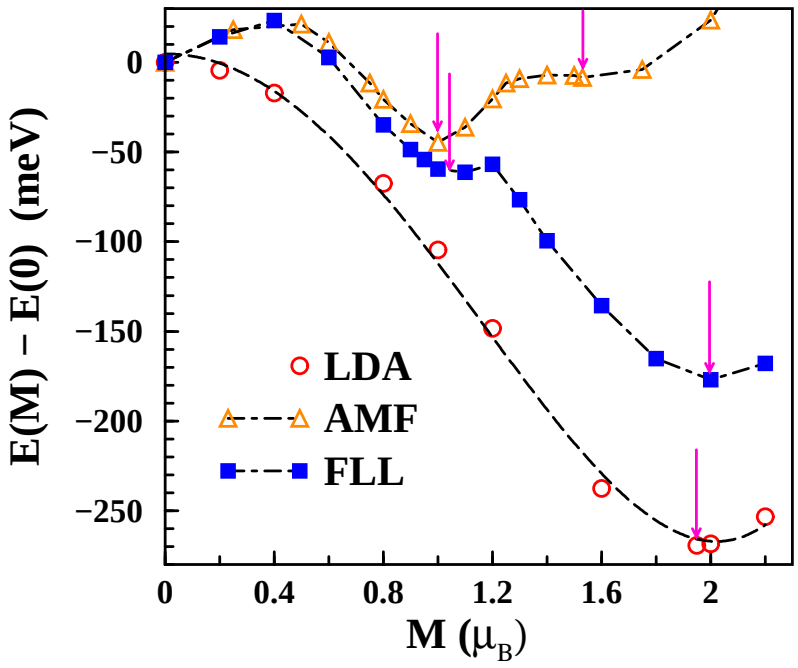

Figure 5.5. Fixed spin moment calculations in LSDA and both LDA+U schemes at U_c=2.5 eV. The arrows pinpoint (meta)stable states. The dashed line for LSDA FSM indicates fitting line with $E(M) - E(0) = \varepsilon_0 - \alpha M^2 + \beta M^4$, where ε_0=5 meV, α=133 meV/μ_B^2, and β=16 meV/μ_B^4.

The fixed spin moment method[25] is applied in a following subsection to probe the magnetic behavior. In the LSDA fixed spin moment calculations the low moment region is given by $E(M) - E(0) \approx -\alpha M^2 + \beta M^4$ with constants α=133 meV/μ_B^2, β=16 meV/μ_B^4. The Stoner-enhanced susceptibility is given by

$$\chi = \chi_0/[1 - N(0)I] \tag{5.1}$$

where the bare susceptibility $\chi_0 = 2\mu_B^2 N(0)$ and $N(0)$ is the single-spin density of states at the Fermi level. Also in the low-M limit one obtains formally $\alpha = (1/2)\chi^{-1}$, giving the Stoner interaction $I = 1.17(\pm 0.05)$ eV. With this value $IN(0) \approx 1.7$, giving a very strong Stoner instability of the nonmagnetic phase that is numerically similar to that of nonmagnetic Fe.

5.3.3 Fermiology

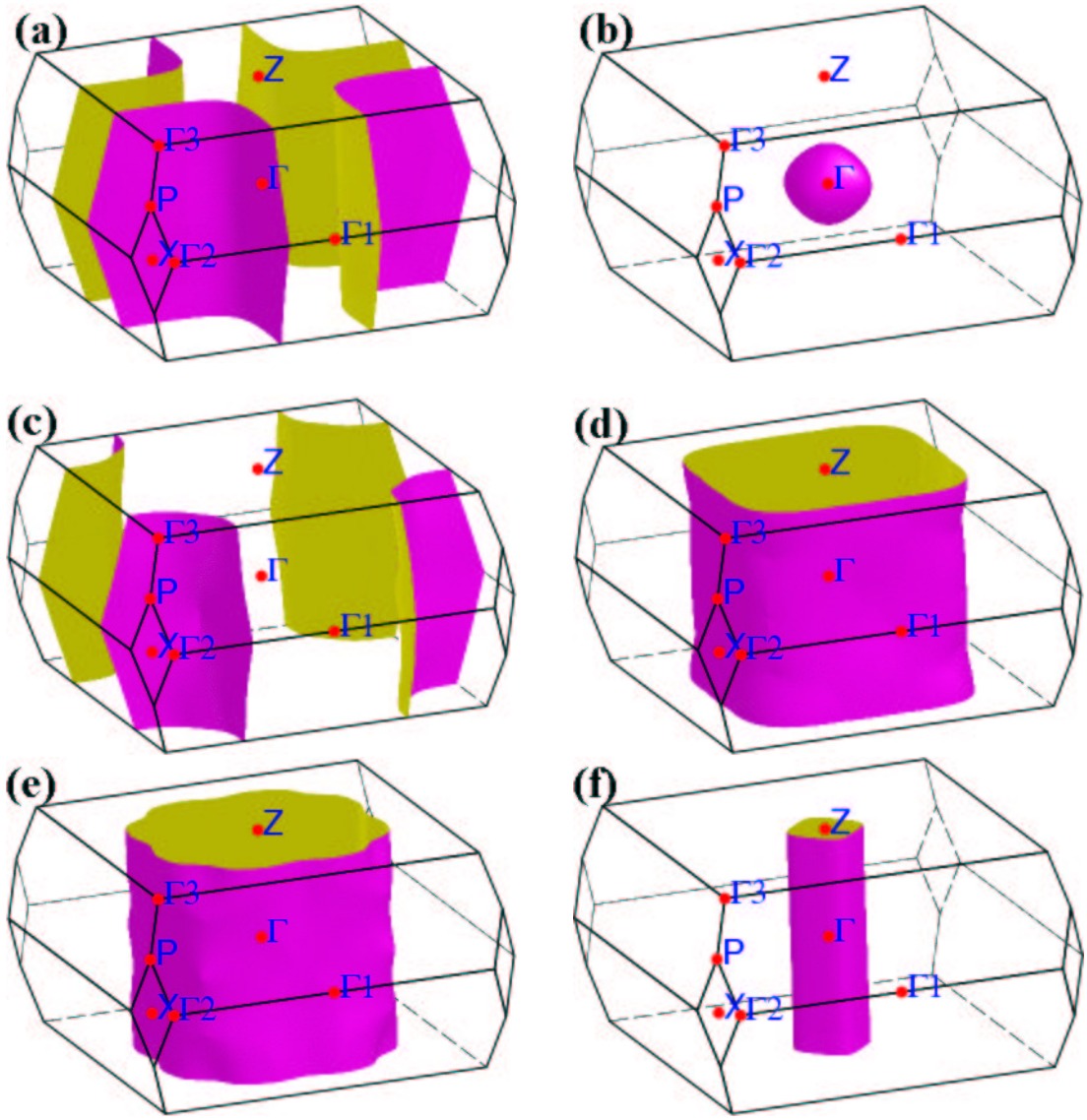

Figure 5.6. LSDA FM Fermi surfaces, for M= 1.95 μ_B. Surfaces (a) and (b) are from the majority states, surfaces (c)-(f) from the minority bands. While (a) and (c) contain holes, the others enclose electrons. Each surface has mainly (a) $d_{x^2-y^2}$ (0.5 holes), (b) $d_{3z^2-r^2}$ (0.01 electrons), (c) d_{xz} (0.2 holes), (d) d_{xy} (0.4 electrons), (e) d_{yz} (0.4 electrons), and (f) $d_{x^2-y^2}$ (0.02 electrons) characters. The number in parentheses says carrier number containing each Fermi surface per Co.

The LSDA FM Fermi surfaces (FS) pictured in Fig. 5.6 consist of two sheets from the majority states and four minority sheets, with very simple geometry and strong two-dimensionality. Except for one sheet that has an ellipsoidal shape (majority $d_{3z^2-r^2}$ character), the FSs have the shape of rectangular cylinders with rounded corners. The X-centered sheets contain holes, whereas the Γ-centered surfaces contain electrons. The FS arising from majority $d_{x^2-y^2}$ (Fig. 5.6(a)) has a clear nesting feature, as does the minority hole sheet in Fig. 5.6(d). The spanning vectors may lead to spin-density-wave or/and charge-density-wave instabilities. Intra-surface scattering may also show some nesting features. For the most part Fermi velocities v_F are in the range of a few 10^7 cm/sec as usual in a metal, but order of magnitude lower velocities occur along the Γ_3 to Z line at E_F.

5.4 Inclusion of Correlation effects

5.4.1 Metal to half-metal transition

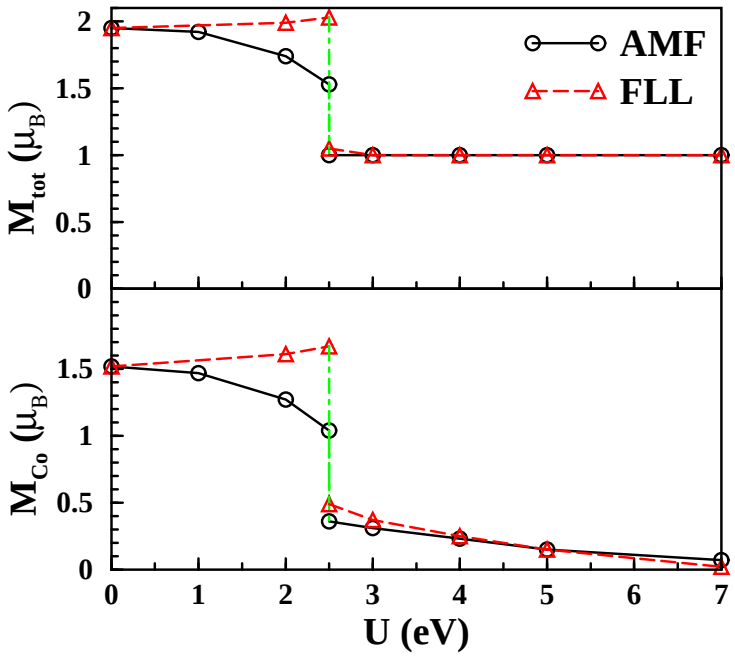

Figure 5.7. Effect of the on-site Coulomb repulsion U on total and Co local magnetic moments in both LDA+U schemes. At U_c=2.5 eV, a metal to half metal transition occurs. The first-order transition is obtained nearly at the same U in the both schemes. (In fact, the transition occurs a little higher U_c in FLL, but the difference is only less than a few tenth eV.)

Since the appropriate value of U in this and other cobaltate systems is unclear, we have studied the ground state as U is increased. The moment initially increases slightly in FLL, while it decreases slowly to 1.5 μ_B at U=2.5 eV in AMF, as shown in Fig. 5.7. From their separate states just below and at the critical value U_c=2.5 eV, beyond this critical value the moment drops sharply to 1 μ_B in both schemes, and then both schemes

produce very similar results in the entire region above U_c. Note particularly that this transition starts from distinct states, but occurs at the same value U_c to the same final state. Both high-moment and low-moment states can be stabilized in the calculations at U_c. Unlike studies in the Na_xCoO_2 system, no discernible hysteretic region could be found at this first-order transition. This magnetic collapse accompanies a metal to half metal transition, presumably because there is a particular stability of this half metallic (HM) FM state since both LDA+U schemes transition to it. The HM state, with a magnetic moment 1 μ_B, has been observed also by Wang *et al.* As U increases, the Co local magnetic moment decreases to vanishingly small value by $U \sim$6–7 eV. The state remains a HM FM, the moment has been pushed onto the PO ions. Since the moment on Co has vanished, it is not surprising that the two LDA+U schemes give the same result.

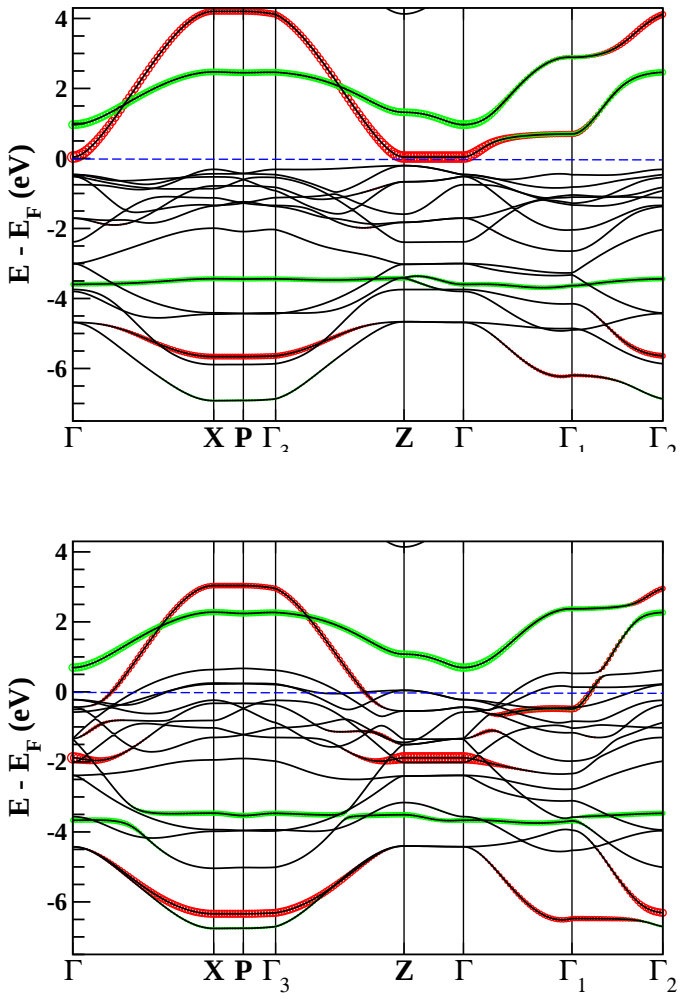

Figure 5.8. LDA+U FM majority (top) and minority (bottom) band structures at U_c=2.5 eV in the half metallic state with M=1 μ_B. The majority state shows a gap of 0.25 eV. The thickened (and colored) lines emphasize Co $d_{3z^2-r^2}$ (green or light) and $d_{x^2-y^2}$ (red or black) characters. The dashed horizontal line denotes the Fermi energy.

The microscopic mechanism behind the magnetic collapse induced by the on-site Coulomb repulsion U can be unraveled from a study of the charge decompositions in Tables 5.1 and 5.2, and comparison of band structures. We can compare and contrast

Table 5.2. Co $3d$ orbital occupancy in half metallic state, having M=1 μ_B, at U=2.5 eV. Compared with LSDA result shown in Table 5.1, there are two remarkable changes in the e_g state; nearly vanishing contribution of $d_{3z^2-r^2}$ and negative contribution of $d_{x^2-y^2}$ (for details, see text). It seems to be close to LS state, but the $d_{x^2-y^2}$ minority has considerable occupancy due to strong hybridization (itinerary) which makes impossible to be called strictly as LS state. The total occupation is 6.79.

	t_{2g}			e_g	
	E_g		B_{2g}	A_g	B_{1g}
	xz	yz	xy	$3z^2-r^2$	x^2-y^2
majority	1.00	1.00	1.01	0.35	0.25
minority	0.81	0.81	0.44	0.44	0.68
difference	0.19	0.19	0.57	-0.09	-0.43

the two viewpoints. First we point out that, while the Mullikan charges given in these tables are somewhat basis set dependent so their specific magnitude should not be given undue significance, differences – whether between orbitals or between spin-projections – are more physical. Then, while these orbital occupations provide one characterization, we have also provided in Figs. 5.2 and 5.8 by the fatbands technique, the bands that one identifies with $d_{x^2-y^2}$ and $d_{3z^2-r^2}$ character. Using both viewpoints provides a more robust interpretation of behavior than either separately.

From the tables one can determine that increasing U does not change the total $3d$ occupation, but introduces rearrangements in the $3d$ charge and moment. From the

bands, the main difference (between FM LSDA and HM FM LDA+U) is that the dispersive majority $d_{x^2-y^2}$ band has become fully *un*occupied, leaving the small gap that results in half metallicity. Returning to the charges and moments, what stands out is that the moment on the $d_{x^2-y^2}$ orbital has flipped, from $+0.35\mu_B$ to -0.43μ_B. The $d_{3z^2-r^2}$ moment has undergone a smaller change in the same manner: $0.20\mu_B$ to $-0.09\mu_B$. Thus the net moment on the Co ion, which is $\sim 0.5\mu_B$, is the result of $\sim +1\mu_B$ in the t_{2g} orbitals (primarily d_{xy}) and $\sim -0.5\mu_B$ in the e_g orbitals. This type of cancellation, in more striking form, has been seen previously in LDA+U resultsfor $LaNiO_2$,[270] which has an unusually *low* formal oxidation state for a nickelate.

5.4.2 Fixed spin moment calculations at U_c

The results of the previous section show that two magnetic states coexist at U_c in LDA+U, whether one uses the AMF or FLL functional. Such a coexistence has been already observed in LDA+U calculations for the sodium cobaltates, where the change at U_c corresponds to a charge disproportionation transition.[73] Here the change is simply in the state of the (single) Co ion; there is no experimental indication of disproportionation here. Here we analyze the FSM results at U_c for LSDA, AMF, and FLL.

The energy versus total magnetic moment behavior, displayed in Fig. 5.5, shows very interesting differences as well as similarities. Perhaps most interesting is that positions of local minima occur at (or near) integer values M=0, 1, and 2 (in units of μ_B), as if there might be underlying states with $S_z = 0, \frac{1}{2}$, or 1 pervading the behavior. The results of previous sections however established that there is strong $d-p$ hybridization which renders integral moments no more favored than other values. The LSDA curve

shows simple behavior: a Stoner instability at M=0 and a single minimum near (but not precisely at) M=2. The LDA+U results show more interesting variation.

For both AMF and FLL the paramagnetic state is metastable, with energy rising up to a moment $M \approx 0.5$, and then decreasing very similarly to the minimum at M=1. Beyond that point, AMF levels off to a broad flat region M=1.3–1.8 beyond which it increases with M. FLL however switches over to a separate phase, with its minimum at M=2. The E(M) curve for FLL seems to consist of two separate parabolas (different phases) with minima very near M=1 and M=2. The M=1 result is integral because a half metallic phase is encountered (see Fig. 5.8) and not due to an $S = 1/2$ configuration of the Co ion. Both majority $d_{x^2-y^2}$ and $d_{3z^2-r^2}$ become completely unoccupied, leaving a small gap to the t_{2g} bands.

We must point out that for both AMF and FLL schemes, the minimum at M=0 μ_B does not correspond to a nonmagnetic state. There is a moment on Co with magnitude 0.14 μ_B that is canceled by magnetization on the PO ion. The driving force for favoring this low, canceling moment phase over a nonmagnetic state is not clear. Possibly an antiferromagnetic result, requiring a doubled unit cell, would be a lower energy M=0 solution.

5.4.3 Strong interaction regime

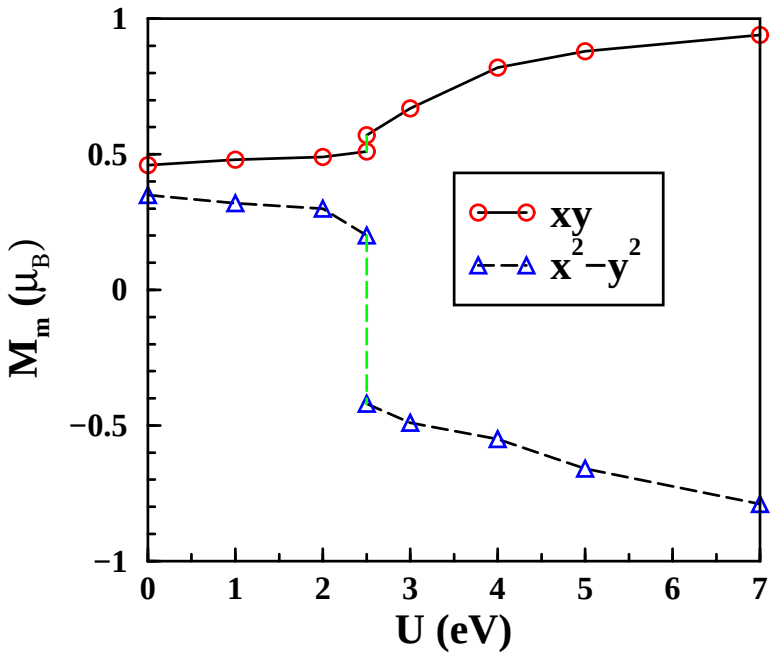

Figure 5.9. Effect of strength of U on the orbital-projected Co magnetic moment M_m, defined by difference between majority and minority occupancies, of Co $d_{x^2-y^2}$ and d_{xy} states in AMF scheme. (Results for the FLL scheme are similar.) In the large U limit an on-site "singlet" type cancellation of moments occurs in this $m = \pm 2$ channel (see Fig. 5.7 and text).

In Sr_2CoO_4 correlation effects should not be very strong it seems, since LSDA already gives a FM state that seems consistent with one of the experimental reports. However, in a strong correlated regime, but not beyond realistic range of U, there is another interesting feature. Figure 5.9 shows the U-dependent orbital-projected local magnetic moment M_m, defined by the difference between majority and minority occupancies, of Co $d_{x^2-y^2}$ and d_{xy} states. Upon increasing U, the d_{xy} minority state loses electrons, while

the $d_{x^2-y^2}$ minority state gains electrons. Beyond $U = U_c = 2.5$ eV, d_{xy} and $d_{x^2-y^2}$ have large positive and negative local magnetic moments respectively, leading to an on-site "singlet" type cancellation within this $|m| = 2$ channel. This type of cancellation, but within the e_g manifold, has been seen already in our previous results for $LaNiO_2$.[270] In contrast with $LaNiO_2$, which shows the cancellation in the total magnetic moment and $Ni^{1+} \rightarrow Ni^{2+}$ conversion, the moment of the system remains unchanged because of large magnetic moments on planar oxygen ions.

5.5 Summary

Synthesis of the high formal oxidation state compound Sr_2CoO_4, bulk materials by high-pressure high-temperature techniques and films by pulsed laser deposition (PLD), have led to a high Curie temperature metallic ferromagnet that introduces new transition metal oxide physics and may be useful in spin electronics devices. We have provided an in-depth study of the electronic and magnetic structure of this compound, looking specifically into the combined effects of correlation on the $3d$ orbitals and strong hybridization with O $2p$ states.

Within LSDA Sr_2CoO_4 is metallic with a ferromagnetic moment near $2\mu_B$, close to the saturation magnetization reported for the PLD films. Application of the two commonly used LDA+U functionals reveals several surprises. As U is increased from zero, the two functionals produce changes in the moment of opposite sign up to the critical value U_c=2.5 eV. Beyond half metallic ferromagnetic phase with moment $1\mu_B$. Within this phase, increasing the value of U has the effect of pushing the moment completely off

the Co and onto the planar O ions by U ~6–7 eV, while the total moment remains fixed at $1\mu_B$.

With U fixed at U_c=2.5 eV, fixed spin moment calculations were carried out for both LDA+U functionals, and compared with the corresponding LSDA result. Both LDA+U schemes behaved similarly out to a minimum at $1\mu_B$ (the half metallic state). Beyond this the two functionals departed in their behavior, with the FLL scheme jumping to a new state with minimum very near $2\mu_B$, not half metallic and much the same as the LSDA minimum ($1.95\mu_B$). In the stronger-interacting regime $U \geq 3$ eV (which may not be appropriate for Sr_2CoO_4), the correlation described by the LDA+U approach leads to oppositely directed moments on the $d_{x^2-y^2}$ and d_{xy} orbitals, reflecting the strong difference in hybridization of these two orbitals.

Acknowledgments

We acknowledge illuminating conversations with M. Richter and K. Koepernik. This work was supported by DOE grant DE-FG03-01ER45876 and DOE's Computational Materials Science Network. W.E.P. acknowledges the stimulating influence of DOE's Stockpile Stewardship Academic Alliance Program.

Bibliography

[1] W. Kohn, Nobel Lecture: Electronic structure of matter–wave functions and density functionals. *Rev. Mod. Phys.* **71**, 1253 (1999).

[2] P. Hohenberg and W. Kohn, Inhomogeneous Electron Gas. *Phys. Rev.* **136**, B864 (1964).

[3] W. Kohn and L. J. Sham, Self-Consistent Equations Including Exchange and Correlation Effects. *Phys. Rev.* **140**, A1133 (1965).

[4] Y. Wang and R. Parr, Construction of exact Kohn-Sham orbitals from a given electron density. *Phys. Rev. A* **47**, 1591 (1993).

[5] W. E. Pickett, Pseudopotential Methods in Condensed Matter Applications. *Comput. Phys. Rep.* **9**, 115 (1989).

[6] K. Koepernik and H. Eschrig, Full-potential nonorthogonal local-orbital minimum-basis band-structure scheme. *Phys. Rev. B* **59**, 1743 (1999).

[7] H. Eshrig, *Optimized LCAO Method and the Electronic Structure of Extended Systems* (Springer, Berlin, 1989).

[8] S. Massidda, M. Posternak, and A. Baldereschi, Hartree-Fock LAPW approach to the electronic properties of periodic systems. *Phys. Rev. B* **48**, 5058 (1993).

[9] L. Hedin, New Method for Calculating the One-Particle Green's Function with Application to the Electron-Gas Problem. *Phys. Rev* **139**, A796 (1965).

[10] O. Gunnarsson, O. K. Andersen, O. Jepsen, and J. Zaanen, Density-functional calculation of the parameters in the Anderson model: Application to Mn in CdTe. *Phys. Rev. B* **39**, 1708 (1989).

[11] V. I. Anisimov and O. Gunnarsson, Density-functional calculation of effective Coulomb interaction in metals. *Phys. Rev. B* **43**, 7570 (1991).

[12] V. I. Anisimov, J. Zaanen, and O. K. Andersen, Band theory and Mott insulators: Hubbard U instead of Stoner I. *Phys. Rev. B* **44**, 943 (1991).

[13] For a review, see V. I. Anisimov, F. Aryasetiawan, and A. I. Lichtenstein, First-principles calculations of the electronic structure and spectra of strongly correlated systems: the LDA+U method. *J. Phys.:Condens. Matter.* **9**, 767 (1997).

[14] A. I. Lichtenstein, V. I. Anisimov, and J. Zaanen, Density-functional theory and strong interactions: Orbital ordering in Mott-Hubbard insulators. *Phys. Rev. B* **52**, R5467 (1995).

[15] For implementation in FPLO, see H. Eschrig, K. Koepernik, and I. Chaplygin, Density functional application to strongly correlated electron systems. *J. Solid State Chem.* **176**, 482 (2003).

[16] J. C. Slater, *Quantum Theory of Atomic Structure*, (McGraw-Hill, New York, 1960), Vol. 1.

[17] F. M. F. de Groot, J. C. Fuggle, B. T. Thole, and G. A. Sawatzky, $2p$ x-ray absorption of 3d transition-metal compounds: An atomic multiplet description including the crystal field. *Phys. Rev. B* **42**, 5459 (1990).

[18] M. T. Czyzyk and G. A. Sawatzky, Local-density functional and on-site correlations: The electronic structure of La_2CuO_4 and $LaCuO_3$. *Phys. Rev. B* **49**, 14211 (1994).

[19] V. I. Anisimov, I. V. Solovyev, M. A. Korotin, M. T. Czyzyk, and G. A. Sawatzky, Density-functional theory and NiO photoemission spectra. *Phys. Rev. B* **48**, 16929 (1993).

[20] S. L. Dudarev, G. A. Botton, S. Y. Savrasov, C. J. Humphreys, and A. P. Sutton, Electron-energy-loss spectra and the structural stability of nickel oxide: An LSDA+U study. *Phys. Rev. B* **57**, 1505 (1998).

[21] C. Herring, in *Magnetism*, edited by G. T. Rado and H. Suhl (Academic, New York, 1966), Vol. IV.

[22] I. V. Solovyev and P. H. Dederichs, *Ab initio* calculations of Coulomb U parameters for transition-metal impurities. *Phys. Rev. B* **49**, 6736 (1994).

[23] A. K. McMahan, R. M. Martin, and S. Satpathy, Calculated effective Hamiltonian for La_2CuO_4 and solution in the impurity Anderson approximation. *Phys. Rev. B* **38**, 6650 (1988).

[24] I. V. Solovyev and M. Imada, Screening of Coulomb interactions in transition metals. *Phys. Rev. B* **71**, 045103 (2005).

[25] K. Schwarz and P. Mohn, Itinerant metamagnetism in YCo_2. *J. Phys. F: Met. Phys.* **14**, L129 (1984).

[26] V. L. Moruzzi, P. M. Marcus, and J. Kübler, Magnetovolume instabilities and ferromagnetism versus antiferromagnetism in bulk fcc iron and manganese. *Phys. Rev. B* 39, 6957 (1989).

[27] M. Kuzmin, (unpulished).

[28] For a recent review, see G. Mahan, B. Sales, and J. Sharp, Thermoelectric Materials: New Approaches to An Old Problem. *Physics Today*, pp. 42 (March, 1997).

[29] M. P. Marder, *Condensed Matter Physics* (John Wieley& Sons, Inc., 2000).

[30] I. Terasaki, Y. Sasago, and K. Uchinokura, Large thermoelectric power in $NaCo_2O_4$ single crystals. *Phys. Rev. B* **56**, R12685 (1997).

[31] K. Fujita, T. Mochida, and K. Nakamura, High-Temperature Thermoelectric Properties of $Na_xCoO_{2-\delta}$ Single Crystals. *Jpn. J. Appl. Phys.* **40**, 4644 (2001).

[32] T. Motohashi, E. Naujalis, R. Ueda, K. Isawa, M. Karppinen, and H. Yamauchi, Simultaneously enhanced thermoelectric power and reduced resistivity of $Na_xCo_2O_4$ by controlling Na nonstoichiometry. *Appl. Phys. Lett.* **79**, 1480 (2001).

[33] Y. Ono, R. Ishikawa, Y. Miyazaki, Y. Ishii, Y. Morlii, and T. Kajitani, Crystal

Structure, Electric and Magnetic Properties of Layered Cobaltite β-Na_xCoO_2. *J. Solid State Chem.* **166**, 177 (2002).

[34] M. Mikami, M. Yoshimura, Y. Mori, T. Sasaki, R. Funahashi, and M. Shikano, Thermoelectric Properties of Two Na_xCoO_2 Crystallographic Phases. *Jpn. J. Appl. Phys.* **42**, 7383 (2003).

[35] B. C. Sales, R. Jin, K. A. Affholter, P. Khalifah, G. M. Veith, and D. Mandrus, Magnetic, thermodynamic, and transport characterization of $Na_{0.75}CoO_2$ single crystals. *Phys. Rev. B* **70**, 174419 (2004).

[36] H. Kishan, V. P. S. Awana, M. A. Ansari, Anurag Gupta, R. B. Saxena, V. Ganesan, A. V. Narlikar, C. A. Cardoso, R. Nirmala, D. Buddhikot, and S. K. Malik, Resistivity and thermoelectric power of Na_xCoO_2 (x=1.0, 0.7, and 0.6) system. *J. Appl. Phys.* **97**, 10A904 (2005).

[37] H. Sakurai, N. Tsujil, and E. Takayama-Muromachi, Thermal and Electrical Properties of γ-Na_xCoO_2 ($0.70 \leq x \leq 0.78$). *J. Phys. Soc. Jpn.***73**, 2393 (2004).

[38] Y. Wang, N. S. Rogado, R. J. Cava, and N. P. Ong, Spin entropy as the likely source of enhanced thermopower in $Na_xCo_2O_4$. *Nature* (London) **423**, 425 (2003).

[39] K. Takada, H. Sakurai, E. Takayama-Muromachi, F. Izumi, R. A. Dilanian, and T. Sasaki, Superconductivity in two-dimensional CoO_2 layers. *Nature* (London) **422**, 53 (2003).

[40] H. Sakurai, K. Takada, S. Yoshii, T. Sasaki, K. Kindo, and E. Takayama-Muromachi, Unconventional upper– and lower–critical fields and normal–state magnetic suscep-

tibility of the superconducting compound $Na_{0.35}CoO_2{\cdot}1.3H_2O$. *Phys. Rev. B* **68**, 132507 (2003).

[41] B. Lorenz, J. Cmaidalka, R. L. Meng, and C. W. Chu, Effect of hydrostatic pressure on the superconductivity in $Na_xCoO_2{\cdot}yH_2O$. *Phys. Rev. B* **68**, 132504 (2003).

[42] B. G. Ueland, P. Schiffer, R. E. Schaak, M. L. Foo, V. L. Miller, and R. J. Cava, Specific heat study of the $Na_{0.3}CoO_2{\cdot}1.3H_2O$ superconductor: influence of the complex chemistry. *Physica C* **402**, 27 (2004).

[43] G. Cao, C. Feng, Y. Xu, W. Lu, J. Shen, M. Fang, and Z. Xu, Superconductivity in a layered cobalt oxyhydrate $Na_{0.31}CoO_2{\cdot}1.3H_2O$. *J. Phys.: Condens. Matt.* **15**, L519 (2003).

[44] M. Kato, C. Michioka, T. Waki, Y. Itoh, K. Yoshimura, K. Ishida, H. Sakurai, E. Takayama-Muromachi, K. Takada, and T. Sasaki, Possible Spin-triplet Superconductivity in $Na_xCoO_2{\cdot}yH_2O$ – ^{59}Co NMR Study. *J. Phys.: Condens. Matter* **18**, 669 (2006).

[45] F. C. Chou, J. H. Cho, P. A. Lee, E. T. Abel, K. Matan, and Y. S. Lee, Thermodynamic and Transport Measurements of Superconducting $Na_{0.3}CoO_2{\cdot}1.3H_2O$ Single Crystals Prepared by Electrochemical Deintercalation. *Phys. Rev. Lett.* **92**, 157004 (2004).

[46] R. Jin, B. C. Sales, P. Khalifah, and D. Mandrus, Observation of Bulk Superconductivity in $Na_xCoO_2{\cdot}yH_2O$ and $Na_xCoO_2{\cdot}yD_2O$ Powder and Single Crystals. *Phy. Rev. Lett.* **91**, 217001 (2003).

[47] R. E. Schaak, T. Klimczuk, M. L. Foo, and R. J. Cava, Superconductivity phase diagram of $Na_xCoO_2 \cdot 1.3H_2O$. *Nature* **424**, 527 (2003).

[48] C. J. Milne, D. N. Argyriou, A. Chemseddine, N. Aliouane, J. Veira, S. Landsgesell, and D. Alber, Revised Superconducting Phase Diagram of Hole-Doped $Na_x(H_3O)_zCoO_2 \cdot yH_2O$. *Phys. Rev. Lett.* **93**, 247007 (2004).

[49] For review, see M. F. Collins and O. A. Petrenko, Triangular antiferromagnets. *Can. J. Phys.* **75**, 605 (1997).

[50] For recent review, see R. Moessner and A. P. Ramirez, Geometrical Frustration, *Physics Today*, pp. 24 (Feb. 2006).

[51] N. L. Wang, D. Wu, G. Li, X. H. Chen, C. H. Wang, and X. G. Luo, Infrared Spectroscopy of the Charge Ordering Transition of $Na_{0.5}CoO_2$. *Phys. Rev. Lett.* **93**, 147403 (2004).

[52] D. Wu, J. L. Luo, and N. L. Wang, Electron-boson mode coupling and the pseudogap of Na_xCoO_2 by infrared spectroscopy. *Phys. Rev. B* **73**, 014523 (2006).

[53] M. L. Foo, Y. Wang, S. Watauchi, H. W. Zandbergen, T. He, R. J. Cava, and N. P. Ong, Charge Ordering, Commensurability, and Metallicity in the Phase Diagram of the Layered Na_xCoO_2. *Phys. Rev. Lett.* **92**, 247001 (2004).

[54] S. Kikkawa, S. Miyazaki, and M. Koizumi, Deintercalated $NaCoO_2$ and $LiCoO_2$. *J. Solid State Chem.* **62**, 35 (1986).

[55] I. R. Mukhamedshin, H. Alloul, G. Collin, and N. Blanchard, ^{23}Na NMR Evidence

for Charge Order and Anomalous Magnetism in Na_xCoO_2. *Phys. Rev. Lett.* **93**, 167601 (2004).

[56] T. Motohashi, R. Ueda, E. Naujalis, T. Tojo, I. Terasaki, T. Atake, M. Karppinen, and H. Yamauchi, Unconventional magnetic transition and transport behavior in $Na_{0.75}CoO_2$. *Phys. Rev. B* **67**, 064406 (2003).

[57] J. Sugiyama, H. Itahara, J. H. Brewer, E, J. Ansaldo, T. Motohashi, M. Karppinen, and H. Yamauchi, Static magnetic order in $Na_{0.75}CoO_2$ detected by muon spin rotation and relaxation. *Phys. Rev. B* **67**, 214420 (2003).

[58] J. Sugiuyama, J. H. Brewer, E. J. Ansaldo, H. Itahara, T. Tani, M. Mikami, Y. Mori, T. Sasaki, S. Hébert, and A. Maignan, Dome-Shaped Magnetic Phase Diagram of Thermoelectric Layered Cobaltites. *Phys. Rev. Lett.* **92**, 017602 (2004).

[59] A. T. Boothroyd, R. Coldea, D. A. Tennant, D. Prabhakaran, L. M. Helme, and C. D. Frost, Ferromagnetic In-Plane Spin Fluctuations in Na_xCoO_2 Observed by Neutron Inelastic Scattering. *Phys. Rev. Lett.* **92**, 197201 (2004).

[60] Y. Ando, N. Miyamoto, K. Segawa, T. Kawata, and I. Terasaki, Specific-heat evidence for strong electron correlations in the thermoelectric material $(Na,Ca)Co_2O_4$. *Phys. Rev. B* **60**, 10580 (1999).

[61] R. Jin, B. C. Sales, S. Li, and D. Mandrus, Dependence of the specific heat of $Na_xCoO_2{\cdot}yH_2O/D_2O$ on sodium and water concentrations. *Phys. Rev. B* **72**, 060512(R) (2005).

[62] K. Miyoshi, E. Morikuni, K. Fujiwara, J. Takeuchi, and T. Hamasaki, Mass-enhanced Fermi-liquid ground state in $Na_{1.5}Co_2O_4$. *Phys. Rev. B* **69**, 132412 (2004).

[63] S. Lupi, M. Ortolani, and P. Calvani, Optical conductivity of single crystals of $Na_{0.57}CoO_2$. *Phys. Rev. B* **69**, 180506(R) (2004).

[64] G. Lang, J. Bobroff, H. Alloul, P. Mendels, N. Blanchard, and G. Collin, Evidence of a single nonmagnetic Co^{3+} state in the Na_1CoO_2 cobaltate. *Phys. Rev. B* **72**, 094404 (2005).

[65] C. de Vaulx, M.-H. Julien, C. Berthier, M. Horvatic, P. Bordet, V. Simonet, D. P. Chen, and C. T. Lin, Nonmagnetic Insulator State in Na_1CoO_2 and Phase Separation of Na Vacancies. *Phys. Rev. Lett.* **95**, 186405 (2005).

[66] P. Carretta, M. Mariani, C. B. Azzoni, M. C. Mozzati, I. Bradarić, I. Savić, A. Feher, and J. Šebek, Mesoscopic phase separation in Na_xCoO_2 ($0.65 \leq x \leq 0.75$). *Phys. Rev. B* **70**, 024409 (2004).

[67] J. L. Gavilano, D. Rau, B. Pedrini, J. Hinderer, H. R. Ott, S. M. Kazakov, and J. Karpinski, Unconventional charge ordering in $Na_{0.70}CoO_2$ below 300 K. *Phys. Rev. B* **69**, 100404(R) (2004).

[68] M. Pissas, V. Psycharis, D. Stamopoulos, G. Papavassiliou, Y. Sanakis, and A. Simopoulos, Mössbauer study of $Na_{0.82}CoO_2$ (doped by 1% ^{57}Fe). *cond-mat/0503662* (2005).

[69] F.L. Ning and T. Imai, ^{17}O NMR Studies of a Triangular-Lattice Superconductor $Na_xCoO_2{\cdot}yH_2O$. *Phys. Rev. Lett.* **94**, 227004 (2005).

[70] I. R. Mukhamedshin, H. Alloul, G. Collin, and N. Blanchard, ^{59}Co NMR Study of the Co States in Superconducting and Anhydrous Cobaltates. *Phys. Rev. Lett.* **94**, 247602 (2005).

[71] M. Yokoi, T. Moyoshi, Y. Kobayashi, M. Soda, Y. Yasui, M. Sato, and K. Kakurai, Magnetic Correlation of Na_xCoO_2 and Successive Phase Transitions of $Na_{0.5}CoO_2$: NMR and Neutron Diffraction Studies. *J. Phys. Soc. Jpn.* **74**, 3046 (2005).

[72] G. Gašparovič, R. A. Ott, J.-H. Cho, F. C. Chou, Y. Chu, J. W. Lynn, and Y. S. Lee, Neutron Scattering Study of Novel Magnetic Order in $Na_{0.5}CoO_2$. *Phys. Rev. Lett.* **96**, 046403 (2006).

[73] K.-W. Lee, J. Kuneš, P. Novak, and W. E. Pickett, Disproportionation, Metal-Insulator Transition, and Critical Interaction Strength in $Na_{1/2}CoO_2$. *Phys. Rev. Lett.* **94**, 026403 (2005).

[74] K.-W. Lee and W. E. Pickett, Charge and Spin Ordering in Insulating $Na_{0.5}CoO_2$: Effects of Correlation and Symmetry. *Phys. Rev. Lett.* **96**, 096403 (2006).

[75] Y. Kobayashi, M. Yokoi, and M. Sato, ^{59}Co-NMR Knight Shift of Superconducting $Na_xCoO_2{\cdot}yH_2O$. *J. Phys. Soc. Jpn.* **72**, 2453 (2003).

[76] K.-W. Lee, J. Kuneš, and W. E. Pickett, Charge disproportionation and spin ordering tendencies in Na_xCoO_2. *Phys. Rev. B* **70**, 045104 (2004).

[77] J. M. Tarascon (private communication).

[78] K. Takada, K. Fukuda, M. Osada, I. Nakai, F. Izumi, R. A. Dilanian, K. Kato, M. Takata, H. Sakurai, E. Takayama-Muromachi, and T. Sasaki, Chemical composition

and crystal structure of superconducting sodium cobalt oxide bilayer-hydrate. *J. Mater. Chem.* **14**, 1448 (2004).

[79] M. Karppinen, I. Asako, T. Motohashi, and H. Yamauchi, Oxidation State of Cobalt in the $Na_xCoO_{2-\delta}{\cdot}yH_2O$ Superconductor. *Chem. Mater.* **16**, 1693 (2004).

[80] K. Takada, H. Sakurai, E. Takayama-Muromachi, F. Izumi, R. A. Dilanian, and T. Sasaki, A New Superconducting Phase of Sodium Cobalt Oxide. *Adv. Mater.* **16**. 1901 (2004).

[81] C. H. Wang, H. T. Zhang, X. X. Lu, G. Wu, J. Q. Li, and X. H. Chen, Charge ordering in charge-compensated $Na_{0.41}CoO_2$ by oxonium ions. *Solid State Commun.* **138**, 169 (2006).

[82] D. J. Singh, Electronic structure of $NaCo_2O_4$. *Phys. Rev. B* **61**, 13397 (2000).

[83] R. Koretsune and M. Ogata, Resonating-Valence-Bond States and Ferromagnetic Correlations in the Doped Triangular Mott Insulator. *Phys. Rev. Lett.* **89**, 116401 (2002),

[84] M. Ogata, Superconducting States in Frustrating t-J Model: A Model Connecting High-Tc Cuprates, Organic Conductors and Na_xCoO_2. *J. Phys. Soc. Jpn.* **72**, 1839 (2003).

[85] B. Kumar and B. S. Shastry, Superconductivity in CoO_2 layers and the resonating valence bond mean-field theory of the triangular lattice t-J model. *Phys. Rev. B* **68**, 104508 (2003).

[86] R. Moessner and S. L. Sondhi, Resonating valence bond liquid physics on the triangular lattice. *Prog. Th. Phys. Suppl.* **145**, 37 (2002).

[87] Q.-H. Wang, D.-H. Lee, and P. A. Lee, Doped t-J model on a triangular lattice: Possible application to $Na_xCoO_2{\cdot}yH_2O$ and $Na_{1-x}TiO$. *Phys. Rev. B* **69**, 092504 (2004).

[88] A. Tanaka and X. Hu, Possible Spin Triplet Superconductivity in $Na_xCoO_2{\cdot}yH_2O$. *Phys. Rev. Lett.* **91**, 257006 (2003).

[89] C. Honerkamp, Instabilities of interacting electrons on the triangular lattice. *Phys. Rev. B* **68**, 104510 (2003).

[90] G. Baskaran, Electronic Model for CoO_2 Layer Based Systems: Chiral Resonating Valence Bond Metal and Superconductivity. *Phys. Rev. Lett.* **91**, 097003 (2003).

[91] G. Baskaran, How Ice enables Superconductivity in $Na_xCoO_2{\cdot}yH_2O$ by melting charge order: Possibility of novel Electric Field Effects. *Physica C* **417**, 150 (2005).

[92] W. Koshibae and S. Maekawa, Electronic State of a CoO_2 Layer with Hexagonal Structure: A Kagomé Lattice Structure in a Triangular Lattice. *Phys. Rev. Lett.* **91**, 257003 (2003).

[93] K.-W. Lee and W. E. Pickett, Disproportionation and Critical Interaction Strength in Na_xCoO_2: Concentration Dependence. *J. Appl. Phys.* **99**, 08P702 (2006).

[94] J. Kuneš, K.-W. Lee, and W. E. Pickett, Charge Disproportionation and Spin-Ordering Tendencies in Na_xCoO_2 at x=1/3. *New Challenges in Superconductivity:Experimental Advances and Emerging Theories*, edited by J. Ashkenazi, M.V.

Eremin, J. L. Cohn, I. Eremin, D. Manske, D. Pavuna, and F. Zuo (Kluwer Academic, Boston, 2004), p.235; *cond-mat/0308388*.

[95] K.-W. Lee and W. E. Pickett, Na_xCoO_2 in the $x \to 0$ regime: Coupling of structure and correlation effects. *Phys. Rev. B* **72**, 115110 (2005).

[96] E. R. Ylvisaker, K.-W. Lee, and W. E. Pickett, Comparison of the Electronic Structures of Two Non-cuprate Layered Transition Metal Oxide Superconductors. *Physica B* (in press, 2006).

[97] T. Mizokawa, L. H. Tjeng, H.-J. Lin, C. T. Chen, R. Kitawaki, I. Terasaki, S. Lambert, and C. Michel, X-ray absorption study of layered Co oxides with a Co-O triangular lattice. *Phys. Rev. B* **71**, 193107 (2005).

[98] Von M. Jansen and F. Hoppe, On Oxocobaltates $A_xCo_2O_4$ (A = Cs, Rb, K). *Z. Anorg. Allg. Chem.* **408**, 104 (1974).

[99] J. W. Lynn, Q. Huang, C. M. Brown, V. L. Miller, M. L. Foo, R. E. Schaak, C. Y. Jones, E. A. Mackey, and R. J. Cava, Structure and dynamics of superconducting Na_xCoO_2 hydrate and its unhydrated analog. *Phys. Rev. B* **68**, 214516 (2003).

[100] J. D. Jorgensen, M. Avdeev, D. G. Hinks, J. C. Burely, and S. Short, Crystal structure of the sodium cobaltate deuterate superconductor $Na_xCoO_2{\cdot}4xD_2O$ ($x \approx \frac{1}{3}$). *Phys. Rev. B* **68**, 214517 (2003).

[101] Q. Huang, M. L. Foo, R. A. Pascal, Jr., J. W. Lynn, B. H. Toby, T. He, H. W. Zandbergen, and R. J. Cava, Coupling between electronic and structural degrees

of freedom in the triangular lattice conductor Na_xCoO_2. *Phys. Rev. B* **70**, 184110 (2004).

[102] C.T. Lin, D.P. Chen, P. Lemmens, X.N. Zhang, A. Maljuk and P.X. Zhang, Study of intercalation/deintercalation of Na_xCoO_2 single crystals. *J. Cryst. Growth* **275**, 606 (2005).

[103] D. N. Argyriou, P. G. Radaelli, C. J. Milne, N. Aliouane, L. C. Chapon, A. Chemseddine, J. Veira, S. Cox, N. D. Mathur, and P. A. Midgley, Crystal structure of the superconducting layered cobaltate $Na_xCoO_2{\cdot}yD_2O$. *J. Phys.: Condens. Matter* **17**, 3293 (2005).

[104] P. Zhang, R. B. Capaz, M. L. Cohen, and S. G. Louie, Theory of sodium ordering in Na_xCoO_2. *Phys. Rev. B*, **71**, 153102 (2005).

[105] Y. S. Meng, A. Van der Ven, M. K. Y. Chan, and G. Ceder, *Ab initio* study of sodium ordering in $Na_{0.75}CoO_2$ and its relation to Co^{3+}/Co^{4+} charge ordering. *Phys. Rev. B*, **72**, 172103 (2005).

[106] T.-P. Choy, D. Galanakis, and P. Phillips, Squaring the Triangle: Insulating Ground State of $Na_{0.5}CoO_2$. *cond-mat/0502164* (2005).

[107] D. J. Singh and D. Kasinathan, Destruction of the small Fermi surfaces in Na_xCoO_2 by Na disorder. *cond-mat/0604002* (2006).

[108] Z. Li, J. Yang, J. G. Hou, and Q. Zhu, Geometrical, electronic, and magnetic properties of $Na_{0.5}CoO_2$ from first principles. *Phys. Rev. B* **71**, 024502 (2005).

[109] Q. Huang, M. L. Foo, J. W. Lynn, H. W. Zandbergen, G. Lawes, Y. Wang, B. H. Toby, A. P. Ramirez, N. P. Ong, and R. J. Cava, Low temperature phase transitions and crystal structure of $Na_{0.5}CoO_2$. *J. Phys. Condens. Matter* **16**, 5803 (2004).

[110] J. Geck, M. v. Zimmermann, H. Berger, S.V. Borisenko, H. Eschrig, K. Koepernik, M. Knupfer, and B. Büchner, Stripe correlations in $Na_{0.75}CoO_2$. *cond-mat/0511554* (2005).

[111] M. L. Foo, R. E. Schaak, V. L. Miller, T. Klimczuk, N. S. Rogado, Y. Wang, G. C. Lau, C. Craley, H. W. Zandbergen, N. P. Ong, and R. J. Cava, Chemical instability of the cobalt oxyhydrate superconductor under ambient conditions. *Solid State Commun.* **127**, 33 (2003).

[112] D. C. Johnston and S. P. Frysinger, X-ray diffraction study of $Na_{1/3}(H_2O)_{1.5}TaS_2$: Observation of a Hendricks-Teller disordered layer lattice. *Phys. Rev. B* **30**, 980 (1984).

[113] D. C. Johnston, Observation of New Cointercalation Compounds in the System $Na_{0.33}(H_2O)_yTaS_2$ ($0 \leq y \leq 2$) from Power X-ray Diffraction Measurements. *J. Less-Common. Met.* **84**, 327 (1982).

[114] M. L. Foo, T. Klimczuk, L. Li, N. P. Ong, and R. J. Cava, Superconductivity in three-layer $Na_{0.3}CoO_2{\cdot}1.3H_2O$. *Solid State Commun.* **133**, 407 (2005).

[115] H. Watanabe, Y. Kobayashi, and M. Sato, ^{59}Co-NMR Knight Shift of Superconducting Three-Layer $Na_xCoO_2{\cdot}yH_2O$. *J. Phys. Soc. Jpn.* **74**, 2563 (2005).

[116] L. Viciu, J. W. G. Bos, H. W. Zandbergen, Q. Huang, M. L. Foo, S. Ishiwata, A.

P. Ramirez, M. Lee, N. P. Ong, and R. J. Cava, Crystal structure and elementary properties of Na_xCoO_2 (x=0.32, 0.51, 0.6, 0.75, and 0.92) in the three-layer $NaCoO_2$ family. *Phys. Rev. B* **73**, 174104 (2006).

[117] C. Delmas, C. Fouassier, and P. Hagenmuller, Structural Classification and Properties of the Layered Oxides. *Physca B* **99**, 81 (1980).

[118] K. Ishida, What are the key factors to control superconductivity in $Na_xCoO_2{\cdot}yH_2O$? *J. Phys. Soc. Jpn. Online-News and Comments*, Nov. 15 (2005).

[119] M. L. Foo, T. Klimczuk, and R. J. Cava, Hydration phase diagram for sodium cobalt oxide $Na_{0.3}CoO_2{\cdot}yH_2O$. *Mat. Res. Bull.* **40**, 665 (2005).

[120] V. V. Potavets, K. A. Lokshin, and M. Greenblatt, Isothermal section of the $Na_{0.3}CoO_2$–H_2O phase diagram at 22 °C from 11 to 100% relative humidity. *Solid State Sci.* **7**, 1312 (2005).

[121] H. Ohta, C. Michioka, Y. Itoh, and K. Yoshimura, Novel Phase Diagram of Superconductor $Na_xCoO_2{\cdot}yH_2O$ in 75% Relative Humidity. *J. Phys. Soc. Jpn.* **74**, 3147 (2005).

[122] H. Sakurai, K. Takada, R. Sasaki, and E. Takayama-Muromachi, Synthesis and superconductivity of $Na_xCoO_2{\cdot}yH_2O$. *Chin. J. Phys.* **43**, 566 (2005).

[123] K. Takada, H. Sakurai, E. Takayama-Muromachi, F. Izumi, R. A. Dilanian, and T. Sasaki, Stuctural difference between a superconducting sodium cobalt oxide and its related phase. *J. Solid State Chem.* **177**, 372 (2004).

[124] C. A. Marianetti, G. Kotliar, and G. Ceder, Role of Hybridization in Na_xCoO_2 and the Effect of Hydration. *Phys. Rev. Lett.* **92**, 196405 (2004).

[125] M. D. Johannes and D. J. Singh, Comparison of the electronic structures of hydrated and unhydrated Na_xCoO_2: The effect of H_2O. *Phys. Rev. B* **70**, 014507 (2004).

[126] R. Arita, Electronic structure of sodium cobalt oxide: Comparing mono- and bilayer hydrate. *Phys. Rev. B* **71**, 132503 (2005).

[127] C. H. Wang, X. H. Chen, J. L. Luo, G. T. Liu, X. X. Lu, H. T. Zhang, G. Y. Wang, X. G. Luo, and N. L. Wang, Dimensional crossover and anomalous magnetoresistivity of superconducting Na_xCoO_2 single crystals. *Phys. Rev. B* **71**, 224515 (2005).

[128] H. Sakurai, K. Takada, F. Izumi, R. A. Dilanian, T. Sasaki, and E. Takayama-Muromachi, The role of the water molecules in novel superconductor, $Na_{0.35}CoO_2{\cdot}1.3H_2O$. *Physica C* **412-414**, 182 (2004).

[129] Y. G. Shi, Y. L. Liu, H. X. Yang, C. J. Nie, R. Jin, and J. Q. Li, Raman spectroscopy study of Na_xCoO_2 and superconducting $Na_xCoO_2{\cdot}yH_2O$. *Phys. Rev. B* **70**, 052502 (2004).

[130] G.-q. Zheng, K. Matano, R.L. Meng, J. Cmaidalka, and C.W. Chu, Na Content dependence of superconductivity and the spin correlation in $Na_xCoO_2{\cdot}1.3H_2O$. *J. Phys.:Condens. Matter* **18**, L63 (2006).

[131] K. Matano, G.-q. Zheng, J. Cmaidalka, Y. Sun, R.L. Meng, and C.W. Chu, Evolution of the physical properties with Na content in the cobalt oxide superconductors $Na_xCoO_2{\cdot}1.3H_2O$. *Physica B* (in press, 2006).

[132] D. P. Chen, H. C. Chen, A. Maljuk, A. Kulakov, H. Zhang, P. Lemmens, and C. T. Lin, Single-crystal growth and investigation of Na_xCoO_2 and $Na_xCoO_2{\cdot}yH_2O$. *Phys. Rev. B* **70**, 024506 (2004).

[133] H. Sakurai, K. Takada, T. Sasaki, F. Izumi, R. A. Dilanian, and E. Takayama-Muromachi, Correlation between T_c and Lattice Parameters of Novel Superconducting Sodium Co Oxide Hydrate. *J. Phys. Soc. Jpn.***73**, 2590 (2004).

[134] P. W. Barnes, M. Avdeev, J. D. Jorgensen, D. G. Hinks, H. Claus, and S. Short, Superconductivity and cobalt oxidation state in metastable $Na_xCoO_{2-\delta}{\cdot}yH_2O$ ($x \approx 1/3$; $y \approx 4x$). *Phys. Rev. B* **72**, 134515 (2005).

[135] B. Liu, Y. Liang, and S. Feng, Kinetic energy driven superconductivity in the electron doped cobaltate $Na_xCoO_2{\cdot}yH_2O$. *Commun. Theor. Phys.* **43**, 1127 (2005).

[136] K. Takada, H. Sakurai, E. Takayama-Muromachi, F. Izumi, R. A. Dilanian, and T. Sasaki, Superconductivity of a hydrous sodium cobalt oxide. *Physica C* **408-410**, 165 (2004).

[137] K. Ishida, Y. Ihara, Y. Maeno, C. Michioka, M. Kato, K. Yoshimura, K. Takada, T. Sasaki, H. Sakurai, and E. Takayama-Muromachi, Unconventional Superconductivity and Nearly Ferromagnetic Spin Fluctuations in $Na_xCoO_2{\cdot}yH_2O$. *J. Phys. Soc. Jpn.* **72**, 3041 (2003).

[138] Y. Ihara, K. Ishida, C. Michioka1, M. Kato, K. Yoshimura, K. Takada, T. Sasaki, H. Sakurai, and E. Takayama-Muromachi, Correlation between Superconducting Transition Temperature T_c and Increase of Nuclear Spin-Lattice Relaxation Rate

Divided by Temperature $1/T_1T$ at T_c in the Hydrate Cobaltate $Na_xCoO_2{\cdot}yH_2O$. *J. Phys. Soc. Jpn.* **73**, 2069 (2004).

[139] Y. Ihara, K. Ishida, C. Michioka, M. Kato, K. Yoshimura, K. Takada, T. Sasaki, H. Sakurai, and E. Takayama-Muromachi, Weak Magnetic Order in Bilayered-Hydrate $Na_xCoO_2{\cdot}yH_2O$ Structure Probed by Co Nuclear Quadrupole Resonance – Proposed Phase Diagram in Superconducting $Na_xCoO_2{\cdot}yH_2O$ –. *J. Phys. Soc. Jpn.* **74**, 867 (2005).

[140] Y. Ihara, K. Ishida, H. Takeya, C. Michioka, M. Kato, Y. Itoh, K. Yoshimura, K. Takada, T. Sasaki, H. Sakurai, and E. Takayama-Muromachi, Anisotropic Behavior of Knight Shift in Superconducting State of $Na_xCoO_2{\cdot}yH_2O$. *J. Phys. Soc. Jpn.* **75**, 013708 (2006).

[141] H. Sakurai, K. Takada, T. Sasaki, and E. Takayama-Muromachi, Phase Diagram of Superconducting $Na_xCoO_2{\cdot}yH_2O$. *J. Phys. Soc. Jpn.***74**, 2909 (2005).

[142] F. C. Chou, J. H. Cho, and Y. S. Lee, Magnetic susceptibility study of hydrated and nonhydrated $Na_xCoO_2{\cdot}yH_2O$ single crystals. *Phys. Rev. B* **70**, 144526 (2004).

[143] W.B. Wu, D. J. Huang, J. Okamoto, H.-J. Lin, F. C. Chou, and C.T. Chen, Orbital symmetry and electron correlation in Na_xCoO_2. *Physica B* (in press, 2006).

[144] B. Lorenz, J. Cmaidalka, R. L. Meng, and C. W. Chu, Thermodynamic properties in the normal and superconducting states of $Na_xCoO_2{\cdot}yH_2O$ powder measured by heat capacity experiments. *Physica C* **402**, 106 (2004).

[145] H. D. Yang, J.-Y. Lin, C. P. Sun, Y. C. Kang, C. L. Huang, K. Takada, T. Sasaki,

H. Sakurai, and E. Takayama-Muromachi, Evidence of nodal superconductivity in $Na_{0.35}CoO_2{\cdot}1.3H_2O$: A specific-heat study. *Phys. Rev. B* **71**, 020504(R) (2005).

[146] C.P. Sun, J.-Y. Lin, Y.C. Kang, C.L. Huang, K. Takada, T. Sasaki, H. Sakurai, E. Takayama-Muromachi, and H.D. Yang, Various analyses of specific heat for the order parameter of superconductor $Na_{0.35}CoO_2{\cdot}1.3H_2O$. *Physica B* (in press, 2006).

[147] L. F. Matteiss, Band Structures of Transition-Metal-Dichalcogenide Layer Compounds, *Phys. Rev. B* **8**, 3719 (1973).

[148] A. Lerf and R. Schöllhorn, Solvation Reactions of Layered Ternary Sulfides A_xTiS_2, A_xNbS_2, and A_xTaS_2 . *Inorg. Chem.* **16**, 2950 (1977).

[149] D. C. Johnston and B. W. Keelan, Superconductivity and Mechanism of $M_x(H_2O)_yTaS_2$ Layered Cointercalation Compounds. *Solid State Commun.* **52**, 631 (1984).

[150] D. C. Johnston, Ambient Temperature Phase Relations in the System $Na_{1/3}(H_2O)_yTaS_2$ $(0 \leq y \leq 2)$. *Mat. Res. Bull.* **17**, 13 (1982).

[151] A. Chainani, T. Yokoya, Y. Takata, K. Tamasaku, M. Taguchi, T. Shimojima, N. Kamakura, K. Horiba, S. Tsuda, S. Shin, D. Miwa, Y. Nishino, T. Ishikawa, M. Yabashi, K. Kobayashi, H. Namatame, M. Taniguchi, K. Takada, T. Sasaki, H. Sakurai, and E. Takayama-Muromachi, Bulk electronic structure of $Na_{0.35}CoO_2{\cdot}1.3H_2O$. *Phys. Rev. B* **69**, 180508(R) (2004).

[152] H. Ohta, Y. Itoh, C. Michioka, and K. Yoshimura, ^{23}Na NMR Studies of Non-

superconducting and Superconducting $Na_{0.35}CoO_2{\cdot}1.3H_2O$ ($T_c < 1.8$ and ~ 4.5 K). cond-mat/0508197 (2005).

[153] Y. Ihara, K. Ishida, K. Yoshimura, K. Takada, T. Sasaki, H. Sakurai, and E. Takayama-Muromachi, ^{17}O NMR Measurements on Superconducting $Na_xCoO_2{\cdot}yH_2O$. *J. Phys. Soc. Jpn.* **74**, 2177 (2005).

[154] M. R. Norman, D. Pines, and C. Kallin, The pseudogap: friend or foe of high T_c ? *Adv. Phys.* **54**, 715 (2005).

[155] S. Y. Li, L. Taillefer, D. G. Hawthorn, M. A. Tanatar, J. Paglione, M. Sutherland, R. W. Hill, C. H. Wang, and X. H. Chen, Giant Electron-Electron Scattering in the Fermi-Liquid State of $Na_{0.7}CoO_2$. *Phys. Rev. Lett.* **93**, 056401 (2004).

[156] F. Rivadulla, M. Bañobre-Lòpez, M. García-Hernández, M. A. López-Quintela, and J. Rivas, Possible quantum criticality in Na_xCoO_2. *Phys. Rev. B* **73**, 054503 (2006).

[157] F.L. Ning, B.W. Statt, and F. C. Chou, Spin Dynamics in the Carrier-Doped $S{=}\frac{1}{2}$ Triangular Lattice of $Na_xCoO_2{\cdot}yH_2O$. *Phys. Rev. Lett.* **93**, 237201 (2004).

[158] T. Shimojima, T. Yokoya, T. Kiss, A. Chainani, S. Shin, T. Togashi, S. Watanabe, C. Zhang, C. T. Chen, K. Takada, T. Sasaki, H. Sakurai, and E. Takayama-Muromachi, Laser-excited ultrahigh-resolution photoemission spectroscopy of $Na_xCoO_2{\cdot}yH_2O$: Evidence for pseudogap formation. *Phys. Rev. B* **71**, 020505(R) (2005).

[159] P. Lemmens, K. Y. Choi, V. Gnezdilov, E. Ya. Sherman, D. P. Chen, C. T. Lin, F. C. Chou, and B. Keimer, Anomalous Electronic Raman Scattering in $Na_xCoO_2{\cdot}yH_2O$. *Phys. Rev. Lett.* **96**, 167204 (2006).

[160] T. Fujimoto, G.-q. Zheng, Y. Kitaoka, R. L. Meng, J. Cmaidalka, and C. W. Chu, Unconventional Superconductivity and Electron Correlations in the Cobalt Oxyhydrate $Na_{0.35}CoO_2{\cdot}yH_2O$ from Nuclear Quadrupole Resonance. *Phys. Rev. Lett.* **92**, 047004 (2004).

[161] N. Oeshler, R. A. Fishes, N. E. Phillips, J. E. Gordon, M. L. Foo, and R. J. Cava, Heat Capacity of $Na_{0.35}CoO_2{\cdot}1.3H_2O$, a New Two-Gap Superconductor: Comparison with the Heat Capacity of MgB_2. *Chin. J. Phys.* **43**, 574 (2005).

[162] I. I. Mazin and M. D. Johannes, A critical assessment of the superconducting pairing symmetry in $Na_xCoO_2{\cdot}yH_2O$. *Nature Phys.* **1**, 91 (2005).

[163] T. Sasaki, P. Badica, N. Yoneyama, K. Yamada, K. Togano, and N. Kobayashi, Superconducting Properties under Magnetic Field in $Na_{0.35}CoO_2{\cdot}1.3H_2O$ Single Crystal. *J. Phys. Soc. Jpn.* **73**, 1131 (2004).

[164] Y. Kobayashi, H. Watanabe, M. Yokoi, T. Moyoshi, Y. Mori, and M. Sato, ^{59}Co-NMR Knight Shift of Aligned Crystals and Polycrystalline Samples of Superconducting $Na_{0.35}CoO_2{\cdot}1.3H_2O$. *J. Phys. Soc. Jpn.* **74**, 1800 (2005).

[165] C. Michioka, M. Kato, K. Yoshimura, K. Takada, H. Sakurai, E. Takayama-Muromachi, and T. Sasaki, Determination of Spin Contributed Knight Shift of ^{59}Co-NMR in $Na_{0.35}CoO_2{\cdot}1.3H_2O$. *cond-mat/0403293* (2004).

[166] M. M. Maśka, M. Mierzejewski, B. Andrzejewski, M. L. Foo, R. J. Cava, and T. Klimczuk, Possible singlet-to-triplet pairing transition in $Na_xCoO_2{\cdot}yH_2O$. *Phys. Rev. B* **70**, 144516 (2004).

[167] K. Kuroki, Y. Tanaka, and R. Arita, Competition between singlet and triplet pairings in $Na_xCoO_2{\cdot}yH_2O$. *Phys. Rev. B* **71**, 024506 (2005).

[168] G.-q. Zheng, K. Matano, D. P. Chen, and C. T. Lin, Spin singlet pairing in the superconducting state of $Na_xCoO_2{\cdot}1.3H_2O$: Evidence from a ^{59}Co Knight shift in a single crystal. *Phys. Rev. B* **73**, 180503(R) (2006).

[169] W. Higemoto, K. Ohishi, A. Koda, S. R. Saha, R. Kadono, K. Ishida, K. Takada, H. Sakurai, E. Takayama-Muromachi, and T. Sasaki, Possible unconventional superconductivity in $Na_xCoO_2{\cdot}yH_2O$ probed by muon spin rotation and relaxation. *Phys. Rev. B* **70**, 134508 (2004).

[170] M. D. Johannes, I. I. Mazin, D. J. Singh, and D. A. Papaconstantopoulos, Nesting, Spin Fluctuations, and Odd-Gap Superconductivity in $Na_xCoO_2{\cdot}yH_2O$. *Phys. Rev. Lett.* **93**, 097005 (2004).

[171] K. Kuroki, Y. Tanaka, and R. Arita, Possible Spin-Triplet f-Wave Pairing Due to Disconnected Fermi Surfaces In $Na_xCoO_2{\cdot}yH_2O$. *Phys. Rev. Lett.* **93**, 077001 (2004).

[172] Y. Yanase, M. Mochizuki, and M. Ogata, Role of Spin-Orbit Coupling on the Spin Triplet Pairing in $Na_xCoO_2{\cdot}yH_2O$: I. d-Vector under Zero Mangetic Field. *J. Phys. Soc. Jpn.* **74**, 2568 (2005).

[173] M. Mochizuki, Y. Yanase, and M. Ogata, Ferromagnetic Fluctuation and Possible Triplet Superconductivity in $Na_xCoO_2{\cdot}yH_2O$: Fluctuation-Exchange Study of the Multiorbital Hubbard Model. *Phys. Rev. Lett.* **94**, 147005 (2005).

[174] M. Z. Hasan, Y.-D. Chuang, D. Qian, Y. W. Li, Y. Kong, A. Kuprin, A. V. Fedorov,

R. Kimmerling, E. Rotenberg, K. Rossnagel, Z. Hussain, H. Koh, N. S. Rogado, M. L. Foo, and R. J. Cava, Fermi Surface and Quasiparticle Dynamics of $Na_{0.7}CoO_2$ Investigated by Angle-Resolved Photoemission Spectroscopy. *Phys. Rev. Lett.* **92**, 246402 (2004).

[175] H.-B. Yang, S.-C. Wang, A. K. P. Sekharan, H. Matsui, S. Souma, T. Sato, T. Takahashi, T. Takeuchi, J. C. Campuzano, R. Jin, B. C. Sales, D. Mandrus, Z. Wang, and H. Ding, ARPES on $Na_{0.6}CoO_2$: Fermi Surface and Unusual Band Dispersion. *Phys. Rev. Lett.* **92**, 246403 (2004).

[176] H.-B. Yang, Z.-H. Pan, A. K. P. Sekharan, T. Sato, S. Souma, T. Takahashi, R. Jin, B. C. Sales, D. Mandrus, Z. Wang, and H. Ding, Fermi Surface Evolution and Luttinger Theorem in Na_xCoO_2: A Systematic Photoemission Study. *Phys. Rev. Lett.* **95**, 146401 (2005).

[177] M.Z. Hasan, D. Qian, Y. Li, A.V. Fedorov, Y.-D. Chuang, A.P. Kuprin, M.L. Foo, and R.J. Cava, Nature of Correlated Motion of Electrons in the Parent Cobaltate Superconductors. *cond-mat/0501530* (2005).

[178] K. Kuroki, S. Onari, Y. Tanaka, R. Arita, and T. Nojima, Extended s-wave pairing originating from the a_{1g} band in $Na_xCoO_2{\cdot}yH_2O$: Single-band U-V model with fluctuation exchange method. *Phys. Rev. B* **73**, 184503 (2006).

[179] P. Zhang, W. Luo, M. L. Cohen, and S. G. Louie, Fermi Surface of Na_xCoO_2. *Phys. Rev. Lett.* **93**, 236402 (2004).

[180] K. Yada and H. Kontani, Origin of Weak Pseudogap Behaviors in $Na_{0.35}CoO_2$: Absence of Small Hole Pockets, *J. Phys. Soc. Jpn.* **74**, 2161 (2005).

[181] K. Yada and H. Kontani, Spin fluctuations and weak pseudogap behaviors in $Na_{0.35}CoO_2$: renormalization of band structure. *cond-mat/0507066* (2005).

[182] S. Zhou, M. Gao, H. Ding, P. A. Lee, and Z. Wang, Electron Correlation and Fermi Surface Topology of Na_xCoO_2. *Phys. Rev. Lett.* **94**, 206401 (2005).

[183] H. Ishida, M. D. Johannes, and A. Liebsch, Effect of Dynamical Coulomb Correlations on the Fermi Surface of $Na_{0.3}CoO_2$. *Phys. Rev. Lett.* **94**, 196401 (2005).

[184] B. Pedrini, J. L. Gavilano, S. Weyeneth, E. Felder, J. Hinderer, M. Weller, H. R. Ott, S. M. Kazakov, and J. Karpinski, Magnetic phase transition at 88 K in $Na_{0.5}CoO_2$ revealed by ^{23}Na NMR investigations. *Phys. Rev. B* **72**, 214407 (2005).

[185] J. Hwang, J. Yang, T. Timusk, and F. C. Chou, Infrared conductivity of Na_xCoO_2: Evidence of gapped states. *Phys. Rev. B* **72**, 024549 (2005).

[186] S. Lupi, M. Ortolani, L. Baldassarre, P. Calvani, D. Prabhakaran and A. T. Boothroyd, Optical conductivity and charge ordering in Na_xCoO_2. *Phys. Rev. B* **72**, 024550 (2005).

[187] L. Balicas, M. Abdel-Jawad, N. E. Hussey, F. C. Chou, and P. A. Lee, Shubnikov-de Haas Oscillations and the Magnetic-Field-Induced Suppression of the Charge Ordered State in $Na_{0.5}CoO_2$. *Phys. Rev. Lett.* **94**, 236402 (2005).

[188] H. W. Zandbergen, M. Foo, Q. Xu, V. Kumar, and R. J. Cava, Sodium ion ordering in Na_xCoO_2: Electron diffraction study. *Phys. Rev. B* **70**, R024101 (2004).

[189] H.X. Yang, C.J. Nie, Y.G. Shi, H.C. Yu, S. Ding, Y.L. Liu, D. Wu, N.L. Wang and J.Q. Li, Structural phase transitions and sodium ordering in $Na_{0.5}CoO_2$: a combined electron diffraction and Raman spectroscopy study. *Solid State Commun.* **134**, 403 (2005).

[190] A. J. Williams, J. P. Attfield, M. L. Foo, L. Viciu, and R. J. Cava, High-resolution neutron diffraction study of possible charge ordering in $Na_{0.5}CoO_2$. *Phys. Rev. B* **73**, 134401 (2006).

[191] P. Mendels, D. Bono, J. Bobroff, G. Collin, D. Colson, N. Blanchard, H. Alloul, I. Mukhamedshin, F. Bert, A. Amato, and A. D. Hillier, Cascade of Bulk Magnetic Phase Transitions in Na_xCoO_2 as Studied by Muon Spin Rotation. *Phys. Rev. Lett.* **94**, 136403 (2005).

[192] C. Bernhard, A. V. Boris, N. N. Kovaleva, G. Khaliullin, A. V. Pimenov, L. Yu, D. P. Chen, C. T. Lin, and B. Keimer, Charge Ordering and Magnetopolarons in $Na_{0.82}CoO_2$. *Phys. Rev. Lett.* **93**, 167003 (2004).

[193] S. P. Bayrakci, I. Mirebeau, P. Bourges, Y. Sidis, M. Enderle, J. Mesot, D. P. Chen, C. T. Lin, and B. Keimer, Magnetic Ordering and Spin Waves in $Na_{0.82}CoO_2$. *Phys. Rev. Lett.* **94**, 157205 (2005).

[194] L. M. Helme, A. T. Boothroyd, R. Coldea, D. Prabhakaran, D. A. Tennant, A. Hiess, and J. Kulda, Three-Dimensional Spin Fluctuations in $Na_{0.75}CoO_2$. *Phys. Rev. Lett.* **94**, 157206 (2005).

[195] L. M. Helme, A. T. Boothroyd, R. Coldea, D. Prabhakaran, A. Stunault, G. J.

McIntyre, and N. Kernavanois, Spin gaps and magnetic structure of Na_xCoO_2. *Phys. Rev. B* **73**, 054405 (2006).

[196] J. Sugiyama, J. H. Brewer, E. J. Ansaldo, B. Hitti, M. Mikami, Y. Mori, and T. Sasaki, Electron correlation in the two-dimensional triangular lattice of Na_xCoO_2 with $x > 0.6$. *Physica B* **359-361**, 1345 (2005).

[197] N. L. Wang, P. Zheng, D. Wu, Y. C. Ma, T. Xiang, R. Y. Jin, and D. Mandrus, Infrared Probe of the Electronic Structure and Charge Dynamics of $Na_{0.7}CoO_2$. *Phys. Rev. Lett.* **93**, 237007 (2004).

[198] Y. Ihara, K. Ishida, C. Michioka, M. Kato, K. Yoshimura, H. Sakurai, and E. Takayama-Muromachi, Magnetic Fluctuations in the Metallic State of $Na_{0.7}CoO_2$ Revealed by ^{23}Na Nuclear Magnetic Resonance. *J. Phys. Soc. Jpn.* **73**, 2963 (2004).

[199] G. Caimi, L. Degiorgi, H. Berger, N. Barisic, L. Forrò, and F. Bussy, Optical evidence for the proximity to a spin-density-wave metallic state in $Na_{0.7}CoO_2$. *Eur. Phys. J. B* **40**, 231 (2004).

[200] J. Wooldridge, D. M^{c}K Paul, G. Balakrishnan, and M. R. Lees, Investigation of the spin density wave in Na_xCoO_2. *J. Phys.: Condens. Matter* **17**, 707 (2005).

[201] J. L. Luo, N. L. Wang, G. T. Liu, D. Wu, X. N. Jing, F. Hu, and T. Xiang, Metamagnetic Transition in $Na_{0.85}CoO_2$ Single Crystals. *Phys. Rev. Lett.* **93**, 187203 (2004).

[202] H. Rosner, S.-L. Dreschler, F. Fuchs, A. Handstein, A. Walte, and K.-H.

Muller, Electronic structure and aspects of unconventional superconductivity in $Na_xCoO_2{\cdot}yH_2O$. *Braz. J. Phys.* **33**, 718 (2003).

[203] D. J. Singh, Quantum critical behavior and possible triplet superconductivity in electron-doped CoO_2 sheets. *Phys. Rev. B* **68**, R20503 (2003).

[204] I. I. Mazin, D. J. Singh, and A. Aguayo, Density Functional Calculations near Ferromagnetic Quantum Critical points. in *Proceedings of the NATO ARW on Physics of Spin in Solids: Materials, Methods, and Applications*, edited by S. Halilov (Kluwer, New York, 2004); *cond-mat/0401563.*

[205] M. Mochizuki, Y. Yanase, and M. Ogata, Ferromagnetic and Triplet-Pairing Instabilities Controlled by Trigonal Distortion of CoO_6 Octahedra in $Na_xCoO_2{\cdot}yH_2O$. *J. Phys. Soc. Jpn.* **74**, 1670 (2005).

[206] V. I. Anisimov, I. S. Elfimov, N. Hamada, and K. Terakura, Charge-ordered insulating state of Fe_3O_4 from first-principles electronic structure calculations. *Phys. Rev. B* **54**, 4387 (1996).

[207] S. Yamamoto and T. Fujiwara, Spin-Glass-like Transition and Hall Resistivity of $Y_{2-x}Bi_xIr_2O_7$. *J. Phys. Soc. Jpn.* **71**, 1226 (2002).

[208] Z. Szotek, W. M. Temmerman, A. Svane, L. Petit, G. M. Stocks, and H. Winter, *Ab initio* study of charge order in Fe_3O_4. *Phys. Rev. B* **68**, 054415 (2003).

[209] L.-J. Zou, J.-L. Wang, and Z. Zeng, Electronic structure and states in two-dimensional triangular cobalt oxides: The role of electronic correlation. *Phys. Rev. B* **69**, 132505 (2004).

[210] A. Liebsch, Mott Transitions in Multiorbital Systems. *Phys. Rev. Lett.* **91**, 226401 (2003).

[211] A. Koga, N. Kawakami, T. M. Rice, and M. Sigrist, Orbital-Selective Mott Transitions in the Degenerate Hubbard Model. *Phys. Rev. Lett.* **92**, 216402 (2004).

[212] Y. Tanaka, Y. Yanase, and M. Ogata, Superconductivity in $Na_xCoO_2{\cdot}yH_2O$ due to Charge Fluctuation. *J. Phys. Soc. Jpn.* **73**, 319 (2004).

[213] Y. Nisikawa, H. Ikeda, and K. Yamada, Possible Pairing Symmetry of Superconductor $Na_xCoO_2{\cdot}yH_2O$. *J. Phys. Soc. Jpn.* **73**, 1127 (2004).

[214] G. G. Amatucci, M. M. Tarascon, and L. C. Klein, CoO_2, The End Member of the Li_xCoO_2 Solid Solution. *J. Electrochem. Soc.* **143**, 1114 (1996).

[215] J. M. Tarascon, G. Vaughan, Y. Chabre, L. Seguin, M. Anne, P. Strobel, and G. Amatucci, In Situ Structural and Electrochemical Study of $Ni_{1-x}Co_xO_2$ Metastable Oxides Prepared by Soft Chemistry. *J. Solid State Chem.* **147**, 410 (1999).

[216] X. Q. Yang, X. Sun, and J. McBreen, New phase and phase transitions observed in $Li_{1-x}CoO_2$ during charage: in situ synchrotron X-ray diffraction studies. *Electrochem. Commun.* **2**, 100 (2000).

[217] S. Venkatraman and A. Manthiram, Synthesis and Characterization of P3-Typer $CoO_{2-\delta}$. *Chem. Mater.* **14**, 3907 (2002).

[218] M. D. Johannes, D. A. Papaconstantopoulos, D. J. Singh, and M. J. Mehl, A tight-binding investigation of the Na_xCoO_2 Fermi surface. *Europhys. Lett.* **68**, 433 (2004).

[219] For recent review, see P. Larson, I. I. Mazin, and D. J. Singh, Magnetism, critical fluctuations, and susceptibility renormalization in Pd. *Phys. Rev. B* **69**, 064429 (2004).

[220] T. Mizokawa, Orbital polarization in layered t_{2g} electron systems. *New J. Phys.* **6**, 169 (2004).

[221] Y. G. Shi, H. X. Yang, H. Huang, X. Liu, and J. Q. Li, Superconductivity, charge ordering, and structural properties of α- and β-$Na_xCoO_2 \cdot y(H_2O,D_2O)$. *Phys. Rev. B* **73**, 094505 (2006).

[222] O. Gunnarsson, E. Koch, and R. M. Martin, Mott transition in degenerate Hubbard models: Application to doped fullerenes. *Phys. Rev. B* **54**, R11026 (1996).

[223] O. Gunnarsson, E. Koch, and R. M. Martin, Mott-Hubbard insulators for systems with orbital degeneracy. *Phys. Rev. B* **56**, 1146 (1997).

[224] E. Koch, O. Gunnarsson, and R. M. Martin, Metal-insulator transitions in generalized Hubbard models. *Comput. Phys. Commun.* **127**, 137 (2000).

[225] J. B. Goodenough and P. M. Raccah, Complex vs Band Formation in Perovskite Oxides. *J. Appl. Phys.* **36**, 1031 (1965).

[226] K. Sreedhar, J. M. Honig, M. Darwin, M. McElfresh, P. M. Shand, J. Xu, B. C. Crooker, and J. Spalek, Electronic properties of the metallic perovskite $LaNiO_3$: Correlated behavior of $3d$ electrons. *Phys. Rev. B* **46**, 6382 (1992).

[227] N. Gayathri, A. K. Raychaudhuri, X. Q. Xu, J. L. Peng, and R. L. Greene, Electronic

conduction in $LaNiO_{3-\delta}$: the dependence on the oxygen stoichiometry δ. *J. Phys.: Condens. Matt.* **10**, 1323 (1998).

[228] T. Moriga, O. Usaka, I. Nakabayashi, T. Kinouchi, S. Kikkawa, and F. Kanamaru, Characterization of oxygen-deficient phases appearing in reduction of the perovskite-type $LaNiO_3$ to $La_2Ni_2O_5$. *Solid State Ionics* **79**, 252 (1995).

[229] Y. Okajima, K. Kohn and K. Siratori, Magnetic relaxation and possible ferromagnetic clusters in defect perovskite $LaNiO_{2.70}$. *J. Mag. Mag. Mat.* **140-144**, 2149 (1995).

[230] J. A. Alonso, M. J. Martínez-Lope, J. L. García-Muñoz, and M. T. Fernández-Díaz, A structural and magnetic study of the defect perovskite $LaNiO_{2.5}$ from high-resolution neutron diffraction data. *J. Phys.: Condens. Matt.* **9**, 6417 (1997).

[231] M. Crespin, P. Levitz, and L. Gatineau, Reduced forms of lanthanum nickel trioxide perovskite. Part1. Evidence for new phases: dilanthanum dinickel pentoxide and lanthanum nickel dioxide. *J. Chem. Soc., Faraday Trans. 2* **79**, 1181 (1983).

[232] P. Levitz, M. Crespin, and L. Gatineau, Reduced forms of lanthanum nickel trioxide perovskite. Part2. X-ray structure of lanthanum nickel dioxide and extended x-ray absorption fine structure study:local environment of monovalent nickel. *J. Chem. Soc., Faraday Trans. 2* **79**, 1195 (1983).

[233] J. Choisnet, R. A. Evarestov, I. I. Tupitsyn, and V. A. Veryazov, Investigation of the chemical bonding in nickel mixed oxides from electronic structure calculations. *J. Phys. Chem. Solids* **57**, 1839 (1996).

[234] V. I. Anisimov, D. Bukhvalov, and T. M. Rice, Electronic structure of possible nickelate analogs to the cuprates. *Phys. Rev. B* **59**, 7901 (1999).

[235] M. J. Martínez-Lope, M. T. Casais, and J. A. Alonso, Stabilization of Ni^{+} in defect perovskites $La(Ni_{1-x}Al_x)O_{2+x}$ with 'infinite-layer' structure. *J. Alloys Comp.* **275-277**, 109 (1998).

[236] T. Siegrist, S. M. Zahurak, D. W. Murphy, and R. S. Roth, The parent structure of the layered high-temperature superconductors. *Nature* **334**, 231 (1988).

[237] M. A. Hayward, M. A. Green, M. J. Rosseinsky, and J. Sloan, Sodium Hydride as a Powerful Reducing Agent for Topotactic Oxide Deintercalation: Synthesis and Characterization of the Nickel(I) Oxide $LaNiO_2$. *J. Am. Chem. Soc.* **121**, 8843 (1999).

[238] M. A. Hayward and M. J. Rosseinsky, Synthesis of the infinite layer Ni(I) phase $NdNiO_{2+x}$ by low temperature reduction of $NdNiO_3$ with sodium hydride. *Solid State Sci.* **5**, 839 (2003).

[239] T. Moriya, *Spin Fluctuations in Itinerant Electron Magnetism* (Berlin, Springer, 1985).

[240] A. Aguayo, I. I. Mazin, and D. J. Singh, Why Ni_3Al Is an Itinerant Ferromagnet but Ni_3Ga Is Not. *Phys. Rev. Lett.* **92**, 147201 (2004).

[241] A. B. Shick, W. E. Pickett, and A. I. Liechtenstein, Ground and Metastable States in γ-Ce from Correlated Band Theory. *J. Electron Spectrosc. Relat. Phenom.* **114-116**, 753 (2001).

[242] A. B. Shick, V. Janis, V. Drchal, and W. E. Pickett, Spin and orbital magnetic state of UGe_2 under pressure. *Phys. Rev. B* **70**, 134506 (2004).

[243] D. J. Singh and I. I. Mazin, Spin fluctuations and the magnetic phase diagram of $ZrZn_2$. *Phys. Rev. B* **69**, 020402 (2004).

[244] A. Aguayo and D. J. Singh, Itinerant ferromagnetism and quantum criticality in Sc_3In. *Phys. Rev. B* **66**, 020401 (2002).

[245] A. Van der Ven, M. K. Aydinol, G. Ceder, G. Kresse, and J. Hafner, First-principles investigation of phase stability in Li_xCoO_2. *Phys. Rev. B* **58**, 2975 (1998).

[246] T. Matsurra, J. Tabuchi, J. Mizusaki, S. Yamauchi, and K. Fueki, Electrical Properties of $La_{2-x}Sr_xCoO_4$–I: Structure, Electrical Conductivity, and Seebeck coefficient of Single Crystals (x=0.0, 0.5, 1.0 and 1.5). *J. Phys. Chem. Solids* **49**, 1403 (1988).

[247] Y. Furukawa, S. Wada, and Y. Yamada, Phase Transition from Antiferromagnetic Insulator to Ferromagnetic Metal in $La_{2-x}Sr_xCoO_4$ – Magnetization and NMR Studies –. *J. Phys. Soc. Jpn.* **62**, 1127 (1993).

[248] Y. Moritomo, K. Higashi, K. Matsuda, and A. Nakamura, Spin-state transition in layered perovskite cobalt oxides: $La_{2-x}Sr_xCoO_4$ ($0.4 \leq x \leq 1.0$). *Phys. Rev. B* **55**, R14725 (1997).

[249] J. Wang, W. Zhang, and D. Y. Xing, Magnetic structure of the layered perovskite $LaSrCoO_4$. *Phys. Rev. B* **62**, 14140 (2000).

[250] M. Sanchez-Andujar, B. Rivas-Murias, D. Rinaldi, R. Caciuffo, J. Mira, R. Ri-

vas, and M. A. Senaris-Rodriguez, Magnetic order in the lamellar compounds $La_{1-x}Sr_{1+x}CoO_4$ ($0 \leq x \leq 0.4$). *J. Magn. Magn. Mat.* **272-276**, 855 (2004).

[251] G. Demazeau, P. Courbin, G. L. Flem, M. Pouchard, P. Hagenmuller, J. L. Soubeyroux, I. G. Main, and G. A. Robins, Structural and magnetic properties of cobalt lanthanum strontium oxide: a discussion of the electronic structure of trivalent cobalt. *Nouv. J. Chim.* **3**, 171 (1979).

[252] Y.Y. Liu, X.M. Chen, and X.Q. Liu, Magnetic properties and magnetoresistance of polycrystalline $SrLaCoO_4$. *Solid State Commun.* **136**, 576 (2005).

[253] C. N. R. Rao, P. Ganguly, K. K. Singh, and R. A. Mohan Ram, A comparative study of the magnetic and electrical properties of perovskite oxides and the corresponding two-dimensional oxides of K_2NiF_4 structure. *J. Solid State Chem.* **72**, 14 (1988).

[254] K. Yamada, M. Matsuda, Y. Endoh, B. Keimer, R. J. Birgeneau, S. Onodera, J. Mizusaki, T. Matsuura, and G. Shirane, Successive antiferromagnetic phase transitions in single-crystal La_2CoO_4. *Phys. Rev. B* **39**, 2336 (1989).

[255] J. Matsuno, Y. Okimoto, Z. Fang, X. Z. Yu, Y. Matsui, N. Nagaosa, M. Kawasaki, and Y. Tokura, Metallic Ferromagnet with Square-Lattice CoO_2 Sheets. *Phys. Rev. Lett.* **93**, 167202 (2004).

[256] J. Matsuno, Y. Okimoto, Z. Fang, X. Z. Yu, Y. Matsui, N. Nagaosa, H. Kumigashira, M. Oshina, M. Kawasaki, and Y. Tokura, Novel metallic ferromagnet Sr_2CoO_4. *Thin Solid Films* **486**, 113 (2005).

[257] X. L. Wang and E. Takayama-Muromachi, Magnetic and transport properties of

the layered perovskite system $Sr_{2-y}Y_yCoO_4$ ($0 \leq y \leq 1$). *Phys. Rev. B* **72**, 064401 (2005).

[258] X. L. Wang, H. Sakurai, and E. Takayama-Muromachi, Synthesis, structures, and magnetic properties of novel Roddlesden– Popper homologous series $Sr_{n+1}Co_nO_{3n+1}$ (n=1,2,3,4, and ∞). *J. Appl. Phys.* **97**, 10M519 (2005).

[259] T. Tekeda, T. Watanabe, S. Komura, and H. Fujii, Magnetic Properties of $SrFe_{1-x}Co_xO_3$. *J. Phys. Soc. Jpn.* **56**, 731 (1987).

[260] S. Mathi Jaya, R. Jagadish, R. S. Rao, and R. Asokamani, Electronic structure and magnetism of $SrFeO_3$ and $SrCoO_3$. *Phys. Rev. B* **43**, 13274 (1991).

[261] R. H. Potze, G. A. Sawatzky, and M. Abbate, Possibility for an intermediate-spin ground state in the charge-transfer material $SrCoO_3$. *Phys. Rev. B* **51**, 11501 (1995).

[262] M. A. Korotin, S. Yu. Ezhov, I. V. Solovyev, V. I. Anisimov, D. I. Khomskii, and G. A. Sawatzky, Intermediate-spin state and properties of $LaCoO_3$. *Phys. Rev. B* **54**, 5309 (1996).

[263] H. Takahashi, F. Munakata, and M. Yamanaka, *Ab initio* study of the electronic structures in $LaCoO_3$–$SrCoO_3$ systems. *Phys. Rev. B* **57**, 15211 (1998).

[264] I. A. Nekrasov, S. V. Streltsov, M. A. Korotin, and V. I. Anisimov, Influence of rare-earth ion radii on the low-spin to intermediate-spin state transition in lanthanide cobaltite perovskites: $LaCoO_3$ versus $HoCoO_3$. *Phys. Rev. B* **68**, 235113 (2003).

[265] G. Maris, Y. Ren, V. Volotchaev, C. Zobel, T. Lorenz, and T. T. M. Palstra, Evidence for orbital ordering in $LaCoO_3$. *Phys. Rev. B* **67**, 224423 (2003).

[266] D. Phelan, Despina Louca, S. Rosenkranz, S.-H. Lee, Y. Qiu, P. J. Chupas, R. Osborn, H. Zheng, J. F. Mitchell, J. R. D. Copley, J. L. Sarrao, and Y. Moritomo, Nanomagnetic Droplets and Implications to Orbital Ordering in $La_{1-x}Sr_xCoO_3$. *Phys. Rev. Lett.* 96, 027201 (2006).

[267] L. F. Mattheiss, Electronic band properties and superconductivity in $La_{2-y}X_yCuO$. *Phys. Rev. Lett.* **58**, 1028 (1987).

[268] For review, see W. E. Pickett, Electronic structure of the high-temperature oxide superconductors. *Rev. Mod. Phys.* **61**, 433 (1989).

[269] R. Weht and W. E. Pickett, Extended Moment Formation and Second Neighbor Coupling in Li_2CuO_2. *Phys. Rev. Lett.* **81**, 2502 (1998).

[270] K.-W. Lee and W. E. Pickett, Infinite-layer $LaNiO_2$: Ni^{1+} is not Cu^{2+}. *Phys. Rev. B* **70**, 165109 (2004).

Appendix A

Stoner Instability[1]

Rigorous Derivation

In the subsection, we will derive mathematically the Stoner condition. According to the Hartree-Fock approximation, the exchange interaction between electrons $\mathcal{H}_{CF}$ is given by

$$\mathcal{H}_{CF} \approx -\sum_{\vec{l},\vec{\kappa},\sigma}{}' v(\vec{\kappa}) f(\varepsilon_{\vec{l}+\vec{\kappa},\sigma}) a^{+}_{\vec{l},\sigma} a_{\vec{l},\sigma}, \tag{A.1}$$

where the Fermi-Dirac function $f(\varepsilon_{\vec{l}+\vec{\kappa},\sigma}) \equiv < a^{+}_{\vec{l}+\vec{\kappa},\sigma} a_{\vec{l}+\vec{\kappa},\sigma} >$ and $\sum'$ means a summation for $\vec{\kappa} \neq 0$. $\varepsilon_{\vec{l}+\vec{\kappa},\sigma}$ is an energy with wave vector $\vec{l}+\vec{\kappa}$ and spin σ. Using a plane waver basis set, the Fourier component of the Coulomb interaction $v(\vec{\kappa})$ is given by $\frac{1}{V}\frac{4\pi e^2}{\kappa^2}$ (V is the normalization volume). a^{+} and a are the creation and annihilation operators for an electron, respectively. However, it is little meaningful to solve Eq. (A.1) exactly. So an

[1] E. C. Stoner, Ferromagnetism. *Rep. Prog. Phys.* **11**, 43 (1947).

approximation is used as

$$\mathcal{H}_{CF} \approx -I \sum_{\vec{l},\vec{\kappa},\sigma} f(\varepsilon_{\vec{l}+\vec{\kappa},\sigma}) a^{+}_{\vec{l},\sigma} a_{\vec{l},\sigma} \tag{A.2}$$

$$\approx \sum_{\vec{l},\sigma} (-I n_\sigma) a^{+}_{\vec{l},\sigma} a_{\vec{l},\sigma}, \tag{A.3}$$

where the number of electrons with spin σ n_σ is $\sum_{\vec{l}} f(\varepsilon_{\vec{l},\sigma})$. Here the mean value theorem of integration to obtain Eq. (A.3) was also used. The effective exchange interaction strength I is the size of the exchange potential produced by the other electrons in a medium with $\vec{\kappa} = 0$. Thus, under the Coulomb interaction and external magnetic field, the total Hamiltonian of an electron is written as

$$\begin{aligned} \mathcal{H} &= \mathcal{H}_0 + \mathcal{H}_{CF} + \mathcal{H}' \\ &= \sum_{\vec{k},\sigma} (\varepsilon_{\vec{k}} - I n_\sigma + \sigma \mu_B H) a^{+}_{\vec{k},\sigma} a_{\vec{k},\sigma} \\ &= \sum_{\vec{k},\sigma} \varepsilon_{\vec{k},\sigma} a^{+}_{\vec{k},\sigma} a_{\vec{k},\sigma}. \end{aligned} \tag{A.4}$$

The total energy of an electron $\varepsilon_{\vec{k},\sigma}$ is

$$\begin{aligned} \varepsilon_{\vec{k},\sigma} &= \varepsilon_{\vec{k}} - I n_\sigma + \sigma \mu_B H \\ &= \varepsilon_{\vec{k}} + \sigma [\mu_B H - \frac{I}{2}(n_+ - n_-)] - \frac{I}{2}(n_+ + n_-). \end{aligned} \tag{A.5}$$

Since the total electron number $n = \sum_\sigma n_\sigma$ is constant, the last term can be neglected. Rewriting the above equation,

$$\begin{aligned} \varepsilon_{\vec{k},\sigma} &= \varepsilon_{\vec{k}} + \sigma [\mu_B H - \frac{I}{2}(n_+ - n_-)] \\ &\equiv \varepsilon_{\vec{k}} + \sigma \mu_B H_{eff}. \end{aligned} \tag{A.6}$$

Here, the effective magnetic field H_{eff} is written as

$$\begin{aligned} H_{eff} &= H - \frac{I}{2}(n_+ - n_-) \\ &= H[1 - \frac{I}{2H\mu_B}(n_+ - n_-)] \\ &= H[1 + \frac{I}{2\mu_B^2}\chi_S]. \end{aligned} \tag{A.7}$$

In the last line, the definition of susceptibility $\chi = -\frac{\mu_B(n_+ - n_-)}{H}(H \to 0)$ is used. Recalling the magnetization $< M_z >$ is given by $< M_z >= \chi_p H_{eff} = \chi_s H$, the Stoner susceptibility χ_s is

$$\chi_s = \frac{\chi_p}{1 - \frac{1}{2\mu_B^2} I\chi_p}. \tag{A.8}$$

Recalling the Pauli susceptibility χ_p is included only the Zeeman energy by external magnetic field, the Stoner susceptibility χ_s is enhanced due to the electron-electron interaction described by the exchange interaction I in a metal. At T=0, since $\chi_p = 2\mu_B^2 N(0)$, the Stoner susceptibility χ_s is

$$\chi_s = \frac{2\mu_B^2 N(0)}{1 - IN(0)}, \tag{A.9}$$

where $N(0)$ is the single spin DOS at the Fermi level. Equation (A.9) shows that χ_s becomes infinity at $IN(0)$=1, leading to ferromagnetic transition. As a result, when $IN(0) \geq 1$, a ferromagnetic state is stable. This criterion is called the Stoner condition. The condition indicates that the appearance of ferromagnetism is favorable if DOS has a sharp peak near E_F.

Conceptual Understanding

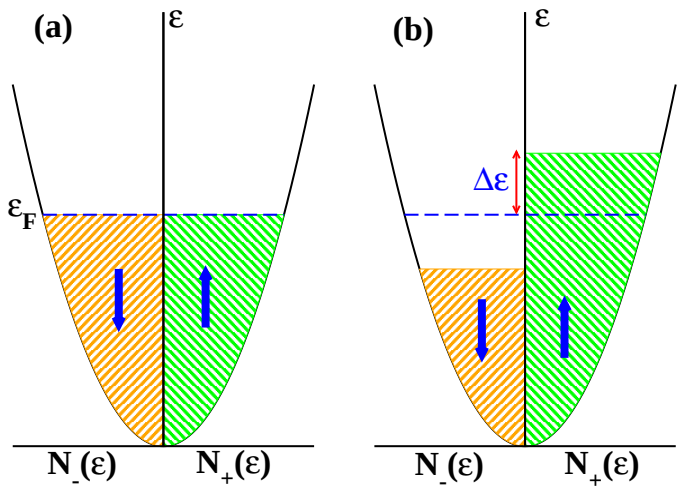

Figure A.1. Schematic DOS for (a) nonmagnetic and (b) ferromagnetic states.

In this subsection, we will derive the Stoner condition through simple physical consideration. The difference of total energy between nonmagnetic (E_a) and ferromagnetic (E_b) states is given by

$$\Delta E \equiv E_b - E_a = \Delta E_{kin} + \Delta E_{ex}, \tag{A.10}$$

where ΔE_{kin} and ΔE_{ex} are the differences of the kinetic and exchange interaction energies, respectively. Assuming the spin-down electrons within an energy width $\Delta\varepsilon$ near the Fermi level invert the spin and move into the spin-up region, as shown in Fig. A.1(b), the kinetic energy is increased by $\Delta E_{kin} \approx (N(0)\Delta\varepsilon) \cdot \Delta\varepsilon$. Of course, the kinetic energy inhibits magnetization. Using Eq. (A.3), the energy difference of the exchange interaction is given by

$$\Delta E_{ex} = -\frac{I}{2}[(n_+^2 + n_-^2) - 2(\frac{n}{2})^2]. \tag{A.11}$$

A factor of $\frac{1}{2}$ is introduced to exclude double counting the exchange interaction between electrons. Since $n_{\pm} \approx \frac{n}{2} \pm \Delta n \approx \frac{n}{2} \pm N(0)\Delta\varepsilon$, the difference can be written as

$$\Delta E_{ex} = -I[N(0)\Delta\varepsilon]^2. \tag{A.12}$$

Thus, the energy difference ΔE_{ex} must be negative, resulting in favoring magnetization. As a result, the magnetization is determined by competition between the kinetic (unfavoring) and exchange interaction (favoring) energies. The total energy difference ΔE should be negative (or, at most zero) for the ferromagnetic state to be stable. (Note that for $T > 0$ the free energy should be compared instead of the total energy.) Therefore, the Stoner condition is derived again such as

$$\begin{aligned} \Delta E &= [N(0) - IN(0)^2](\Delta\varepsilon)^2 \leq 0 \\ i.e., \quad & IN(0) \geq 1. \end{aligned} \tag{A.13}$$